Topological edge modes in photonic crystals

Shuhei Oono

February 2018

Topological edge modes in photonic crystals

Shuhei Oono
Doctoral Program in Physics

Submitted to the Graduate School of
Pure and Applied Sciences
in Partial Fulfillment of the Requirements
for the Degree of Doctor of Philosophy in
Science

at the
University of Tsukuba

Acknowledgements

First of all, I would like to express my sincere gratitude to Prof. Y. Hatsugai for helpful suggestions, continuous encouragements and strong supports throughout my doctoral program. I would like to thank all my collaborators Prof. Y. Arakawa, Prof. S. Iwamoto, Dr. T. Kariyado, and Dr. S. Takahashi, for their advises and fruitful discussions. I am indebted to Dr. A. Kubo, Prof. S. Okada, Prof. T. Ono, Prof. N. Taniguchi, Prof. Y. Tokura, and Dr. K. Yoshida for encouragements and supports. Also I would like to express special thanks to all of my colleagues, H. Araki, S. Fubasami, H. Hirano, K. Hoda, T. Isobe, R. Kamoda, K. Kohda, K. Kudo, Y. Takahashi, S. Nishizawa, D. Seki, T. Sekizawa, R. Sumi, S. Suzuki, S. Tanaya, and T. Yamazaki for all the stimulating discussions and the warm atomosphere. I am also grateful to people belonging to the Arakawa's group in University of Tokyo, the former Arimitsu's group, the Ono's group, the Okada's group, the Taniguchi's group and the Tokura's group for many enlightening discussions. I would like to thank Jasso and University of Tsukuba for financial supports which made it possible to compete this study. My deepset thanks go to my parents and my family for unconditional support and encouragement in any possible situation.

Contents

Chapter 1

Introduction

1.1 Backgrounds

The discovery of the Quantum Hall Effect by K. v. Klitzing *et al.* in 1980 [1] finally led to the concept of the topological phase in condensed matter physics. The topological property is not found by just seeing the energy spectrum, but it is the property provided by the wave functions [2]. One of the most prominent properties that all of the topological phases share might be the bulk-edge correspondence [3–6], which says that gap-less excitation modes always appears at interface between topologically distinct phases.

Although the conventional quantum Hall states under an external magnetic field had always accompanied formation of Landau levels, Haldane proposed [7] a potential unconventional quantum hall state without Landau levels by breaking time reversal symmetry(TRS) with magnetic order having no net flux. Later it led to the finding of topological insulator [8, 9], where the TRS breaking effect for each spin sector is caused by spin-orbital couplings while entire TRS is conserved. As its name indicates, the topological insulator is insulator in the bulk but with a non-trivial topological invariant and thus it is conducting at the edge.

On the other hand, another pioneering work having relation to this thesis, the discovery of a photonic band material was achieved by Yablonovitch *et al.* [10]. The photonic crystal [11, 12] consists of a spatially periodic pattern of the dielectric constant in macroscopic scale, where propagation of electromagnetic(EM) waves is described by the classical Maxwell equations. As in a single electron state in a solid crystal, an EM state in the photonic crystal is represented by the Bloch state and the frequency dispersion against the wave vector forms a certain band structure in the same way as the electron states in a solid crystal form a energy band structure. The Maxwell equations are macroscopic equations and invariant if the ratio between the frequency(ω) and structural scale(a) is kept (scale-free). Then, we can tune the band gap frequency to a resonance frequency and by creating a point defect in the 3D photonic crystal, we can pin the resonant mode to the point [13, 14]. Moreover, if we excavate a certain line shape, we can control the light propagation along the line [15].

If the gapped band structure and wavefunctions are all of the ingredient required for the topological argument, it also seems to be applicable to the photonic band structure. In 2008, Raghu and Haldane [16, 17] and Soljacic's group in MIT [18] proposed to use magnet-optical materials in photonic crystals and break TRS. Then it resulted in realization of a topologically non-trivial photonic band structures with non-zero Chern numbers and realziation of chiral edge mode propagation of EM waves. Also Soljacic's group experimentally confirmed their proposal [19]. Their achievements made clear that the bulk-edge correspondence itself is not unique to quantum systems but universal in broader classes of physical systems. In addition, their findings stimulated studies not only in classical EM waves but also in other classical systems such as elastic [20, 21], acoustic [22–25] waves or fluid waves [26] in continuous media or even in mechanical systems of the Newton equation [27–32]. Those studies are dubbed as topological xxx ics (acoustics for example), according to the physical system. Specifically, topological photonics seems to be full of promise for practical application in future photonics. The difference of topological edge modes from the conventional photonic crystal waveguide such as [15] is that it is immune to back scatting and thus it is expected to lead to an isolator-free optical circuit or an optical delay line [33].

For two-dimensional systems, the Chern number is well defined as a topological invariant. However it is non-zero only when the TRS is broken. Unlike the electron, the photon is neutral and TRS in a photonic

system is not broken just by applying a magnetic field. Raghu-Haldane or Soljacic *et al.* [16–19] used the gyrotropic materials for photonic crystals. Then, the appearance of the imaginary anti-symmetric off diagonal elements, which is the cause of the magnet-optical coupling, breaks the TRS. However, a sufficiently strong gyrotropic effect for light requires a strong magnetic field, which can be obstacle for implementation in future electronic/optical systems since it can affect badly to other components. Moreover, the off-diagonal element, in general, strongly depends on the wavelength of the light it can be impediment for stable operation. In addition, the off-diagonal element becomes small in shorter wavelengths such as optical frequencies and it lacks the scalability.

1.2 Purpose

The primary purpose of this thesis is the theoretical investigation of topological properties of photonic band structures and topologically protected edge modes by numerical analysis of the photonic band structure and topological invariants. Further, in expectation of compatibility in photonics systems, we confine ourselves only to dielectric materials, which is stable in optical response but does not break TRS. It is also preferable that the mechanism and physical structure are kept as simple as possible.

1.3 Outline

Chapter 2 describes minimal requirements to deal with dielectric materials and magnet-optical materials. In addition, an elementary introduction to the photonic crystal is also described.

Chapter 3 reviews photonic systems in the context of the topological band structure. Those are milestones in topological photonics, and we will also make use of some ideas included in those studies in later parts.

Chapter 4 describes the gaussian expansion method which we use throughout the thesis to numerically analyzes the continuous Maxwell equations. Since topological invariants are defined on an orientable closed space, the matrix eigenequation must be periodic in the parameters(Bloch wave vectors in crystals) for numerical formalization of a topological invariant. The requirement is satisfied if the eigenequation is expanded by a spatially localized basis set and the topological invariants are well defined by the gaussian basis set. After mentioning about the practical procedures, the validity is tested in some typical problems.

In chapter 5, a topologically related surface propagation mode are realized in a 3D uniaxially chiral dielectric photonic crystal. The surface modes are consequence of the bulk-edge correspondence to the non-zero 2D section Chern number, which is given to a 2D slice in the 3D Brillouin zone. The non-zero section Chern number is caused by the formation of the isolated degeneracy point called as Weyl point. The uni-axial chiral structure is formed by a quite simple modification of a two-dimensional photonic crystal. The properties are also taken over by a chiral woodpile structure, which is expected to lead to fabrication in several tenths of micro-meters and has a great compatibility with point defects or line defects.

Chapter 6 concerns the topological Floquet band structures of photonic crystals with temporally periodic modulation. Under the partial breaking of the temporal translation symmetry, the frequency of a harmonic mode is no more conserved. In this case, the states are given by Floquet mode with quasi frequency, which is invariant with mod $\equiv 2\pi/T$ (T being the period of temporal modulation). First, the method for obtaining a Floquet mode band structure from the periodically time-varying continuous Maxwell equations with the gaussian basis expansion are described. It is confirmed that, a Floquet band structure with non-zero Chern number is realized with temporary directed modification and photonic chiral edge modes are induced by such a temporal modification.

In Chapter 7, we focus on the woodpile photonic crystal and consider to deform the structure. We regard the structural deformation degree of freedom of the woodpile structure as a fictitious momentum degree of freedom and then discuss the topological invariant(Chern number) and the bulk-edge correspondence in the synthetic Brillouin zone, which consists of the pure momentum and structural deformation parameter. In particular, it is shown that variation of edge modes during the structural deformation is characterized by the Chern number that is obtained by using the deformation parameter.

Then the thesis conclude with the summary of the obtained results and a future outlook as extension of the thesis.

Chapter 2

Photonic crystal

This chapter describes fundamental facts that are required for the formation of photonic band structure in dielectric or magnetic materials. Starting from general considerations of optical response, we derive expressions of optical constants in the classical description .Then we describe the formation of frequency band gap in the simplest case of 1D photonic crystal. We discuss the band gap and decay length in the transfer matrix formalism.

2.1 Optical responce of materials

2.1.1 Complex dielectric constant

In materials, an EM field $\{\vec{E}, \vec{H}\}$ induces polarization and magnetization. The electric displacement and magnetic flux are given as

$$\boldsymbol{D} = \varepsilon_0 \boldsymbol{E} + \boldsymbol{P}, \quad \boldsymbol{B} = \mu_0 \boldsymbol{H} + \boldsymbol{M}. \tag{2.1}$$

Macroscopically, the effect is represented by the constitutive ralations

$$\boldsymbol{D} = \hat{\varepsilon} \boldsymbol{E}, \quad \boldsymbol{B} = \hat{\mu} \boldsymbol{B}, \tag{2.2}$$

where linear responces

$$\frac{\boldsymbol{P}}{\varepsilon_0} = \hat{\varepsilon}_r \boldsymbol{E}, \quad \frac{\boldsymbol{M}}{\mu_0} = \hat{\mu}_r \boldsymbol{H}, \qquad [\hat{\varepsilon}_r = \left(\hat{\varepsilon} - \hat{1}\right), \hat{\mu}_r = \left(\hat{\mu} - \hat{1}\right)], \tag{2.3}$$

are assumed. The $\hat{\epsilon}$ and $\hat{\mu}$ are called as the permittivity and permeability and those are generally complex valued quantities. The imarginary part of the dielectric constant physically means absorption of the energy by the material. The linear relations of the polarization or magnetization is microscopically given by the deviation of electron's localization center from the ion or an allignment of magnetic dipoles. However, since the time scale of magnetic motion is much larger than the optical oscilation, it is usually neglected as $\hat{\mu} = \mu_0 \hat{1}$. On the other hand, the time scale of elctric motion is comparable to optical frequencies (a tens of nanometers in semicon ductors). The Maxwell equations in a uniform medium are

$$\nabla \cdot \boldsymbol{D} = 0, \qquad \nabla \cdot \boldsymbol{B} = 0 \tag{2.4}$$

$$\frac{\partial}{\partial t} \boldsymbol{D} = \nabla \times \boldsymbol{H}, \qquad -\frac{\partial}{\partial t} \boldsymbol{B} = \nabla \times \boldsymbol{E}. \tag{2.5}$$

Taking the rotatin of the bottom left eq. and substituting the bottom right eq., we obtaine the EM wave propagation

$$\begin{aligned} \frac{\partial^2}{\partial t^2} \hat{\mu} \hat{\varepsilon} \boldsymbol{E} &= \nabla^2 \boldsymbol{E} \\ \frac{\partial^2}{\partial t^2} &= \frac{1}{(nc)^2} \nabla^2 \boldsymbol{E}, \end{aligned} \tag{2.6}$$

for $\hat{\mu}\hat{\varepsilon} = \varepsilon \hat{1} = \sqrt{n} \hat{1}$.

Generally, the $\hat{\varepsilon}$ is not isotropic. For real symmetric tensor $\hat{\varepsilon}$, the eigenvalues may take different values, which leads to the anisotropy. Since it gives difference in propagation speed according to the axial polarizations, it changes the type of polarization such as, circlular, elliptic, or linear and it is used as a wave plate. However, this type of transition is still reciprocal, since if a linear polarized light is transformed into a circularly polarized one throught a medium, the circularly polarized light is transformed to the linearly polarized light by going back the propagation. There also exist materials having a complex anti-symmetric tensor,

$$\hat{\varepsilon} = \begin{pmatrix} \varepsilon_{xx} & -\varepsilon_{xy} & 0 \\ \varepsilon_{xy} & \varepsilon_{xx} & 0 \\ 0 & 0 & \varepsilon_{zz}. \end{pmatrix} \tag{2.7}$$

The hermiticity is kept if $\mathbf{Im}[\varepsilon_{ii}] = 0$ and $\mathbf{Re}[\epsilon_{xy}] = 0$. For light propagatin in the z direction, we can diagonlize the tensor with right or left circular polarization and refractive indices for them are

$$n_{\pm} = \sqrt{\varepsilon_{xx} \pm \varepsilon_{xy}}, \tag{2.8}$$

which gives difference in propagation speed between the right and left circular polarizations. As a consequence, the polarization plane of a linearly polarized light rotates after propagating through the medium, which is called as Faraday rotation. This process is non-reciprocal. By going back the propagation, the sense of circular polarization is not conversed but the untisymmetric tensor is conversed and then the linearly polarized light is rotated in the opposite direction with respect to the propagating directin. Then, the polization plane is not restored for backward input and the process is non-reciprocal.

2.1.2 Causality and the Kramers-Kronig relatoins

The frequency dependence of the dielectric constant means the non locality of the responce. Indicating the frequency dependence, the constitutive relation is given as

$$\boldsymbol{D}(\omega) = \hat{\varepsilon}(\omega)\boldsymbol{E}(\omega). \tag{2.9}$$

The fourier transformation gives the relation in real time

$$\begin{aligned} \boldsymbol{D}(t) &= \frac{1}{2\pi}\int_{-\infty}^{\infty} \hat{\varepsilon}(\omega)\boldsymbol{E}(\omega)\mathrm{e}^{-\mathrm{i}\omega t}\mathrm{d}\omega \\ &= \left(\frac{1}{2\pi}\right)^2 \int_{-\infty}^{\infty} \mathrm{d}\omega\, \hat{\varepsilon}(\omega)\mathrm{e}^{-\mathrm{i}\omega t} \int_{-\infty}^{\infty} \mathrm{d}t'\, \boldsymbol{E}(t')\mathrm{e}^{\mathrm{i}\omega t'} \\ &= \varepsilon_0 \left\{ \boldsymbol{E}(t) + \int_{-\infty}^{\infty} \hat{G}(\tau)\boldsymbol{E}(t-\tau)\mathrm{d}\tau \right\}, \end{aligned} \tag{2.10}$$

where the retardance function $\hat{G}(\tau)$ is given by

$$\hat{G}(\tau) = \frac{1}{2\pi}\int_{-\infty}^{\infty} \left[\hat{\varepsilon}(\omega)/\varepsilon_0 - \hat{1}\right]\mathrm{e}^{-\mathrm{i}\omega\tau}\mathrm{d}\omega, \tag{2.11}$$

and it is assumed to be a real valued quantity. Note that the constant $\hat{\varepsilon}(\omega)$ gives $\hat{G}(\tau) = \left[\hat{\varepsilon}(\omega)/\varepsilon_0 - \hat{1}\right]\delta(\tau)$, meaning the instantaneous responce.

From causality, the nonlocal relation Eq. (2.10) should be given in the form

$$\boldsymbol{D}(t) = \varepsilon_0 \left\{ \boldsymbol{E}(t) + \int_{0}^{\infty} \hat{G}(\tau)\boldsymbol{E}(t-\tau)\mathrm{d}\tau \right\}. \tag{2.12}$$

In accordance, from the relation (2.11), all of the poles of $\hat{\varepsilon}(\omega)/\varepsilon_0 - \hat{1}$ must lie within the lower-half of the complex ω plane and it must be analytic in the entire upper half. The dielectric constant is now expressed as

$$\frac{\hat{\varepsilon}(\omega)}{\varepsilon_0} = \hat{1} + \int_{0}^{\infty} \hat{G}(\tau)\mathrm{e}^{\mathrm{i}\omega\tau}\mathrm{d}\tau. \tag{2.13}$$

This expression tells us several meaningful consequences. The complex conjugate gives the relation

$$\frac{\hat{\varepsilon}(-\omega)}{\varepsilon_0} = \left(\frac{\hat{\varepsilon}(\omega)}{\varepsilon_0}\right)^* . \tag{2.14}$$

Integration by parts in Eq. (2.13) gives the recursive series

$$\frac{\hat{\varepsilon}(\omega)}{\varepsilon_0} - \hat{1} = \frac{\mathrm{i}\hat{G}(0)}{\omega} - \frac{\hat{G}'(0)}{\omega^2} + \cdots , \tag{2.15}$$

where the argument of $\hat{G}(\tau)$ is $\tau = 0^+$. It is unphysical $\hat{G}(0^-) = 0$ while $\hat{G}(t^+) \neq 0$. Thus the first term in the series must vanish and it decays at higher frequencies as $1/\omega^2$. The series (2.15) shows the behavier of the $\hat{\varepsilon}(\omega)/\varepsilon_0 - \hat{1}$ in the large ω limit as

$$\mathrm{Re}\left[\frac{\hat{\varepsilon}(\varepsilon)}{\varepsilon_0}\right] - \hat{1} \simeq O(\frac{1}{\omega^2}), \quad \mathrm{Im}\left[\frac{\hat{\varepsilon}(\omega)}{\varepsilon_0}\right] = O\left(\frac{1}{\omega^3}\right), \quad (\omega \to \infty). \tag{2.16}$$

The Kramers-Kronig relations

The causality guarantees the analyticity of the $\hat{\varepsilon}(\omega)$ in the upper-half complex ω plane. The analytisity gives us the Caucy's relation

$$\frac{\hat{\varepsilon}(z)}{\varepsilon_0} = \hat{1} + \frac{1}{2\pi\mathrm{i}} \oint_C \frac{\hat{\varepsilon}(\omega')/\varepsilon_0 - \hat{1}}{\omega' - z} \mathrm{d}\omega'. \tag{2.17}$$

The contour C is taken as the real axis and the upper semi-circle of infinite radius. Since $\hat{\varepsilon}/\varepsilon_0 - \hat{1}$ decays as $O(1/\omega^2)$((2.16)) in the limit $\omega \to \infty$, the contour is replaced by the real axis. Then, the above expression can be written as

$$\frac{\varepsilon(z)}{\varepsilon_0} = 1 + \frac{1}{2\pi\mathrm{i}} \int_{-\infty}^{\infty} \frac{\varepsilon(\omega')/\epsilon_0 - 1}{\omega' - z} \mathrm{d}\omega'. \tag{2.18}$$

To avoid the singularity on the real axis, we take it as $z = \omega + \mathrm{i}\delta$, and Eq. (2.18) is

$$\frac{\hat{\varepsilon}(\omega)}{\varepsilon_0} = \hat{1} + \frac{1}{2\pi\mathrm{i}} \int_{-\infty}^{\infty} \frac{\hat{\varepsilon}(\omega')/\epsilon_0 - \hat{1}}{\omega' - \omega - \mathrm{i}\delta} \mathrm{d}\omega'. \tag{2.19}$$

The denominator in the integrand is formally written as

$$\frac{1}{\omega' - \omega - \mathrm{i}\delta} = P(\frac{1}{\omega' - \omega}) + \mathrm{i}\pi\delta(\omega' - \omega), \tag{2.20}$$

where the P means taking principal part. The use of the Eq. (2.20) reduces the Eq. (2.19) to

$$\frac{\hat{\varepsilon}(\omega)}{\varepsilon_0} = 1 + \frac{1}{\pi\mathrm{i}} P \int_{-\infty}^{\infty} \frac{\hat{\varepsilon}(\omega')/\varepsilon_0 - \hat{1}}{\omega' - \omega} \mathrm{d}\omega'. \tag{2.21}$$

The real and imarginary parts are given as

$$\mathrm{Re}[\hat{\varepsilon}(\omega)/\varepsilon_0] = \hat{1} + \frac{1}{\pi} P \int_{-\infty}^{\infty} \frac{\mathrm{Im}\,[\hat{\varepsilon}(\omega')/\varepsilon_0]}{\omega' - \omega} \mathrm{d}\omega' \tag{2.22}$$

$$\mathrm{Im}[\hat{\varepsilon}(\omega)/\varepsilon_0] = -\frac{1}{\pi} P \int_{-\infty}^{\infty} \frac{\mathrm{Re}\,[\hat{\varepsilon}(\omega')/\varepsilon_0] - \hat{1}}{\omega' - \omega} \mathrm{d}\omega'. \tag{2.23}$$

These equations relates the real part and imarginaly part. Therefore, if the whole spectrum of either one is obtained, the other is given by these relations. The relations Eq. (2.23) is called as the Kramers-Kronig relation and it was derived from the causality. Note that since

$$P \int_{\infty}^{\infty} \frac{1}{\omega' - \omega} \mathrm{d}\omega' = 0,$$

a constant responce $Re\,[\hat{\varepsilon}(\omega) = C]$ eliminates the imarginary part. From the property(Eq. (2.14)), the real part of $\hat{\varepsilon}(\omega)/\varepsilon_0$ is even and the imarginary part is odd. This fact allows us further reduce the relations Eq. (2.23),

$$\mathrm{Re}\left[\frac{\hat{\varepsilon}(\omega)}{\varepsilon_0}\right] = \hat{1} + \frac{2}{\pi} P \int_0^{\infty} \frac{\mathrm{Im}\,[\hat{\varepsilon}(\omega')/\varepsilon_0]}{\omega'^2 - \omega^2} \mathrm{d}\omega' \tag{2.24}$$

$$\mathrm{Im}\left[\frac{\hat{\varepsilon}(\omega)}{\varepsilon_0}\right] = -\frac{2\omega}{\pi} P \int_0^{\infty} \frac{\mathrm{Re}\,[\hat{\varepsilon}(\omega')/\varepsilon_0]}{\omega'^2 - \omega^2} \mathrm{d}\omega'. \tag{2.25}$$

2.1.3 Description of light matter interaction

Classical description

The electric polarization of charged particle q is given by using the average deviation $\vec{u}$ as

$$\boldsymbol{P} = Nq\boldsymbol{u}. \tag{2.26}$$

Electric susceptibility from a classical description

Regarding the charged particles in materials as the classical point-like particle, we can consider its classical motion in an oscilating electric field and a static magnetic field. Then, we estimate the polarization from its average deviation. We consider motion of a charged particle bounded by a localized ion in the EM field, which follows the equation

$$m\frac{\mathrm{d}^2\boldsymbol{u}}{\mathrm{d}t^2} + m\gamma\frac{\mathrm{d}\boldsymbol{u}}{\mathrm{d}t} + m\omega_0^2\boldsymbol{u} = q\left(\boldsymbol{E} + \frac{\mathrm{d}\boldsymbol{u}}{\boldsymbol{dt}} \times \boldsymbol{B}\right), \tag{2.27}$$

where the m is mass of the cherged particle, the γ is inverse of the mean free time of the particle and ω_0 is the resonance frequency. We take the direction of the magnetic field in the z direction $\vec{B} = (0, 0, B)$, and assume the oscilating elctric field as $\vec{E}(t, \vec{r}) = \vec{E}_0 \mathrm{e}^{-\mathrm{i}\omega t}$. The motion of the particle takes place in the same frequency as the external oscilating field ω as

$$\boldsymbol{u}(t) = \boldsymbol{u}_0 \mathrm{e}^{-\mathrm{i}\omega t}. \tag{2.28}$$

Substituting this into the Eq. (2.27), we obtaine

$$-m\omega^2\boldsymbol{u}_0 - \mathrm{i}m\gamma\boldsymbol{u}_0 + m\omega_0^2\boldsymbol{u}_0 = q\left(\boldsymbol{E} - \mathrm{i}\omega\boldsymbol{u}_0 \times \boldsymbol{B}\right). \tag{2.29}$$

We write down the equation for each component

$$m\left(\omega^2 + \mathrm{i}\gamma\omega - \omega_0^2\right)u_{0x} - \mathrm{i}q\omega B u_{0y} = -qE_x \tag{2.30}$$

$$\mathrm{i}q\omega B u_{0x} + m\left(\omega^2 + \mathrm{i}\gamma\omega - \omega_0^2\right)u_{0y} = -qE_y \tag{2.31}$$

$$m\left(\omega^2 + \mathrm{i}\gamma\omega - \omega_0^2\right)u_{0z} = -qE_z. \tag{2.32}$$

Solving the equations, we obtaine the deviation and then the polarization by Eq. (2.26). The susceptibility $\chi_{ij} = P_i/\varepsilon_0 E_j$ is obtained as follows

$$\chi_{xx} = -\frac{Nq^2}{m\varepsilon_0} \cdot \frac{\omega^2 + \mathrm{i}\omega\gamma - \omega_0^2}{\left(\omega^2 + \mathrm{i}\omega\gamma - \omega_0^2\right)^2 - \omega^2\omega_c^2} \tag{2.33}$$

$$\chi_{yx} = \frac{Nq^2}{m\varepsilon_0} \cdot \frac{\mathrm{i}\omega\omega_c}{\left(\omega^2 + \mathrm{i}\omega\gamma - \omega_0^2\right)^2 - \omega^2\omega_c^2} \tag{2.34}$$

$$\chi_{zz} = -\frac{Nq^2}{m\varepsilon_0} \cdot \frac{1}{\omega^2 + \mathrm{i}\omega\gamma - \omega_0^2}, \tag{2.35}$$

where the $\omega_c = |qB/m|$ is the cyclotron frequency.

The components of relative permittivity $\hat{\varepsilon} = \hat{I} + \hat{\chi}$ are respectively

$$\varepsilon_{xx} = 1 - \frac{Nq^2}{m\varepsilon_0} \cdot \frac{\omega^2 + \mathrm{i}\omega\gamma - \omega_0^2}{\left(\omega^2 + \mathrm{i}\omega\gamma - \omega_0^2\right)^2 - \omega^2\omega_c^2} \tag{2.36}$$

$$\varepsilon_{yx} = \frac{Nq^2}{m\varepsilon_0} \cdot \frac{\mathrm{i}\omega\omega_c}{\left(\omega^2 + \mathrm{i}\omega\gamma - \omega_0^2\right)^2 - \omega^2\omega_c^2} \tag{2.37}$$

$$\varepsilon_{zz} = 1 - \frac{Nq^2}{m\varepsilon_0} \cdot \frac{1}{\omega^2 + \mathrm{i}\omega\gamma - \omega_0^2} \quad . \tag{2.38}$$

Further, the conductance of materials are given by $\sigma_{ij} = -\mathrm{i}\omega\varepsilon_0\left(\tilde{\varepsilon}_{ij} - \delta_{ij}\right)$

$$\sigma_{xx} = \frac{Nq^2}{m} \cdot \frac{\mathrm{i}\omega\left(\omega^2 + \mathrm{i}\omega\gamma - \omega_0^2\right)}{\left(\omega^2 + \mathrm{i}\omega\gamma - \omega_0^2\right)^2 - \omega^2\omega_c^2} \tag{2.39}$$

$$\sigma_{yx} = \frac{Nq^2}{m} \cdot \frac{-\omega^2\omega_c}{\left(\omega^2 + \mathrm{i}\omega\gamma - \omega_0^2\right)^2 - \omega^2\omega_c^2} \tag{2.40}$$

$$\sigma_{zz} = \frac{Nq^2}{m} \cdot \frac{\mathrm{i}\omega}{\omega^2 + \mathrm{i}\omega\gamma - \omega_0^2} \quad . \tag{2.41}$$

In the following, we give the dielectric constans in specific cases.

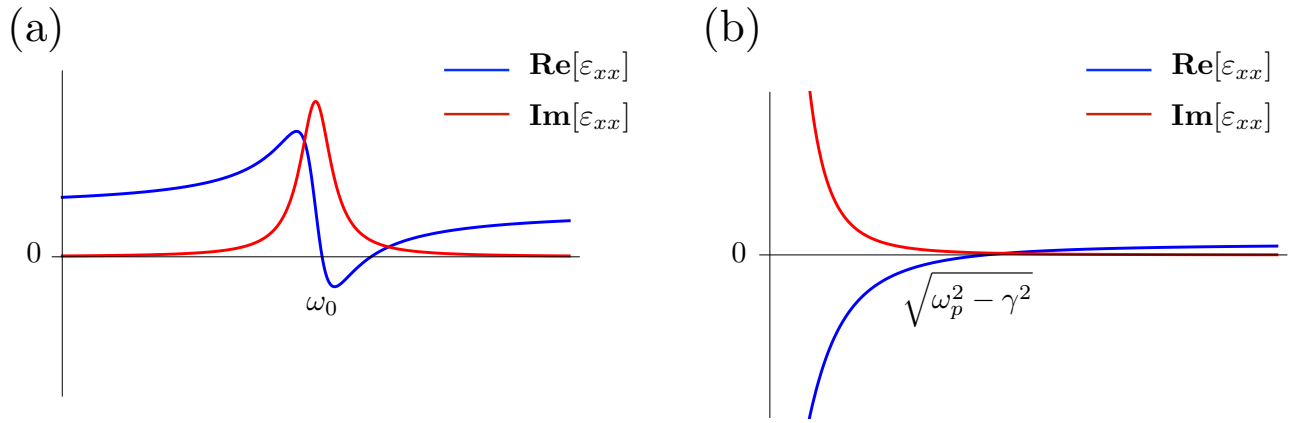

Figure 2.1: Plot of the real and imaginary parts of ε_{xx}, (a) of the Lorentz model and (b) the Drude model.

Bounded particlse without magnetic field -The Lorentz model-

In this case, the permittivity tensor Eq. (2.38) is diagonal and it is

$$\varepsilon_{xx} = \varepsilon_{zz} = 1 - \frac{Nq^2}{m\varepsilon_0} \cdot \frac{1}{\omega^2 + \mathrm{i}\omega\gamma - \omega_0^2}. \tag{2.42}$$

The dispersion of this type is called as Lorentzian. The real part and imarginary(shown in Fig. 2.1(a)) part are respectively

$$\mathrm{Re}\left[\varepsilon\right] = 1 - \frac{Nq^2}{m\varepsilon_0} \cdot \frac{\omega^2 - \omega_0^2}{\left(\omega^2 - \omega_0^2\right)^2 + \omega^2\gamma^2} \tag{2.43}$$

$$\mathrm{Im}\left[\varepsilon\right] = \frac{Nq^2}{m\varepsilon_0} \cdot \frac{\omega\gamma}{\left(\omega^2 - \omega_0^2\right)^2 + \omega^2\gamma^2}. \tag{2.44}$$

Free particle without magnetic field -The Drude model-

The isotropic permittivity is given as

$$\varepsilon = 1 - \frac{Nq^2}{m\varepsilon_0} \cdot \frac{1}{\omega^2 + \mathrm{i}\omega\gamma}. \tag{2.45}$$

The real and imarginary parts(shown in Fig. 2.1(b)) are respectively

$$\mathrm{Re}\left[\varepsilon\right] = 1 - \frac{Nq^2}{m\varepsilon_0} \cdot \frac{1}{\omega^2 + \gamma^2} \tag{2.46}$$

$$\mathrm{Im}\left[\varepsilon\right] = \frac{Nq^2}{m\varepsilon_0} \cdot \frac{\gamma}{\omega\left(\omega^2 + \gamma^2\right)} \quad . \tag{2.47}$$

In the limit $\omega \to 0$, the imaginary part diverges and the real part takes minus value, meaning motion of free electrons screen the EM field. Incresing ω the real part crosses zero, meaning electrons can not follow the EM field. Neglegteing the dumping ratio γ, the crossing frequency is given by

$$\omega_p = \sqrt{\frac{Nq^2}{m\varepsilon_0}}, \tag{2.48}$$

and the ω_p is called as the *plasma frequency*.

Free particle under magnetic field

The existence of magnetic field($\omega_c \neq 0$) cause the circular dichroism, since

$$n_\pm^2 = \varepsilon_{xx} \pm \mathrm{i}\varepsilon_{xy} = 1 + \frac{\omega_p^2}{\left(\omega^2 + \mathrm{i}\omega\gamma - \omega_0^2\right)^2 - \omega^2\omega_c^2}\left\{-\left(\omega^2 + \mathrm{i}\omega\gamma - \omega_0^2\right) \mp \omega\omega_c\right\}. \tag{2.49}$$

For $\gamma = 0$ and $\omega_0 = 0$(free electron without damping), it further simplifies into

$$n_\pm^2 = 1 - \frac{\omega_p^2}{\omega\left(\omega \pm \omega_c\right)}. \tag{2.50}$$

The Drude model under magnetic field
For $\omega_0 = 0$, the conductance Eqs. (2.41) are

$$\sigma_{xx}(\omega) = \frac{Nq^2}{m} \cdot \frac{\mathrm{i}\left(\omega + \mathrm{i}\gamma\right)}{\left(\omega + \mathrm{i}\gamma\right)^2 - \omega_c^2} \tag{2.51}$$

$$\sigma_{xy}(\omega) = \frac{Nq^2}{m} \cdot \frac{-\omega_c}{\left(\omega + \mathrm{i}\gamma\right)^2 - \omega_c^2} \tag{2.52}$$

$$\sigma_{zz}(\omega) = \frac{Nq^2}{m} \cdot \frac{\mathrm{i}}{\omega + \mathrm{i}\gamma} \quad . \tag{2.53}$$

The DC limit ($\omega \to 0$) gives the Hall conductance.

$$\sigma_{xy} = \frac{Nq^2}{m} \cdot \frac{\omega_c}{\gamma^2 + \omega_c^2}. \tag{2.54}$$

The binding force ω_0 is given by quantum mechanical calculations. The magnetic effect by the internal magnetic order is also can not be explanined without quantum mechanics.

2.2 Photonic crystals

2.2.1 1D photonic crystal

We consider one-dimensional periodic structures, which have the simplest form and thus, in many cases, enable us to derive several analytic relations, such as gap size, attenuation length, transmittivity. An answer for the question why frequency gap emerges may be obtained by considering the one-dimensional case, since higher dimensional periodic structures are also regarded as a one-dimensional structure for a wave propagating in one fixed direction, namely a Bloch state. If we are thinking about a behavior of EM field in a large scale, all of systems called '1D photonic crystal' fall into the stacking of layers with different optical indices. Most simply, a gapped frequency dispersion is achieved by repetition of two kinds of layers.

Here we derive the photonic band gap with tranfermatrix formalism [34]. We consider a wave entering into an interface with normal incidence. Taking the z axis as the propagation direction and x axis for the polarization direction, the wave is represented as

$$\boldsymbol{E} = \mathbf{e}_x\left(a^{\mathrm{in}}\mathrm{e}^{\frac{\mathrm{i}}{c\omega}nx} + a^{\mathrm{out}}\mathrm{e}^{\frac{-\mathrm{i}}{c\omega}nx}\right). \tag{2.55}$$

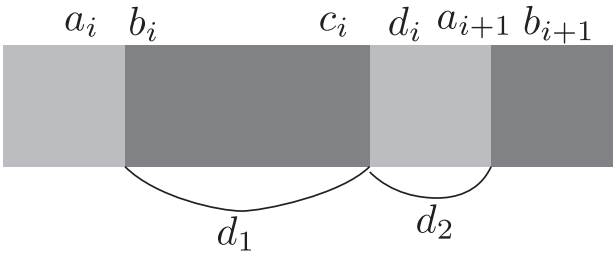

Figure 2.2: Layered structure of one-dimensional photonic crystal.

The continuity at the interface for electric fields gives

$$a_i^{\text{in}} + a_i^{\text{out}} = b_i^{\text{in}} + b_i^{\text{out}}. \tag{2.56}$$

The magnetic field is obtained from $\mathrm{i}\omega \boldsymbol{H} = \nabla \times \boldsymbol{E}$ and the continuity for the magnetic fields at the interface gives

$$n_1 \left(a_i^{\text{in}} - a_i^{\text{out}}\right) = n_2 \left(-b_i^{\text{in}} + b_i^{\text{out}}\right). \tag{2.57}$$

This relation is more consisely given in a matrix form

$$\begin{pmatrix} b_i^{\text{in}} \\ b_i^{\text{out}} \end{pmatrix} = \begin{pmatrix} \frac{n_2-n_1}{2n_2} & \frac{n_2+n_1}{2n_2} \\ \frac{n_2+n_1}{2n_2} & \frac{n_2-n_1}{2n_2} \end{pmatrix} \begin{pmatrix} a_i^{\text{in}} \\ a_i^{\text{out}} \end{pmatrix}. \tag{2.58}$$

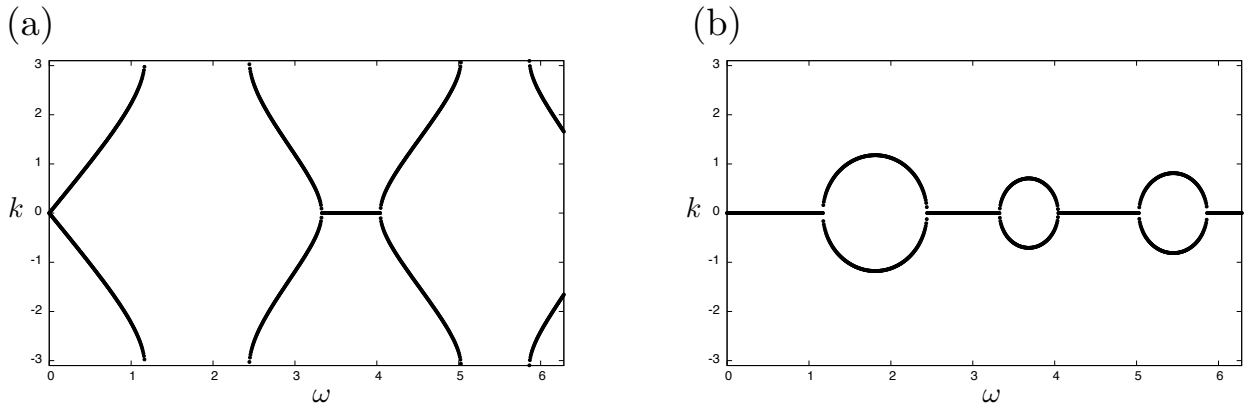

Figure 2.3: The frequency dispersion of the 1D photonic crystal with the normal incidence in a set up $d_1 = 0.3$, $d_2 = 0.7$, $\varepsilon_1 = 1$, $\varepsilon_2 = 3.4^2$. (a) The real part of the wavenumber k plotted to the frequency ω. (b) In freqency regions with $\mathrm{Re}[k] = 0$, the k is pure imaginary, otherwise it is pure real. The imaginary part of the k. The $\mathrm{Im}[k]$ represents decay late of the wave. It is largest at middle of the band gap.

Within the same structure, the wave propargates freely and thus, the relation between both ends of fields are given by

$$\begin{pmatrix} c_i^{\text{in}} \\ c_i^{\text{out}} \end{pmatrix} = \begin{pmatrix} 0 & \mathrm{e}^{\frac{\mathrm{i}\omega}{c} n_1 d_1} \\ \mathrm{e}^{-\frac{\mathrm{i}\omega}{c} n_1 d_1} & 0 \end{pmatrix} \begin{pmatrix} b_i^{\text{in}} \\ b_i^{\text{out}} \end{pmatrix}. \tag{2.59}$$

In 1D photonic crystal which is repetition of two kinds of layeres like in Fig.2.2, the relation between neibohring cites is given by a product of matricies like Eqs. (2.58)(2.59) as

$$\begin{pmatrix} a_i^{\text{in}} \\ a_i^{\text{out}} \end{pmatrix} = \begin{pmatrix} M_{11} & M_{12} \\ M_{21} & M_{22} \end{pmatrix} \begin{pmatrix} a_{i+1}^{\text{in}} \\ a_{i+1}^{\text{out}} \end{pmatrix}, \tag{2.60}$$

where the matrix M represents

$$M = \begin{pmatrix} 0 & e^{\frac{i\omega}{c}n_2 d_2} \\ e^{\frac{-i\omega}{c}n_2 d_2} & 0 \end{pmatrix} \begin{pmatrix} \frac{n_1-n_2}{2n_2} & \frac{n_1+n_2}{2n_2} \\ \frac{n_1+n_2}{2n_2} & \frac{n_1-n_2}{2n_2} \end{pmatrix} \begin{pmatrix} 0 & e^{\frac{i\omega}{c}n_1 d_1} \\ e^{-\frac{i\omega}{c}n_1 d_1} & 0 \end{pmatrix} \begin{pmatrix} \frac{n_2-n_1}{2n_1} & \frac{n_2+n_1}{2n_1} \\ \frac{n_1+n_2}{2n_1} & \frac{n_2-n_1}{2n_1} \end{pmatrix} \tag{2.61}$$

$$M_{11} = \frac{(n_1+n_2)^2}{4n_1n_2} e^{\frac{i\omega}{c}(n_1d_1+n_2d_2)} - \frac{(n_1-n_2)^2}{4n_1n_2} e^{\frac{i\omega}{c}(-n_1d_1+n_2d_2)} \tag{2.62}$$

$$M_{12} = \frac{\left(n_2^2-n_1^2\right)}{4n_1n_2} e^{\frac{i\omega}{c}(n_1d_1+n_2d_2)} + \frac{\left(n_1^2-n_2^2\right)}{4n_1n_2} e^{\frac{i\omega}{c}(-n_1d_1+n_2d_2)} \tag{2.63}$$

$$M_{21} = \frac{\left(n_1^2-n_2^2\right)}{4n_1n_2} e^{\frac{i\omega}{c}(n_1d_1-n_2d_2)} + \frac{\left(n_2^2-n_1^2\right)}{4n_1n_2} e^{\frac{i\omega}{c}(-n_1d_1-n_2d_2)} \tag{2.64}$$

$$M_{22} = -\frac{(n_2-n_1)^2}{4n_1n_2} e^{\frac{i\omega}{c}(n_1d_1-n_2d_2)} + \frac{(n_1+n_2)^2}{4n_1n_2} e^{\frac{i\omega}{c}(-n_1d_1-n_2d_2)} \tag{2.65}$$

Applying the Bloch's theorem, we obtain an eigenequation

$$\begin{pmatrix} a_{i+1}^{\text{in}} \\ a_{i+1}^{\text{out}} \end{pmatrix} = M \begin{pmatrix} a_i^{\text{in}} \\ a_i^{\text{out}} \end{pmatrix} = \lambda \begin{pmatrix} a_i^{\text{in}} \\ a_i^{\text{out}} \end{pmatrix} \tag{2.66}$$

If the eigenvalue λ is pure imaginary, the eigenmode is extended mode and otherwise, it decays in the crystal. The eigenvalue is given as

$$\lambda = \frac{1}{2}\left(\text{Tr}M \pm \sqrt{(\text{Tr}M)^2 - 4\text{det}|M|}\right). \tag{2.67}$$

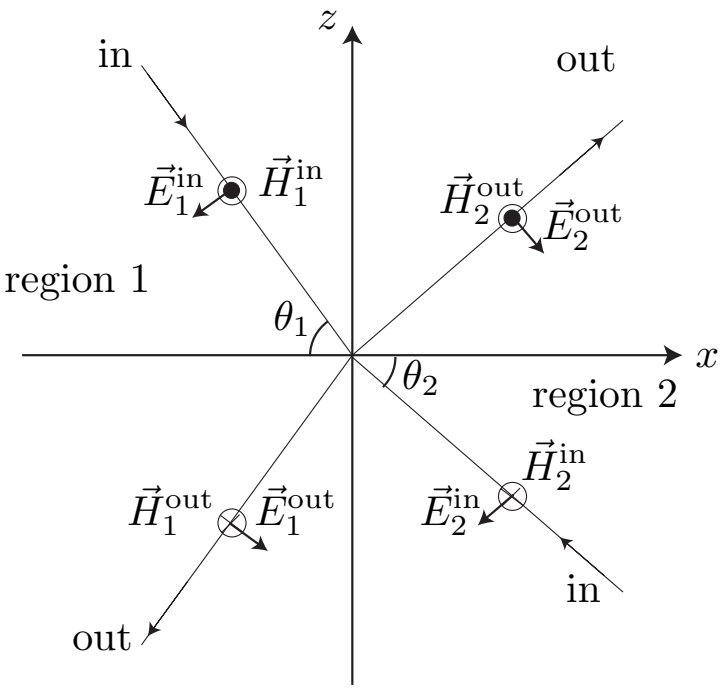

Figure 2.4: A schematic that shows convention of the directions(phases) of vectors on the points. The amplitude of each vector is taken along the direction shown in the schematic.

The frequency dispersion in a set up is plotted in the Fig. 2.3

In next, we proceed to consider the case of oblique incidence. Since the incident angle is no longer normal, the degeneracy between two transverse direcison dissolves. It is convenient to distinguish the difference by

seeing whether the oscilation is included in the incident plane or not. The polarization perpendicular to the incidence plane is called as $s-$polarization, whereas the polarization included within the incidence plane is called as $p-$polarization. Since the number of components increases within the incidence plane, it is better to derive the relation with respect to the one component out of the incidence plane.

Let us consider the case of $p-$polarization. In this case we construct the equation on the magnetic component H_y. To meet the convention used in the case electric component, we write the magnetic field in the region1 as

$$H_1(\boldsymbol{r}) = H_1^{\text{in}} \mathrm{e}^{-\mathrm{i}\boldsymbol{k}_1^{\text{in}}\cdot\boldsymbol{r}} - H_1^{\text{out}} \mathrm{e}^{-\mathrm{i}\boldsymbol{k}_1^{\text{out}}\cdot\boldsymbol{r}}, \tag{2.68}$$

and in the region2 as

$$H_2(\boldsymbol{r}) = -H_2^{\text{in}} \mathrm{e}^{-\mathrm{i}\boldsymbol{k}_2^{\text{in}}\cdot\boldsymbol{r}} + H_2^{\text{out}} \mathrm{e}^{-\mathrm{i}\boldsymbol{k}_1^{\text{out}}\cdot\boldsymbol{r}}. \tag{2.69}$$

The boudary condition about the magnetic component reads

$$H_1^{\text{in}} - H_1^{\text{out}} = -H_2^{\text{in}} + H_2^{\text{out}}. \tag{2.70}$$

The boundary condition about the electric component is represented as

$$E_{1z}^{\text{in}} + E_{1z}^{\text{out}} = E_{2z}^{\text{in}} + E_{2z}^{\text{out}} \tag{2.71}$$

$$\varepsilon_1 \left(E_{1x}^{\text{in}} + E_{1x}^{\text{out}}\right) = \varepsilon_2 \left(E_{2x}^{\text{in}} + E_{2x}^{\text{out}}\right). \tag{2.72}$$

Since the elctric component is related to the magnetic component by[1] [2]

$$\mathrm{i}\omega\varepsilon\boldsymbol{E} = \nabla \times \boldsymbol{H} = -\frac{1}{c\sqrt{\varepsilon}|\boldsymbol{k}|}\nabla \times \boldsymbol{H}_0 \tag{2.73}$$

From these relations, the equations about the elctric component is rewritten as

$$\frac{1}{\sqrt{\varepsilon_1}} \cos\theta_1 \left(H_1^{\text{in}} + H_1^{\text{out}}\right) = \frac{1}{\sqrt{\varepsilon_2}} \cos\theta_2 \left(H_2^{\text{in}} + H_2^{\text{out}}\right) \tag{2.74}$$

$$\sqrt{\varepsilon_1} \sin\theta_1 \left(H_1^{\text{in}} - H_1^{\text{out}}\right) = \sqrt{\varepsilon_2} \sin\theta_2 \left(H_2^{\text{in}} - H_2^{\text{out}}\right) \tag{2.75}$$

For both of Eq. (2.70) and Eq. (2.74) to be sattisfied, the relation

$$\begin{aligned} \frac{1}{\sqrt{\varepsilon_1}} \sin\theta_1 &= \frac{1}{\sqrt{\varepsilon_2}} \sin\theta_2 \\ \frac{\sin\theta_1}{\sin\theta_2} &= \sqrt{\frac{\varepsilon_1}{\varepsilon_2}} \end{aligned} \tag{2.76}$$

must hold. This is the Snell's law. From this, the θ_2 can be solved by θ_1

$$\cos\theta_2 = \sqrt{1 - \frac{\epsilon_1}{\epsilon_2}\sin^2\theta_1}. \tag{2.77}$$

Putting[3]

$$\lambda_{12} = \sqrt{\frac{\varepsilon_1}{\varepsilon_2}}\frac{\cos\theta_2}{\cos\theta_1} = \left(\sqrt{\frac{\varepsilon_1}{\varepsilon_2}}\sqrt{1 - \frac{\varepsilon_1}{\varepsilon_2}\sin^2\theta_1}\right) / \cos\theta_1, \tag{2.78}$$

two asociated equations are written as

$$\left(H_1^{\text{in}} + H_1^{\text{out}}\right) = \lambda_{12}\left(H_2^{\text{in}} + H_2^{\text{out}}\right) \tag{2.79}$$

$$H_1^{\text{in}} - H_1^{\text{out}} = H_2^{\text{in}} - H_2^{\text{out}}. \tag{2.80}$$

---

[1]
$$\nabla \times \boldsymbol{H} = \nabla \times \left(\boldsymbol{H}_0 \mathrm{e}^{-\mathrm{i}\boldsymbol{k}\cdot\boldsymbol{r}}\right) = -\mathrm{i}\left(\boldsymbol{k} \times \boldsymbol{H}_0\right)\mathrm{e}^{-\mathrm{i}\boldsymbol{k}\cdot\boldsymbol{r}}$$

[2] $\omega = \frac{c|\boldsymbol{k}|}{\sqrt{\varepsilon}}$, $\boldsymbol{E} = -\frac{1}{\mathrm{i}\omega\varepsilon}\nabla \times \boldsymbol{H} = -\frac{1}{c\sqrt{\varepsilon}|\boldsymbol{k}|}\boldsymbol{k} \times \boldsymbol{H}_0$

[3] This quantity sattisfies $\mathrm{Re}\left[\cos\theta_2\right] < 1.0$, and can be pure imaginary if $\varepsilon_1 > \varepsilon_2$.

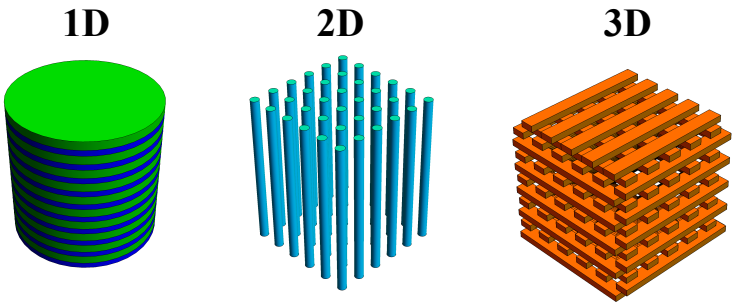

Figure 2.5: A schematic of 2D and 3D photonic crystals. A periodci spatial variation of the optical constants are realized by placing materials with different optical constants, or in a popular way creating holes within a dielectric material.

Then, the transfer matrix at the interface for oblique incidence θ_1 reads

$$\begin{pmatrix} H_1^{\text{in}} \\ H_1^{\text{out}} \end{pmatrix} = \begin{pmatrix} \frac{1}{2}(\lambda_{12}+1) & \frac{1}{2}(\lambda_{12}-1) \\ \frac{1}{2}(\lambda_{12}-1) & \frac{1}{2}(\lambda_{12}+1) \end{pmatrix} \begin{pmatrix} H_2^{\text{in}} \\ H_2^{\text{out}} \end{pmatrix}. \tag{2.81}$$

In free propagating region, since the propagation is straight but oblique across the layer, it reads

$$\begin{pmatrix} H_2^{\text{in}} \\ H_3^{\text{out}} \end{pmatrix} = \begin{pmatrix} 0 & \mathrm{e}^{\frac{\mathrm{i}\omega}{c} n_2 d_2 \cos\theta_2} \\ \mathrm{e}^{-\frac{\mathrm{i}\omega}{c} n_2 d_2 \cos\theta_2} & 0 \end{pmatrix}. \tag{2.82}$$

Thus, the matrix M in this case of the oblique incidence with $p-$ polarization becomes

$$\begin{aligned} M = &\begin{pmatrix} 0 & \mathrm{e}^{\frac{\mathrm{i}\omega}{c} n_2 d_2 \cos\theta_2} \\ \mathrm{e}^{-\frac{\mathrm{i}\omega}{c} n_2 d_2 \cos\theta_2} & 0 \end{pmatrix} \cdot \begin{pmatrix} \frac{1}{2}(\lambda_{21}+1) & \frac{1}{2}(\lambda_{21}-1) \\ \frac{1}{2}(\lambda_{21}-1) & \frac{1}{2}(\lambda_{21}+1) \end{pmatrix} \\ &\cdot \begin{pmatrix} 0 & \mathrm{e}^{\frac{\mathrm{i}\omega}{c} n_1 d_1 \cos\theta_1} \\ \mathrm{e}^{-\frac{\mathrm{i}\omega}{c} n_1 d_1 \cos\theta_1} & 0 \end{pmatrix} \cdot \begin{pmatrix} \frac{1}{2}(\lambda_{12}+1) & \frac{1}{2}(\lambda_{12}-1) \\ \frac{1}{2}(\lambda_{12}-1) & \frac{1}{2}(\lambda_{12}+1) \end{pmatrix} \end{aligned} \tag{2.83}$$

In the same way, we obtain a frequency band structure.

2.2.2 Photonic crystals in higher dimensions

In general, a 2D or 3D photonic crystal is formed by locating structures with a different dielectric constant from the background medium in a periodic fashion (Fig. 2.5). Applying the same argument to the layers formed by the scattering centers (atomic layers in a solid crystal), a band gap is formed in the direction of the wave vector. If the band gaps for all of the directions in the Brillouin zone are tuned to the same frequency region, we obtain a photonic crystal with omni-directional frequency band gap, *i.e.* a photonic band gap material [10].

Chapter 3

Topological photonics

In this chapter, we reviews some representative works on topological photonics. We also utilize some ideas included in those studies in the later parts of the thesis. First, we briefly describe the topological invariants of band structures and the bulk-edge correspondence, which is the essence of the topological photonics. The bulk-edge correspondence was first recognized in the quantum hall effect, as the strong relationship between the Chern number and the chiral edge modes. In next, beginning with the formulation of the eigenvalue problem of Maxwell equations for EM waves, the idea of the bulk-edge correspondence is applied to the photonic band structure. Then we discuss the topologically non-trivial photonic band structures and topologically protected photonic edge modes, in various photonic systems from two-dimensional and three-dimensional photonic crystals to other setups such as evanescently coupled waveguides or coupled resonators.

3.1 Bulk edge correspondence

The study of topology in momentum space originates in the finding of the quantum hall effect [1,35]. K. v. Klitzing performed measurements in the Hall bar of the 2D hetero-structure of semiconductors under a strong magnetic field at low temperatures and found that the transverse conductance, the Hall conductance σ_{yx} is quantized in the unit of e^2/h when the longitudinal conductance is absent. The precision of the quantization was so correct that it is expected to be adopted as the new resistance standard [36]. The quantization is explained in two different ways assuming bulk system or presence of an edge.

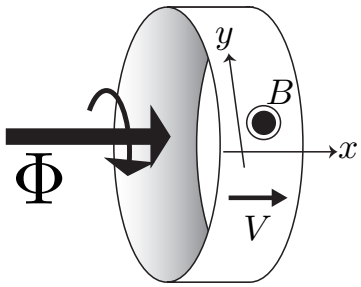

Figure 3.1: The cylinder geometry in the Laughlin argument.

3.1.1 Laughlin's argument

The first explanation for the quantization was given by R. Laughlin. He simplified the Hall bar geometry to a cylinder like in the Fig. 3.1 and toke the following argument. Flux insertion ϕ into the central hole induce the vector potential along the circumference A_l. The vector potential transforms the wave function as

$$\psi(x,y) \to \psi'(x,y) = \mathrm{e}^{\mathrm{i}\int \mathrm{d}y \frac{e}{\hbar} A_l} \psi(x,y). \tag{3.1}$$

The integral on the circumference $A_l L$ equals the amount of the flux ϕ. Then insertion of the flux quanta $\triangle\phi = e/h$, moves the wave number of the electron state as $k_y \to k_y + \triangle k_y (= 2\pi/L)$. Since the entire hamiltonian returns to the original one after the insertion of the flux quanta, the spectrum of the entire spectrum also goes back. However, the occupied state and entire energy may change after the process. In a gapped bulk spectrum such as that of Landau levels, if the insertion process takes place sufficiently slowly compared to the energy gap, the change can be only allowed at edges. Then the energy change after the process should be $\triangle U = neV_x$, where the n is number of electrons moved from one side of edges to the other and the V_x is the potential difference caused by imbalance of electrons between both sides of edges. The electric current I_y is given by the Byers-Yang formula $I_y = \partial U/\partial\phi$ and the linear increasment approximation of the energy as

$$I_y = \frac{\triangle U}{\triangle \phi} = \frac{neV_x}{(h/e)} = n\frac{e^2}{h}V_x.$$

Therefore we conclude that

$$\sigma_{yx} = \frac{I_y}{V_x} = n\frac{e^2}{h}. \tag{3.2}$$

In the above argument, the quantization of the Hall conductance is derived only from the gauge invariance and the bulk gap.

Later, Halperin considered the details of the Laughlin's argument in the geometry of an annular film(similar to the cylinder) and rationalized the electron transportation from one side edge to the other by the chiral edge modes, which propagates along the edge unidirectionally [4]. Also, the Hall conductance in the quantum Hall state was given by the chiral edge modes. Therefore, the first explanation is given by considering the presence of edge and edge modes.

3.1.2 Berry phase

The Berry phase [37] is the most fundamental component in the topological argument of band structures. Although at the time of the derivation of the TKNN formula [2], which is described in the following, the expression was given without the Berry curvature, now the Hall conductance is expressed by the integral of the Berry curvature over the entire 2D Brillouin zone. At first, Berry noticed that the phase other than the dynamical phase could be non-trivial when it is compared after an adiabatic process returning to the original system. The Schrödinger equation is written as

$$\mathrm{i}\hbar\frac{\partial}{\partial t}|\psi\rangle = H(\boldsymbol{R})|\psi\rangle, \tag{3.3}$$

where the hamiltonian depends on certain parameters $\boldsymbol{R} = \{R_1, R_2, \cdots\}$. We write the eigenstate for $\boldsymbol{R}$, $H(\boldsymbol{R})|n(\boldsymbol{R})\rangle = E(\boldsymbol{R})|n\rangle$ and assume that each phase is defined smoothly. If the parameter remains to be $\boldsymbol{R}_0$, the time dependence of the Schrödinger equation is separated and the state evolves as

$$|\psi(t)\rangle = \mathrm{e}^{-\mathrm{i}\hbar E(\boldsymbol{R}_0)t}|n(\boldsymbol{R}_0)\rangle. \tag{3.4}$$

However, if the $\boldsymbol{R}$ varies in time, the separation of variables is no more allowed. In a evolution of $\boldsymbol{R}$ on a closed path, if the variation is sufficiently slow compared to the excitation gap, the state at the end of the process goes back to the original state but the its phase is not trivial. That is, if we assume an additional phase factor $\mathrm{e}^{\mathrm{i}\gamma}$ as

$$|\psi(T)\rangle = \mathrm{e}^{\mathrm{i}\gamma}\mathrm{e}^{-\mathrm{i}\int_0^T E(\boldsymbol{R}(t))}|n(\boldsymbol{R}_0)\rangle, \tag{3.5}$$

the γ can be nonzero. Indeed

$$\mathrm{i}\hbar\frac{\partial}{\partial t}|\psi(t)\rangle = \mathrm{i}\hbar\frac{\partial}{\partial t}\mathrm{e}^{\mathrm{i}\gamma(t)}\mathrm{e}^{\frac{1}{\mathrm{i}\hbar}\int \mathrm{d}t\, E(\boldsymbol{R}(t))}|n(\boldsymbol{R}(t))\rangle =$$

$$-\hbar\dot{\gamma}(t)|n(\boldsymbol{R}(t))\rangle + E(\boldsymbol{R}(t))|n(\boldsymbol{R}(t))\rangle + \mathrm{i}\hbar\frac{\partial}{\partial t}|n(\boldsymbol{R}(t))\rangle = E(\boldsymbol{R}(t))|n(\boldsymbol{R}(t))\rangle.$$

Taking the inner product with $\langle n(\boldsymbol{R}(t))|$,

$$\dot{\gamma}(t) = \mathrm{i}\langle n(\boldsymbol{R}(t))|\frac{\partial}{\partial t}|n(\boldsymbol{R})(t)\rangle$$

$$\gamma = \int_0^T \mathrm{d}t\dot{\gamma}(t) = \mathrm{i}\int_0^T \mathrm{d}t\langle n(\boldsymbol{R}(t))|\frac{\partial}{\partial t}|n(\boldsymbol{R}(t))\rangle$$
$$= \mathrm{i}\oint \mathrm{d}\boldsymbol{R}\cdot\langle n(\boldsymbol{R})|\partial_{\boldsymbol{R}}|n(\boldsymbol{R})\rangle = \mathrm{i}\oint \mathrm{d}\boldsymbol{R}\cdot\boldsymbol{A}(\boldsymbol{R}), \quad (3.6)$$

where the $\boldsymbol{A}(\boldsymbol{R})$ is the berry connection. Since the additional phase only depends on the path of the adiabatic process, it is also called as the geometrical phase. Due to the normalization $\langle n|n\rangle = 1$ and $\partial_{\boldsymbol{R}}\langle n(\boldsymbol{R})|n(\boldsymbol{R})\rangle = 0$, the Berry connection is pure imaginary

$$(\partial|n(\boldsymbol{R})\rangle)^\dagger|n(\boldsymbol{R})\rangle + \langle n(\boldsymbol{R})|\partial_{\boldsymbol{R}}n(\boldsymbol{R})\rangle = \{\langle n(\boldsymbol{R})|\partial_{\boldsymbol{R}}|n(\boldsymbol{R})\rangle\}^* + \langle n(\boldsymbol{R})|\partial_{\boldsymbol{R}}|n(\boldsymbol{R})\rangle = 0$$
$$\{\langle n(\boldsymbol{R})|\partial_{\boldsymbol{R}}|n(\boldsymbol{R})\rangle\}^* = -\langle n(\boldsymbol{R})|\partial_{\boldsymbol{R}}|n(\boldsymbol{R})\rangle = 0 \quad (3.7)$$

We can introduce the Berry curvature

$$B_{\mu\nu}(\boldsymbol{R}) = \partial_\mu A_\nu(\boldsymbol{R}) - \partial_\nu A_\mu(\boldsymbol{R}), \quad (3.8)$$

if the dimension of the parameter $\boldsymbol{R}$ is less than three, which is quite general situation since any two band degeneracy is described with the three real parameters, the Berry curvature can be express by

$$\boldsymbol{B} = \nabla_{\boldsymbol{R}}\times\boldsymbol{A}(\boldsymbol{R}). \quad (3.9)$$

From Stokes' theorem the Berry phase γ is given by

$$\gamma = \int_S \mathrm{d}\boldsymbol{s}\cdot\boldsymbol{B}(\boldsymbol{R}), \quad (3.10)$$

where integral is performed on the surface closed by the path C and the $\boldsymbol{s}$ is the normal vector to the surface at the point. Note that we only imposed that the phases of the eigenstates should be continuous and there exists arbitrariness. If the phases of eigenstates are changed to the other continuous phase distribution as $|n(\boldsymbol{R})\rangle \to \mathrm{e}^{\mathrm{i}f(\boldsymbol{R})}|n(\boldsymbol{R})\rangle$, the Berry connection transforms in the same way as the gauge transformation of the vector potential under the gauge transformation

$$\boldsymbol{A}(\boldsymbol{R}) \to \boldsymbol{A}(\boldsymbol{R}) + \nabla f(\boldsymbol{R}). \quad (3.11)$$

On the other hand, the Berry curvature does not change since $\nabla_{\boldsymbol{R}}\times f(\boldsymbol{R}) = 0$. Then, the Berry curvature $\boldsymbol{B}$ is the momentum space analogue of the magnetic field and the Berry phase γ is the magnetic flux.

Indeed, the Berry curvature can be given an explicit gauge independent expression.

$$\boldsymbol{B} = \nabla\times\boldsymbol{A} = \nabla\times\langle n|\nabla|n\rangle = \langle\nabla n|\times|\nabla n\rangle = \sum_{m\neq n}\langle\nabla n|m\rangle\times\langle m|\nabla n\rangle$$

From the relation $H|n\rangle = E_n|n\rangle$ and orthogonality between eigenstates,

$$\langle m|\partial n\rangle = \frac{\langle m|\partial H|n\rangle}{E_n - E_m}, \qquad \langle\partial n|m\rangle = -\langle m|\partial n\rangle = \frac{\langle n|\partial H|m\rangle}{E_n - E_m},$$

then the Berry curvature is written as

$$\boldsymbol{B} = \sum_{m\neq n}\frac{\langle n|\nabla H|m\rangle\times\langle m|\nabla H|n\rangle}{(E_n - E_m)^2}. \quad (3.12)$$

Also from this expression, it is observed that the intensity depends on the square inverse of the energy gap.

3.1.3 TKNN formula

On the other hand, the quantization is derived from bulk. Within the linear response theory, the Bubo formula for the off-diagonal conductance of a 2D electron gas is derived by Thouless, Kohmoto, Nightingale and den Nijs [2]

$$\sigma_{xy} = \frac{\mathrm{i}e^2}{\hbar}\int \frac{\mathrm{d}k_1\mathrm{d}k_2}{(2\pi)^2}\sum_{\varepsilon_\alpha<\varepsilon_F}\sum_{\varepsilon_\beta>\varepsilon_F}\frac{\langle u_\alpha|\partial_{k_x}\tilde{H}|u_\beta\rangle\langle u_\beta|\partial_{k_y}\tilde{H}|u_\alpha\rangle - \langle u_\alpha|\partial_{k_y}\tilde{H}|u_\beta\rangle\langle u_\beta|\partial_{k_x}\tilde{H}|u_\alpha\rangle}{(\varepsilon_\alpha-\varepsilon_\beta)^2}, \tag{3.13}$$

where the indecies for $\vec{k}$ are neglected and the $\tilde{H} = \tilde{H}(\vec{k})$ is the one body hamiltonian and the $|u_\alpha\rangle$ is the Bloch states with eigenenergy $\epsilon_\alpha(\vec{k})$. This quantity is quantized and if the fermi energy lies in the band gap and the band gap is kept, continuous change of the hamiltonian does not alter the value and thus it is a topological quantity [38]. Also the integrand is given by the Berry curvature $B(\vec{k})$ [39], in the expression of Eq. (3.12). Then, from Stokes' theorem the integral of the $B(\vec{k})$ over the entire 2D Brillouin zone becomes the line integral of the Berry connection $\vec{A}(\vec{k})$ on the path enclosing the Brillouin zone. If the $\vec{A}(\vec{k})$ is defined smoothly and uniquely in the entire Brillouin zone, contributions of line integrals on counter-propagating paths cancel and the integral vanishes. If the $\vec{A}(\vec{k})$ is not defined consistently over the entire Brillouin zone, it is smoothly defined only within patches which cover the Brillouin zone and the integral becomes the line integral of the *difference* of the $\vec{A}(\vec{k})$ between patches along the boundary. Then it becomes the sum of winding numbers and must be $2\pi i n$ with n being an integer. The integral is related to the first Chern number [40]

$$\int \mathrm{d}^2k\ \boldsymbol{B}(\boldsymbol{k}) = 2\pi\mathrm{i}\ C \qquad (C \in \mathbf{Z}). \tag{3.14}$$

Finally, the Hall conductance is

$$\sigma_{xy} = -\sum_n \frac{e^2}{h}C_n, \tag{3.15}$$

where the C_n is the Chern number of the $n-$th band and the summation is taken over bands below the fermi energy. Therefore the quantized Hall conductance is derived from the bulk property.

The Chern number(Eq. 3.14) vanishes under time reversal symmetry(TRS). Time reversal of a spinless state is given by taking the complex conjugate

$$\mathcal{T}|\psi\rangle = |\psi\rangle^*. \tag{3.16}$$

Application of $\mathcal{T}$ to a Bloch state relates the Berry connection at points $\vec{k}$ and $-\vec{k}$ as $\vec{A}(-\vec{k}) = \vec{A}(\vec{k})$. This leads to the relation $\vec{B}(-\vec{k}) = -\vec{B}(\vec{k})$. Then the Berry curvature at $\vec{k}$ and $-\vec{k}$ cancels in the integral(Eq. 3.14). The TRS of the quantum hall state is broken by the uniform magnetic field.

3.1.4 The bulk-edge correspondence

Thus far, two way of explanations are given for the quantization of the Hall conductance. Since both explanations correctly gives the quantized Hall conductance, they are expected to have a deep relationship. This relationship is well established in the tight-binding model of the square lattice under magnetic field. Hatsugai solved the problem by the transfer matrix method and in the Laughlin's argument, he related the Hall conductance to the linking number of the edge modes at fermi energy$\sigma^{\mathrm{edge}} = \frac{e^2}{h}I(C(\varepsilon_F))$ [5]. He also found that the Chern number of a band is given by the difference of the linking number of edge modes in the gap above and below the band $C_j = I(C_j) - I(C_{j-1})$ [6]. As a consequence, the coincidence of two quantized quantities is derived

$$\sigma^{\mathrm{bulk}} = \frac{e^2}{h}\sum_{j(\varepsilon_j<\varepsilon_F)} C_j = \frac{e^2}{h}I(C(\varepsilon_F)) = \sigma^{\mathrm{edge}}. \tag{3.17}$$

This relationship itself is essential rather than the quantization of the Hall conductance. Indeed, when the Chern number classification is applied to photonic systems, the Chern number itself is not related to any physical quantity but only the bulk edge correspondence is physically meaningful.

3.2 The eigenvalue problem of the Maxwell equations in photonic crystals

The Maxwell equations for EM waves in the current-free and source-free field are given by

$$\nabla \cdot \boldsymbol{D} = 0, \qquad \nabla \cdot \boldsymbol{B} = 0 \tag{3.18}$$

$$\frac{\partial}{\partial t}\boldsymbol{D} = \nabla \times \boldsymbol{H}, \qquad -\frac{\partial}{\partial t}\boldsymbol{B} = \nabla \times \boldsymbol{E} \tag{3.19}$$

$$\boldsymbol{D} = \varepsilon_0 \hat{\varepsilon}\boldsymbol{E}, \qquad \boldsymbol{B} = \mu_0 \hat{\mu}\boldsymbol{H}, \tag{3.20}$$

where the ϵ_0, μ_0 are vacuum permittivity and permeability and the $\hat{\epsilon}, \hat{\mu}$ are relative permittivity and permeability tensor respectively. Generally, the optical responses of $\hat{\varepsilon}, \hat{\mu}$ are frequency dependent $\hat{\varepsilon} = \hat{\varepsilon}(\omega), \quad \hat{\mu} = \hat{\mu}(\omega)$.

If we neglect the nonlinear effects and the Maxwell equations are independent of time, the frequency of the EM field is conserved. Nonlinear effects can change the frequency and there exist interesting cases with the external temporal effects by using the nonlinear effect. Without notice we neglect such a temporal effect and focus on the normal modes.

$$\boldsymbol{H}(\boldsymbol{r}, t) = \mathrm{e}^{-\mathrm{i}\omega t}\boldsymbol{H}(\boldsymbol{r}), \quad \boldsymbol{E}(\boldsymbol{r}, t) = \mathrm{e}^{-\mathrm{i}\omega t}\boldsymbol{E}(\boldsymbol{r}). \tag{3.21}$$

Substituting these into the Eq. (3.19), we obtaine

$$\begin{aligned} \nabla \cdot \boldsymbol{D} = 0 \qquad & \nabla \cdot \boldsymbol{B} = 0 \\ -\mathrm{i}\omega \boldsymbol{D} = \nabla \times \boldsymbol{H}, \quad & \mathrm{i}\omega \boldsymbol{B} = \nabla \times \boldsymbol{E}. \end{aligned} \tag{3.22}$$

These equations are written in the eigenvalue problem as

$$\hat{L}\begin{pmatrix} \boldsymbol{E} \\ \boldsymbol{H} \end{pmatrix} = \omega \hat{R}\begin{pmatrix} \boldsymbol{E} \\ \boldsymbol{H} \end{pmatrix}, \tag{3.23}$$

where the operators $\hat{L}$ and $\hat{R}$ represent

$$\hat{L} = \begin{pmatrix} 0 & \mathrm{i}\nabla\times \\ -\mathrm{i}\nabla\times & 0 \end{pmatrix}, \quad \hat{R} = \begin{pmatrix} \varepsilon_0\hat{\varepsilon} & \hat{\xi} \\ \hat{\zeta} & \mu_0\hat{\mu} \end{pmatrix}, \tag{3.24}$$

and the constraint(Eq.(3.18)) has to be satisfied at the same time. Here as a general form, we set $\vec{D} = \hat{\varepsilon}\vec{E} + \hat{\xi}\vec{H}$ and $\vec{B} = \hat{\zeta}\vec{E} + \hat{\mu}\vec{H}$. The operator $\hat{L}$ is hermitian, because of the vector analysis formula

$$\begin{aligned} \int \mathrm{d}^3 \boldsymbol{A}^*_{\sigma'}(\boldsymbol{r}) \cdot \nabla \times \boldsymbol{B}_\sigma(\boldsymbol{r}) &= \left[\mathrm{i}\nabla \cdot \left\{\boldsymbol{A}^*_{\sigma'}(\boldsymbol{r}) \times \boldsymbol{B}_\sigma(\boldsymbol{r})\right\}\right] - \int \mathrm{d}^3 r\ \boldsymbol{A}^*_{\sigma'}(\boldsymbol{r})\, \mathrm{i}\nabla \times \boldsymbol{B}_\sigma(\boldsymbol{r}) \\ &= \left\{\int \mathrm{d}^3 r\ \boldsymbol{B}^*_\sigma \cdot \mathrm{i}\nabla \times \boldsymbol{A}_{\sigma'}(\boldsymbol{r})\right\}^* \quad , \end{aligned} \tag{3.25}$$

where σ represents the $\vec{E}$ or $\vec{H}$ component. The first term in the right hand side of the first line vanishes if we assume the vanishing or periodic boundary condition. Therefore $\langle\{\vec{E}_1, \vec{H}_1\}|\hat{L}|\{\vec{E}_2, \vec{H}_2\}\rangle = \langle\{\vec{E}_2, \vec{H}_2\}|\hat{L}|\{\vec{E}_1, \vec{H}_1\}\rangle^*$ and the $\hat{L}$ is hermitian. The eigenequation Eq. (3.23) is a generalized eigenvalue problem, namely, the right hand side includes the overlap. For a generalized eigenequation to be formalized, the overlap should be positive definite. This is satisfied if the inner product satisfies

$$(\boldsymbol{E}(\boldsymbol{r}), \boldsymbol{H}(\boldsymbol{r})) \cdot \begin{pmatrix} \varepsilon_0\hat{\varepsilon}(\boldsymbol{r}) & \hat{\xi}(\boldsymbol{r}) \\ \hat{\zeta}(\boldsymbol{r}) & \mu_0\hat{\mu}(\boldsymbol{r}) \end{pmatrix}\begin{pmatrix} \boldsymbol{E}(\boldsymbol{r}) \\ \boldsymbol{H}(\boldsymbol{r}) \end{pmatrix} > 0, \tag{3.26}$$

at arbitrary point $\vec{r}$.

In inhomogeneous medium, the refractive indices varies as $\hat{\varepsilon}(\vec{r})$ and $\hat{\mu}(\vec{r})$ and behaves like an external potential for an electron wave function. The eigenvalue is irrelevant of the energy of the eigenfield. The energy of the EM field is rather related to the norm of the EM field.

Generally, the eigenvalue problem Eqs.3.23,3.24 is frequency dependent. Then, a true solution is obtained by repeatedly solving the eigenequation until the assumed frequency for the $\hat{R}$ gets coincident with the frequency of the eigenvalue obtained by solving the eigenequation. The frequency of the mode depends on the

spatial scale and usually the frequency dependence of the $\hat{R}$ can be neglected in the focused frequencies of the eigenmodes or eigenmodes are obtained per a frequency patch, within which the frequency dependence is negligible.

The hermiticity of the $\hat{R}$ is satisfied if all of the followings are satisfied.

$$\hat{\epsilon}^\dagger = \hat{\varepsilon},\ \hat{\mu}^\dagger = \hat{\mu},\ \hat{\zeta} = \hat{\xi}^\dagger \tag{3.27}$$

The hermiticity is necessary for the eigenmode to be lossless. If the eigenequation is non-hermitian, an eigenvalue is generally complex valued. The complex ω means decay(or gain) of the EM field. Since the norm decays(increase) in time, it means that the energy leakage to outside or absorption by(gain from) a medium.

There is a case in which the EM tensor is not diagonal as in the Eq. (3.23). The appearance of the off diagonal elements means the magnet-optical(ME) coupling and they appear in materials with bi-anisotropy. However if the EM tensor in the Eq. (3.23) is diagonal, the eigenequation can be further simplified. Multiplying the inverse of the EM tensor diag $\left\{(\varepsilon_0\varepsilon)^{-1}, (\mu_0\mu)^{-1}\right\}$ from the left and further operating $\begin{pmatrix} 0 & \mathrm{i}\nabla\times \\ -\mathrm{i}\nabla\times & 0 \end{pmatrix}\begin{pmatrix}\vec{E}\\ \vec{H}\end{pmatrix} = \omega\begin{pmatrix}\varepsilon_0\hat{\varepsilon} & 0\\ 0 & \mu_0\hat{\mu}\end{pmatrix}\begin{pmatrix}\vec{E}\\ \vec{H}\end{pmatrix}$, we obtain two equivalent equations

$$\nabla\times\hat{\varepsilon}^{-1}(\boldsymbol{r})\,\nabla\times\boldsymbol{H}(\boldsymbol{r}) = \left(\frac{\omega}{c}\right)^2\hat{\mu}\boldsymbol{H}(\boldsymbol{r}) \tag{3.28}$$

$$\nabla\times\hat{\mu}^{-1}(\boldsymbol{r})\,\nabla\times\boldsymbol{E}(\boldsymbol{r}) = \left(\frac{\omega}{c}\right)^2\hat{\varepsilon}\boldsymbol{E}(\boldsymbol{r}) \tag{3.29}$$

$$\hat{L}_{H,E}\boldsymbol{f}(\boldsymbol{r}) = \left(\frac{\omega}{c}\right)^2\hat{R}_{H,E}\boldsymbol{f}(\boldsymbol{r}) \tag{3.30}$$

where the $\hat{L}_{H,E} = \vec{\nabla}\times\left\{\hat{\varepsilon}^{-1}, \hat{\mu}^{-1}\right\}\vec{\nabla}\times$, $\hat{R}_{H,E} = \{\hat{\mu}, \hat{\varepsilon}\}$ with the $c^2 = 1/\varepsilon_0\mu_0$ are the diagonal version of the left $\hat{L}$ and the right $\hat{R}$ operators. If the solution is obtained for either $\vec{H}$ or $\vec{E}$, the other is obtained from the Maxwell equation Eq. (3.22).

In a system with transnational invariance, the momentum(wave vector) is conserved. As the name of *photonic crystal* implies, the dielectric constant is periodic in space there and the Maxwell equations are invariant under a discrete lattice translation.

$$\hat{\varepsilon}(\boldsymbol{r}+\boldsymbol{R}) = \hat{\varepsilon}(\boldsymbol{r})\,, \hat{\mu}(\boldsymbol{r}+\boldsymbol{R}) = \hat{\mu}(\boldsymbol{r})\,, \tag{3.31}$$

where the $\vec{R}$ represents a lattice translation $\vec{R} = n_1\vec{a}_1 + n_2\vec{a}_2 + n_3\vec{a}_3 \quad (n_1, n_2, n_3 \in \mathbf{Z})$

In this case, the reduced momentum(Bloch wave vector) defined within the Brillouin zone is a conserved quantity. The eigenstates are given by the Bloch states satisfying

$$\boldsymbol{E}(\boldsymbol{r}+\boldsymbol{R}) = \mathrm{e}^{\mathrm{i}\boldsymbol{k}\cdot\boldsymbol{R}}\boldsymbol{E}(\boldsymbol{r})\,, \quad \boldsymbol{H}(\boldsymbol{r}+\boldsymbol{R}) = \mathrm{e}^{\mathrm{i}\boldsymbol{k}\cdot\boldsymbol{R}}\boldsymbol{H}(\boldsymbol{r})\,, \tag{3.32}$$

where the $\vec{k}$ is given as

$$\boldsymbol{k} = m_1\boldsymbol{b}_1 + m_2\boldsymbol{b}_2 + m_3\boldsymbol{b}_3 \quad m_1, m_2, m_3 \in \mathbf{Z} \tag{3.33}$$

$$\boldsymbol{b}_1 = \frac{2\pi\boldsymbol{a}_2\times\boldsymbol{a}_3}{\boldsymbol{a}_1\times(\boldsymbol{a}_2\times\boldsymbol{a}_3)}, \boldsymbol{b}_2 = \frac{2\pi\boldsymbol{a}_3\times\boldsymbol{a}_1}{\boldsymbol{a}_2\cdot(\boldsymbol{a}_3\times\boldsymbol{a}_1)}, \boldsymbol{b}_3 = \frac{2\pi\boldsymbol{a}_1\times\boldsymbol{a}_2}{\boldsymbol{a}_3\cdot(\boldsymbol{a}_1\times\boldsymbol{a}_2)}. \tag{3.34}$$

Although the vector field of the EM field has three components, the constraint Eq. (3.18) reduce them to two components since the EM waves is a transverse wave. Generally in dielectric material, the relative permeability is almost $\mu_r \simeq 1$(in frequencies higher than microwaves). Without notice, we will only consider the dielectric tensor $\hat{\varepsilon}$ regarding the permeability as $\hat{\mu} = \mu_0\hat{I}$. Under this condition, the eigenequation with respect to $\vec{H}$ is more convenient since the divergence of the right hand side is zero and we can expand it with transverse basis[1].

[1]With the use of plane waves, the transversality condition for $\vec{H}$ allows us to take only two components, whereas the expansion of $\vec{E}$ requires three components producing the one-third of zero eigenvalues.

3.2.1 Symmetry considerations

The transformation of a vector field is given by

$$Rf(r) = \hat{R} f\left(\hat{R}^{-1} r\right), \tag{3.35}$$

where the $\hat{R}$ is a 3×3 matrix that rotates the position vector $\vec{r}$ by the R. In accordance, the transformation of an operator is given by

$$O \to ROR^{-1}. \tag{3.36}$$

First, we consider the change of the left hand side of the eigenequation(Eq. (3.23)) under symmetrical transformations. The left hand side operator is invariant under a usual spatial rotation without inversion $\hat{R}(\nabla\times)\hat{R}^{-1} = \nabla\times$. This is confirmed by examining the transformation of each component under the rotation. In the Maxwell theory of electromagnetism, the $\vec{E}$ field is taken as a vector(odd under inversion) field whereas the $\vec{H}$ field is taken as a pseudo vector field(even under inversion). The broken duality between the $\vec{E}$ and the $\vec{H}$ comes from the vanishing divergence of the magnetic flux $\vec{B}$, namely, the absence of the mono-pole magnet. This difference is more clearly understand by considering the vector potential, which is the essence of the EM field

$$\boldsymbol{E}(\boldsymbol{r}, t) = \frac{\mathrm{d}}{\mathrm{d}t}\boldsymbol{A}(\boldsymbol{r}, t) - \nabla\phi(\boldsymbol{r}, t), \quad \boldsymbol{B}(\boldsymbol{r}, t) = \nabla \times \boldsymbol{A}(\boldsymbol{r}, t), \tag{3.37}$$

and inversion of the vector potential results in

$$R_I \boldsymbol{E}(\boldsymbol{r}) = -\frac{\mathrm{d}}{\mathrm{d}t}\boldsymbol{A}(-\boldsymbol{r}) - \nabla\phi(-\boldsymbol{r}) = -\boldsymbol{E}(-\boldsymbol{r}) \tag{3.38}$$

$$R_I \boldsymbol{B}(\boldsymbol{r}) = (-\nabla\times)(\boldsymbol{A}(-\boldsymbol{r})) = \boldsymbol{B}(\boldsymbol{r}). \tag{3.39}$$

To summarize, the EM field transforms under spatial inversion as

$$R_I \begin{pmatrix} \boldsymbol{E}(-\boldsymbol{r}) \\ \boldsymbol{H}(-\boldsymbol{r}) \end{pmatrix} = \begin{pmatrix} -\boldsymbol{E}(\boldsymbol{r}) \\ \boldsymbol{H}(\boldsymbol{r}) \end{pmatrix}. \tag{3.40}$$

On the other hand, for spatial inversion, the rotation transforms as

$$R_I (\nabla\times) R_I^{-1} = -\nabla\times, \tag{3.41}$$

since the rotation depends on the handedness of the spatial coordinate. As a consequence,

$$\begin{aligned} R_I \begin{pmatrix} 0 & \mathrm{i}\nabla\times \\ -\mathrm{i}\nabla\times & 0 \end{pmatrix} R_I \begin{pmatrix} \boldsymbol{E}(\boldsymbol{r}) \\ \boldsymbol{H}(\boldsymbol{r}) \end{pmatrix} &= R_I \begin{pmatrix} 0 & \mathrm{i}\nabla\times \\ -\mathrm{i}\nabla\times & 0 \end{pmatrix} \begin{pmatrix} -\boldsymbol{E}(-\boldsymbol{r}) \\ \boldsymbol{H}(-\boldsymbol{r}) \end{pmatrix} \\ &= R_I \begin{pmatrix} -\mathrm{i}\{\nabla \times \boldsymbol{H}(\boldsymbol{r}')\}(-\boldsymbol{r}) \\ \mathrm{i}\{\nabla \times \boldsymbol{E}(\boldsymbol{r}')\}(-\boldsymbol{r}) \end{pmatrix} = \begin{pmatrix} \mathrm{i}\nabla \times \boldsymbol{H}(\boldsymbol{r}) \\ -\mathrm{i}\nabla \times \boldsymbol{E}(\boldsymbol{r}) \end{pmatrix} = \begin{pmatrix} 0 & \mathrm{i}\nabla\times \\ -\mathrm{i}\nabla\times & 0 \end{pmatrix} \begin{pmatrix} \boldsymbol{E}(\boldsymbol{r}) \\ \boldsymbol{H}(\boldsymbol{r}) \end{pmatrix}, \end{aligned} \tag{3.42}$$

the $\hat{L}$ is invariant under the spatial rotation.

Next, we examine the TRS. From Eqs. (3.21), the time reversal $T\left\{\vec{E}(\vec{r}, t), \vec{H}(\vec{r}, t)\right\} = \left\{\vec{E}(\vec{r}, -t), \vec{H}(\vec{r}, -t)\right\}$ is given by

$$T \begin{pmatrix} \boldsymbol{E}(\boldsymbol{r}) \\ \boldsymbol{H}(\boldsymbol{r}) \end{pmatrix} = \begin{pmatrix} \boldsymbol{E}^*(\boldsymbol{r}) \\ -\boldsymbol{H}^*(\boldsymbol{r}) \end{pmatrix}. \tag{3.43}$$

Note that the minus sign in front of $\vec{H}^*$ [41]. The sign flip for the $\vec{H}$is necessary to keep the handedness[2]. As a consequence, the time reversal transformation of the $\hat{L}$ is

$$\begin{aligned} T \begin{pmatrix} 0 & \mathrm{i}\nabla\times \\ -\mathrm{i}\nabla\times & 0 \end{pmatrix} T \begin{pmatrix} \boldsymbol{E} \\ \boldsymbol{H} \end{pmatrix} = T \begin{pmatrix} 0 & \mathrm{i}\nabla\times \\ -\mathrm{i}\nabla\times & 0 \end{pmatrix} \begin{pmatrix} \boldsymbol{E}^* \\ -\boldsymbol{H}^* \end{pmatrix} = \\ T \begin{pmatrix} -\mathrm{i}\nabla \times \boldsymbol{H}^* \\ -\mathrm{i}\nabla \times \boldsymbol{E}^* \end{pmatrix} = \begin{pmatrix} \mathrm{i}\nabla \times \boldsymbol{H} \\ -\mathrm{i}\nabla \times \boldsymbol{E} \end{pmatrix} = \begin{pmatrix} 0 & \mathrm{i}\nabla\times \\ -\mathrm{i}\nabla\times & 0 \end{pmatrix} \begin{pmatrix} \boldsymbol{E} \\ \boldsymbol{H} \end{pmatrix}, \end{aligned} \tag{3.44}$$

[2] Sign flip for the $\vec{E}$ instead is also possible.

meaning it is invariant under T.

The transformation of the $\hat{R}$ under rotation R is given by

$$R\begin{pmatrix}\hat{\varepsilon}(\boldsymbol{r}) & 0\\ 0 & \hat{\mu}(\boldsymbol{r})\end{pmatrix}R^{-1}=\begin{pmatrix}\hat{R}\hat{\varepsilon}(\hat{R}^{-1}\boldsymbol{r})\hat{R}^{-1} & 0\\ 0 & \hat{R}\hat{\mu}(\hat{R}^{-1}\boldsymbol{r})\hat{R}^{-1}\end{pmatrix}, \tag{3.45}$$

As for time reversal of the $\hat{R}$, it is invariant if the EM tensor is given by real valued quantities.

The invariance of the eigenequation under spatial inversion is more clearly seen from the Eq.(3.30), where the eigenvalue appears as the ω^2. The invariance of the left hand side of the (3.30) under inversion is shown below

$$\left(R_I\nabla\times\hat{\varepsilon}^{-1}\nabla\times R_I\right)=(R_I\nabla\times R_I)\left(R_I\hat{\varepsilon}^{-1}R_I\right)(R_I\nabla\times R_I)=(-\nabla\times)\left(R_I\hat{\varepsilon}^{-1}R_I\right)(-\nabla\times)\,. \tag{3.46}$$

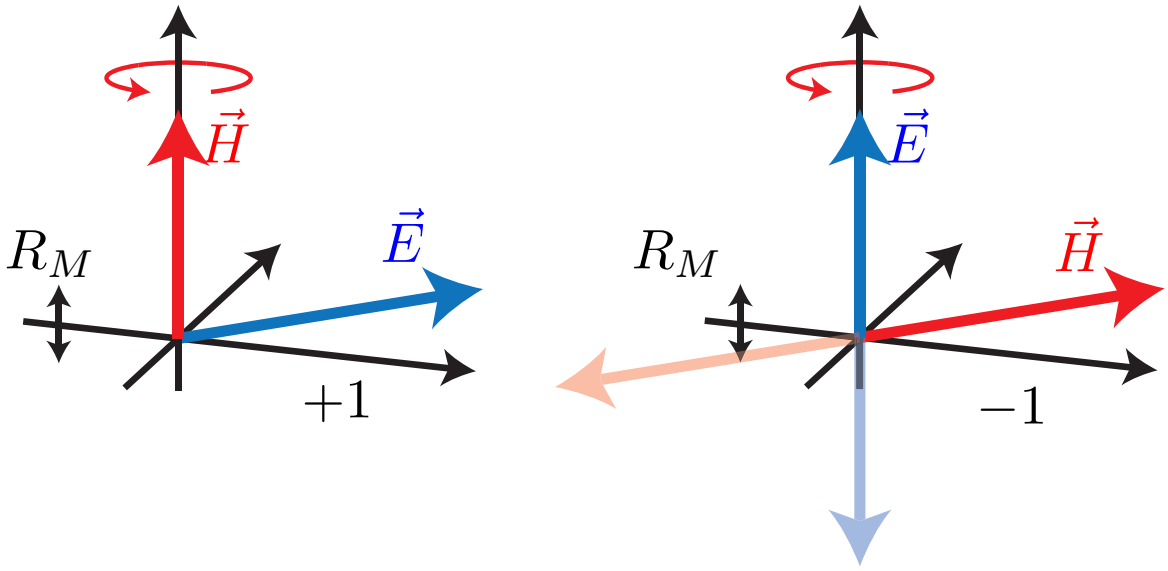

Figure 3.2: The polarization are classified into TE(+1) mode and TM(-1) mode according to the eigenvalue of $R_M(=C_{2z}I)$.

The reduced equation in 2D systems

If the EM tensor is independent of the $z-$coordinate, namely the system is uniform in the z direction, the $z-$component of the momentum k_z is a conserved quantity and we can take the elect magnetic field as $\left\{\vec{E}(\vec{r}),\vec{H}(\vec{r})\right\}=\left\{e^{ik_zz}\vec{E}(x,y)\,e^{ik_zz}\vec{H}(x,y)\right\}$. If we further restrict it to $k_z=0$, the entire equation is independent of z and thus we obtain a two dimensional problem. The two dimensionality allows us to classify the solutions into transverse electric(TE) mode and transverse magnetic(TM) mode, which reduce vector fields into scalar fields. The two dimensionality always gives the mirror symmetry with respect to the 2D plane $R_M:(x,y,z)\to(x,y,-z)$. Since the mirror operation is decomposed as $R_M\to R_IC_{2z}$, the left hand side operator is invariant under the mirror. The $\vec{E}$ field transforms as in usual mirror $\left(E_x,E_y,E_z\right)\to\left(E_x,E_y,-E_z\right)$, where as the pseudo vector field $\vec{H}$ transforms as the $\pi-$rotation around the $z-$axis $\left(H_x,H_y,H_z\right)\to\left(-H_x,-H_y,H_z\right)$. Since $R_M^2=1$, we can take the λ as 1 or -1. The $\lambda=+1$ means that $\vec{H}$ field is perpendicular to the 2D plane and the $\vec{E}$ field is completely included within the 2D plane and this solution is called as the TE-mode. The $\lambda=-1$ means(see Fig. 3.2), on the other hand, the $\vec{H}$ field is completely included within the 2D plane and the $\vec{E}$ field is perpendicular to the plane, and this is called as the TM-mode. Therefore, TE or TM mode decomposition gives us the scalar equation about the $z-$component[3]. If either field is obtained, the another(a 2D vector field) is obtained from the Maxwell equation Eq. (3.22).

[3]When the $\vec{E}$ field is polarized in the z(TM-mode), the transversality condition $\nabla\cdot\hat{\varepsilon}\vec{E}=\hat{\varepsilon}\nabla\cdot\vec{E}$ is automatically satisfied.

3.2.2 Defining gauge invariant quantities in photonic band structures

Since the eigenvalue problem for the EM field is a generalized eigenvalue problem, the formalism for the Berry connection is slightly different from the case of the Schrödinger equation. Moreover, the frequency dependence of the eigenequation raises additional ambiguities. Due to the generalized eigenvalue problem, the inner product of the states are defined with the overlap as

$$(\{\boldsymbol{E}_1(\boldsymbol{r}), \boldsymbol{H}_1(\boldsymbol{r})\}, \{\boldsymbol{E}_2, \boldsymbol{H}_2\}) = \int \mathrm{d}r^3 \, \{\boldsymbol{E}_1^*(\boldsymbol{r}), \boldsymbol{H}_1^*(\boldsymbol{r})\} \cdot \hat{R} \begin{pmatrix} \boldsymbol{E}_2(\boldsymbol{r}) \\ \boldsymbol{H}_2(\boldsymbol{r}) \end{pmatrix}. \tag{3.47}$$

The eigenstates of the generalized eigenvalue problem are orthogonalized under the inner product(Eq. 3.47). The norm of the EM field is not required to be normalized since it means the energy of the field, which is continuous, instead of the number of particles, which is discrete. However, normalization is essential for defining a gauge invariant quantity. Since the $\hat{R}$ is assumed to be positive definite, the square root $\hat{R}^{1/2}$ can be obtained and we can redefine the eigenstate as

$$\left\{\tilde{\boldsymbol{E}}, \tilde{\boldsymbol{H}}\right\}^t = \hat{R}^{1/2} \{\boldsymbol{E}, \boldsymbol{H}\}^t, \tag{3.48}$$

and the inner product is instead given as

$$(\{\tilde{\boldsymbol{E}}_1, \tilde{\boldsymbol{H}}_1\}, \{\tilde{\boldsymbol{E}}_2, \tilde{\boldsymbol{H}}_2\}) = \int \mathrm{d}^3 r \, \{\tilde{\boldsymbol{E}}_1^*(\boldsymbol{r}), \tilde{\boldsymbol{H}}_2^*(\boldsymbol{r})\} \cdot \begin{pmatrix} \tilde{\boldsymbol{E}}_2(\boldsymbol{r}) \\ \tilde{\boldsymbol{H}}_2(\boldsymbol{r}) \end{pmatrix}. \tag{3.49}$$

This definition is convenient for defining the Berry connection. The normalization is necessary for defining the Berry connection

$$\langle \tilde{u}_n(\boldsymbol{k}) | \tilde{u}_n(\boldsymbol{k}) \rangle = (\{\tilde{\boldsymbol{E}}_n(\boldsymbol{k}), \tilde{\boldsymbol{H}}_n(\boldsymbol{k})\}, \{\tilde{\boldsymbol{E}}_n(\boldsymbol{k}), \tilde{\boldsymbol{H}}_n(\boldsymbol{k})\}) = 1. \tag{3.50}$$

Then, the Berry connection in the eigenstates of the EM fields are given as

$$A_{n,\mu}(\boldsymbol{k}) = \langle \tilde{u}_n(\boldsymbol{k}) | \partial_{k_\mu} | \tilde{u}_n(\boldsymbol{k}) \rangle, \tag{3.51}$$

where the μ represents the coordinate index($\mu = x, y, z$). The $A_{n,\mu}(k)$ defined above is a pure imaginary quantity for the same reason as in the case of the Schrödinger equation. In general, the optical responce $\hat{R}$ is frequency dependent. Therefore with dispersion, the derivative ∂_{k_μ} includes the variation of the optical constant

$$\partial_\mu |\tilde{u}_n(\boldsymbol{k})\rangle = \partial_\mu \hat{R}(\omega_{\boldsymbol{k}}) \{E_n(\boldsymbol{k}), H_n(\boldsymbol{k})\}^t = (\partial_\mu \hat{R}(\omega_{\boldsymbol{k}}))\{E_n(\boldsymbol{k}), H_n(\boldsymbol{k})\}^t + \hat{R}(\omega_{\boldsymbol{k}})(\partial_{k_\mu} \{E_n(\boldsymbol{k}), H_n(\boldsymbol{k})\}^t). \tag{3.52}$$

Once the Berry connection is obtained, the Berry curvature and consequently the Chern number is obtained in the same as the Schrödinger equation. For the purpose of obtaining topological invariants such as the Chern number, since a continuous change does not abruptly varies the value, the frequency dependence of the $\hat{R}(\omega_{\boldsymbol{k}})$ can be reasonably neglected if the frequency dependence not so strong within the band. As mentioned before, the Chern number of the photonic bands is not related to any physical quantity but it predicts the number of edge modes in the gap regardless of specific shape of the boundary. Since EM filelds does not interact with external magnetic field in the vacuum, TRS for the EM fields is not broken just applying magnetic field. TRS breaking effect is caused by the use of a magnet optical material.

3.3 Topological edge modes of light in photonic crystals

In 2006, S. Raugh and F.D.M.Haldane suggested that the idea of the Haldane's 2D honeycomb lattice can also be realized in a photonic crystal [16, 17], which is a totally different system from an electron system and even not a quantum sort. This finding broke a stereotype that the quantum hall effect is unique to a quantum systems and demonstrated that it is universal in the systems having a gap. The key point to make a topologically non-trivial band structure in 2D system is the breaking of TRS and they proposed to use a gyro-electric material. In

the application of external magnetic field, the gyro-electric material is represented in the convenient coordinate as

$$\hat{\varepsilon} = \begin{pmatrix} \varepsilon & -i\kappa & 0 \\ i\kappa & \varepsilon & 0 \\ 0 & 0 & \varepsilon_z \end{pmatrix}, \tag{3.53}$$

where the κ cause a time-reversal breaking and the difference between ε and ε_z is the anisotropy due to application of magnetic field in the z direction. The diagonalization of the tensor gives circularly polarized states as eigenvectors and gives different eigenvalues, that is, different refractive indices for opposite circular polarization meaning the Faraday effect. They focused on the photonic band structure of TE-mode of the 2D triangular photonic crystal. The photonic band structure has a clear dirac cone-like dispersion near K or K' points between the 2nd and 3rd TE-modes. This is simply explained from a point-group perspective and the separation of two-degeneracy points, namely lacking of mirror symmetry in the group of k. Also, the existence of degeneracy itself is explained from the both existence of spatial inversion and TRS. In the existence of both symmetries, the effective 2×2 matrix representing the degeneracy is given by only two pauli matrices. Therefore, under the both symmetries, the existence of degeneracy is topologically stable. By breaking the either of them, the degeneracy is eliminated. By breaking a spatial inversion symmetry, the degeneracy at K or K' point dissolve and the dirac cones become massive. The breaking of inversion symmetry is realized by breaking the inversion symmetry of the inner-structure such as deformation of a circle into a triangle or modulating a dielectric constant to break the symmetry. On the other hand, the degeneracy can also be solved by breaking the time reversal symmetry, namely applying an external magnetic field to the gyro-electric material. This makes the same effect as the Haldane mass in the Haldane model. Then, the transition between topologically non-trivial and trivial band structure can be discussed parallelly to the Haldane's original lattice model.

Inspired by the suggestion, the M. Soljacic and J.D.Joannpolos group at MIT, who has a great experience on engineering of photonic systems, considered more realistic situation [18] and later, they actually observed the robust propagation of the chiral edge modes of light [19]. To break TRS of a photonic system, they used a gyro-magnetic material (YIG) instead of gyro-electric material since they noticed the TRS breaking effect is relatively large for TM-modes. The eigenequation for TM-modes with the gyro-magnetic material is written as

$$\nabla \times \hat{\mu} \times \vec{E} = \hat{\epsilon} \left(\frac{\omega}{c}\right)^2 \vec{E}, \tag{3.54}$$

where the optical indices $\hat{\mu}$, $\hat{\varepsilon}$ with in the material is given by

$$\hat{\mu} = \begin{pmatrix} \mu & -i\kappa & 0 \\ i\kappa & \mu & 0 \\ 0 & 0 & \mu_z \end{pmatrix}, \quad \hat{\varepsilon} = \begin{pmatrix} \varepsilon & 0 & 0 \\ 0 & 0 & \varepsilon \\ 0 & 0 & \varepsilon \end{pmatrix}. \tag{3.55}$$

They focused the TM-mode band structure of the 2D square lattice, which is known as the first discovery of the dirac cone with quadratic dispersion [42]. It is rarely found in electronic systems because of internal spin degree. For the square lattice with complete internal symmetry, the symmetry point with multiple irreducible representation lies on the inversion symmetric point, and then two dirac points pile up. As a consequence, the dispersion at degeneracy becomes quadratic. For fermionic system, the two band degeneracy becomes linear due to the Kramers degeneracy. The existence of the dirac-cone is not essential here and we can make the same argument just by placing the two degeneracy points on the same point in stead of different two points. Further, the quadratic dependence dramatically reduces the dispersion and the effect of TRS breaking is great compared to the case of the linear dispersion. As a consequence, it is great advantage to create a distinctive band cap favorable to an experiment. In their theoretical work [18], assuming YIG as a composing material, the yttrium compound is the most known magnetoptical materials, as a they obtained the gap as large as $\triangle\omega \simeq 0.05(2\pi c/a)$ for the topological gap in the GHz frequency region with external magnetic field of 1600 gauss. To study the chiral edge modes of light as a consequence of non-zero Chern number, they set up the system surrounded by photonic crystal with a trivial gap in the same frequency region to prevent light from leaking outside. In addition to showing the chiral edge mode dispersion of light, they demonstrated its robust unidirectional propagation by FDTD simulation of the Maxwell equation. To test the robustness, they put an obstacle along the interface and the light indeed keeps going forward avoiding the obstacle like a dissipation less flow of a superfluid state.

After the theoretical work, they achieved an experimental observation of the chiral edge mode of EM waves. In their experiment [19], instead of arranging the cylinders with an infinite length, they used cylinder, and cladded over them by a copper board, which effectively behaves like a 2D system for a specific condition. The boundary was also made by copper cladding. They observed the chiral edge modes by putting two antennas for input and output ports and measured the transmittance. The large contrast of the transmittance between forward and backward propagation shows the unidirectionality of the chiral edge mode. Further, the tendency does not change when an obstacle made of copper is placed in the middle of two ports, demonstrating the robustness of the chiral edge modes.

The chiral edge modes of light in the vacuum termination was first studied by Ochiai and Onoda [43]. Unlike an electron in a solid, a light mode is not confined within a photonic crystal unless it lies lower than the light cone. In their study, the dispersion in the finite width system including leakage was dealt with the scattering matrix method for the layered structure [44, 45].

Literally, a topologically non-trivial state is not a fine-tuned state. Transition from topologically trivial to non-trivial state is well shown by changing the radius of the internal cylinder as an example. The most simple trivial band is that of an array of isolated atoms. Because of the absence of tunneling effects in the system, the band is flat. When the eigenstates in the entire Brillouin zone are given by the closed set of localized orbitals, total of Chern numbers of those bands must vanish. In this case, the flat band is given by a single localized orbital of the isolated orbit, the Chern number is obviously zero. Fixing the magnetic field(Voigt's ratio), we consider to change th radius of the cylinder.

In the small radius limit of the internal cylinder, the photonic band structure is trivial. Increasing the radius, the trivial gap once closes and reopens getting topologically non-trivial. Increasing the radius of the cylinder, the transition occurs again. This is understood by converting the complementary region to filled region, namely at the large radius limit, the system get near uniform again and the band structure becomes trivial again.

Further sticking into the higher degeneracy by fine tuning the parameter and simultaneous gap opening with a TRS breaking effect, the photonic band gap with Chern number larger than two was achieved [46, 47]. In general, a photonic band structure gets highly tangled going higher in the frequency and we have more opportunities to have a gap with greater chern numbers if a gap is found in the region.

In other aspects, the Berry curvature in the $k-$space is related with the vorticity of the wave function in the real space. The light with vortex is expect to be applied to the production of the orbital angular momentum beam.

Metamaterial photonic topological insulator

The photonic chiral edge modes in the previous sections requires an external magnetic field to break TRS. The magnetic filed of 1600 gauss is hard for daily use. The Kane-Mele model [8] is two copies of the Haldane model with opposite spin polarization, each of which feels a magnetic field coming from the spin-orbit coupling with the other polarization. It has TRS and does not require an external magnetic field. A photonic analogue of the Kane-Mele model was proposed with the use of meta-material by Khanikaev *et.al.* [48], which also does not require an external magnetic field. The optical reaction from the meta material cause a bi-anisotropy, which in their set up, effectively given as

$$\begin{pmatrix} 0 & \mathrm{i}\nabla\times \\ -\mathrm{i}\nabla\times & 0 \end{pmatrix}\begin{pmatrix} \boldsymbol{E} \\ \boldsymbol{H} \end{pmatrix} = \left(\frac{\omega}{c}\right)^2 \begin{pmatrix} \hat{\varepsilon} & \hat{\xi} \\ \hat{\zeta}^\dagger & \hat{\mu} \end{pmatrix}\begin{pmatrix} \boldsymbol{E} \\ \boldsymbol{H} \end{pmatrix}, \tag{3.56}$$

where from reciprocity $\hat{\zeta} = \hat{\xi}^\dagger$, and it is written as

$$\hat{\xi} = \begin{pmatrix} 0 & \mathrm{i}\chi_{xy} & 0 \\ \mathrm{i}\chi_{yx} & 0 & 0 \\ 0 & 0 & 0 \end{pmatrix}. \tag{3.57}$$

Most simply, those elements are given by an anti-symmetric form $\chi_{yx} = -\chi_{xy}$. Note that this equation is invariant under bosonic time reversal operation $T\left(\vec{E}, \vec{H}\right)^t \to \left(\vec{E}^*, -\vec{H}^*\right)^t$, since

$$T\begin{pmatrix} 0 & -\mathrm{i}\nabla\times \\ \mathrm{i}\nabla\times & 0 \end{pmatrix}T = \begin{pmatrix} 0 & -\mathrm{i}\nabla\times \\ \mathrm{i}\nabla\times & 0 \end{pmatrix}, \quad T\begin{pmatrix} \hat{\epsilon} & \hat{\zeta} \\ \hat{\zeta}^\dagger & \hat{\mu} \end{pmatrix}T = \begin{pmatrix} \hat{\epsilon}^* & -\hat{\zeta}^* \\ -\left(\hat{\zeta}^\dagger\right)^* & \hat{\mu}^* \end{pmatrix} = \begin{pmatrix} \hat{\epsilon} & \hat{\zeta} \\ \hat{\zeta}^\dagger & \hat{\mu} \end{pmatrix}, \tag{3.58}$$

and specifically in this case, $\hat{\epsilon}^* = \hat{\epsilon}$, $\hat{\mu}^* = \hat{\mu}$, $-\hat{\zeta}^* = \hat{\zeta}$. The Kane-Mele model is a spin-full 4-band model having a spin degeneracy in addition to a pseudo-spin degeneracy. To mimic the 4-band model, the permeability $\hat{\mu}$ is set to equal $\hat{\varepsilon}$ and this is achievable with the use of meta-material. With $\hat{\mu} = \hat{\varepsilon}$, the TE-modes($H_z$ polarization) and TM-modes(E_z polarization) are completely degenerate if $\chi_{xy} = 0$, if $\chi_{xy} \neq 0$, the TE or TM polarization is not conserved. We can take linear combination of TE and TM modes deliberately and the optical spin polarization $\psi_\pm = E_z \pm H_z$ becomes eigenstates in the case of $\chi_{xy} \neq 0$ and its time-reversal is given by $T\psi_\pm = \psi_\mp$. Such an effect as the term χ_{xy} is called as the optical activity, which is not uncommon in nature and seen in materials such as liquid crystals, though it is usually small $|\chi_{xy}| << 1$. In contrast, the large optical activity is achievable with the use of meta-materials [49] such as split-ring resonators [50–52], $\Omega-$particles [53] or metallic helices [54]. Due to the equivalence $\hat{\varepsilon} = \hat{\mu}$ and $\hat{\zeta} = \hat{\xi}^\dagger$, we can take the EM field as

$$\boldsymbol{E} = \begin{pmatrix} E_x \\ E_y \\ E_z \end{pmatrix}, \quad \boldsymbol{H} = \begin{pmatrix} -E_x \\ -E_y \\ E_z \end{pmatrix} \tag{3.59}$$

and $\psi_\pm = \boldsymbol{E} \pm \boldsymbol{H}$. Noting this, the right hand side of the eigenequation3.56 reduces to

$$\begin{pmatrix} \hat{\varepsilon} & \hat{\xi} \\ \hat{\xi}^\dagger & \hat{\varepsilon} \end{pmatrix} \begin{pmatrix} \boldsymbol{E} \\ \pm\boldsymbol{H} \end{pmatrix} \to \hat{\tilde{\varepsilon}}_\pm = \begin{pmatrix} \varepsilon & -\pm i\chi & 0 \\ \pm i\chi & \varepsilon & 0 \\ 0 & 0 & \varepsilon_z \end{pmatrix}. \tag{3.60}$$

As a consequence, in this specific case, the eigenequation for ± polarization reduces to

$$\nabla \times \hat{\tilde{\varepsilon}}_\pm^{-1} \nabla \times \psi_\pm = \left(\frac{\omega}{c}\right)^2 \psi. \tag{3.61}$$

Therefore, the optical activity χ reduces the 4-band degeneracy to two spin ± degeneracies and creates the band gap with the same TRS breaking effect as in the gyrotropic materials with opposite directions for opposite polarizations. Of course, the topological non triviality does not require the strict equivalence $\hat{\varepsilon} = \hat{\mu}$, but it is the matter of degree. In practice, a difference inevitably arise between $\hat{\epsilon}$ and $\hat{\mu}$. The in-equivalence breaks the degeneracy between ±-spin polarization, and the two bands are disconnected with the trivial Chern number. As a result, the band structure is trivial in reality and of course, the edge modes are disconnected. However, a tiny difference does not gives abrupt distraction and the smaller the equivalence is, the more distinctive the edge mode is, though it no more connects two bulk bands.

Let us further mention about the relation to the Kane-Mele model of electrons. The edge state protected by the TRS and Z_2 characterization of the topological band structure in the Kane-Mele model is essentially the consequence of fermionic time reversal operator satisfying $T_F^2 = -1$, namely the Kramers degeneracy. However, the photonic spin-Hall system considered here is the bosonic system and follows the bosonic time reversal operator $T_B^2 = 1$. Thus, the corresponding Z_2 characterization is impossible.

Photonic topological insulator with tellegene medium

In next, let us consider a magnet-electric coupling of the type The magnet-electric coupling of the type

$$\hat{\xi} = \begin{pmatrix} 0 & \chi & 0 \\ -\chi & 0 & 0 \\ 0 & 0 & 0 \end{pmatrix}, \tag{3.62}$$

which is known as the Tellegene [55] type magnet-electric coupling. This breaks the bosonic TRS since in this case,

$$T_B \begin{pmatrix} \hat{\varepsilon} & \hat{\xi} \\ \hat{\xi}^\dagger & \hat{\mu} \end{pmatrix} T_B = \begin{pmatrix} \hat{\varepsilon} & -\hat{\xi} \\ -\hat{\xi}^\dagger & \hat{\mu} \end{pmatrix} \tag{3.63}$$

On the other hand, as seen below, this form gives an invariance under a fermionic type time reversal operation, which is given by $T_F \left(\vec{E}, \vec{H}\right)^t = \left(\vec{H}^*, -\vec{E}^*\right)^t$, with a strict condition, the equivalence $\hat{\varepsilon} = \hat{\mu}$. Under the T_F, the right hand side of the eigenequation transforms as

$$T_F^{-1}(-T_F) \begin{pmatrix} \hat{\varepsilon} & \hat{\xi} \\ \hat{\xi}^\dagger & \hat{\mu} \end{pmatrix} T_F = \begin{pmatrix} \hat{\mu}^* & \hat{\xi} \\ \hat{\xi}^\dagger & \hat{\varepsilon}^* \end{pmatrix}. \tag{3.64}$$

Then if the equivalence $\hat{\varepsilon} = \hat{\mu}$ is assured, it is invariant under T_F. The left hand side is transformed as

$$T_F^{-1}\begin{pmatrix} 0 & -\mathrm{i}\nabla\times \\ \mathrm{i}\nabla\times & 0 \end{pmatrix} T_F = \begin{pmatrix} 0 & \mathrm{i}\nabla\times \\ -\mathrm{i}\nabla\times & 0 \end{pmatrix}. \tag{3.65}$$

The ± sign difference in the left hand side means that the sector of the solution is moved to the opposite sector. [4]

To return to the original sector, we have to take complex conjugate of both hands. Then, the transformation for the right hand side should be taken as

$$T_F^{-1}\begin{pmatrix} \hat{\varepsilon} & \hat{\xi} \\ \hat{\xi}^\dagger & \hat{\mu} \end{pmatrix} T_F = \begin{pmatrix} \hat{\mu}^* & \hat{\xi}^* \\ \left(\hat{\xi}^\dagger\right)^* & \hat{\varepsilon}^* \end{pmatrix}, \tag{3.66}$$

as a consequence, for the fermionic time reversal here, a system with complex tensor $\hat{\varepsilon} = \hat{\mu}$ can have TRS. However, the invariance for the T_F is a more strict condition, that is, the equivalence $\hat{\varepsilon} = \hat{\mu}$ is never found in natural materials.

The above photonic topological insulator with fermionic TRS was proposed and studied by Ochiai [56]. A material having the Tellegene type magneto electric coupling is found in the multiferroic materials [57]. Also, a combination of piezo-magnetic and piezo-electric material is known to show the magnet-electric coupling [58, 59]. Although, for the former, the EM tensor is determined as a material property, it is tenable for the later by changing the stacking ratio such as

$$\varepsilon_{\text{eff}} = x\epsilon_{\text{PE}} + (1-x)\varepsilon_{PM}\mu = x\mu_{\text{PE}} + (1-x)\mu_{\text{PM}}. \tag{3.67}$$

Therefore, for achieving the equivalence $\hat{\epsilon} = \hat{\mu}$, the later is preferable. In addition, the magnet-electric coupling occurs in resonance. Then, the EM tensor is strongly frequency dependent. Since the resonance frequency is a material property, the scale of the structure should be tuned to meet the topological band gap to the resonance frequency. Since the edge mode considered here relies strongly on the existence of fermionic pseudo TRS, the cladding material of the edge also have to have the pseudo TRS. As an example, the EM tensor of the cladding material with fermionic TRS is given in the simple form,

$$\hat{\epsilon} = \hat{\mu} = \mathrm{diag}\left\{1, 1, -1\right\}. \tag{3.68}$$

As a result, the band gap characterized by non-trivial Z_2 index has the topological edge modes at interface with the unusual cladding with fermionic TRS, whereas it disappear for the cladding by perfect conductor.

Photonic topological insulator with crystal line symmetry

Also, without resorting to the magnetoptical coupling, an all dielectric photonic topological insulator has been shown to be achievable. An all dielectric 2D photonic topological insulator, the band structure of which is characterized by the crystal-line symmetry instead of usual TRS was first proposed by Hu and Wu [60]. They considered usual 2D photonic crystal consisting of honeycomb array of cylinders and toke each hexagon as a cluster. By shrinking or extending the cluster size, the structure forms a Kekule pattern, which does not break the C_6 symmetry of the honeycomb lattice. Inducing the Kekule pattern partially brakes the transnational symmetry and broadens the size of the unit cell three times. When the unit cell is enlarged three-times, the original Brillouin zone is folded to the size of one-third and K and K' points comes to the Γ point. The two dirac cones are protected by the transnational symmetry for the honeycomb lattice and Induction of the Kekule pattern opens a gap at Γ point. It is seen by examining the poyinting vector of the eigenfield that the field is isolated for the shrunken cluster, whereas it is itinerant for the extended cluster. As seen below, these two states can be topologically distinctive.

In the work by Wu and Hu, the 2D TM-mode band structure is considered. The Γ point has the entire crystal symmetry of C_{6v}. The irreducible representation of the two dirac cones at K and K' points becomes two 2D representations of E_1 and E_2 for lower and upper two bands respectively. The expression of the E_1 for the

[4] The EM field should indeed be represented as a real valued field with its complex conjugate field. The complex conjugate is the solution of the complex conjugate of the both hands of the eigenequation.

lower bands is x, y and that of the E_2 or the higher bands is $x^2 - y^2, xy$. Then the eigenfields for the lower two bands correspond to p_x and p_y orbitals in the condensed matter convention and the upper two bands correspond to $d_{x^2-y^2}$ and d_{xy}. The representation of the C_6 for the $p-$orbitals is given by

$$D_p(C_6)\begin{pmatrix} p_x \\ p_y \end{pmatrix} = \begin{pmatrix} \frac{1}{2} & -\frac{\sqrt{3}}{2} \\ \frac{\sqrt{3}}{2} & \frac{1}{2}. \end{pmatrix} \tag{3.69}$$

The combination $U = \left(D_p(C_6) + D_P(C_6^2)\right) / \sqrt{3} = -\mathrm{i}\sigma_y$ gives the $\pi/2$ rotation and gives $U^2 = -1$. On the other hand, the representation of the C_6 for the $d-$orbitals is given by

$$D_d(C_6)\begin{pmatrix} d_{x^2-y^2} \\ d_{xy} \end{pmatrix} = \begin{pmatrix} -\frac{1}{2} & -\frac{\sqrt{3}}{2} \\ \frac{\sqrt{3}}{2} & -\frac{1}{2} \end{pmatrix}\begin{pmatrix} d_{x^2-y^2} \\ d_{xy} \end{pmatrix}. \tag{3.70}$$

Then the combination $U = \left(D_d(C_6) - D_d(C_6^2)\right) / \sqrt{3}$ is associated with $\pi/4$ rotation and again give $U^2 = -1$. Since the system is TRS invariant, the system has the complex conjugate K as a symmetric transformation. Further, by composing a pseudo time reversal operator in combination with U as $T = UK$, it gives $T^2 = -1$. Like this, the crystal line symmetry gives alternative to the spin degree of freedom to take a parallel argument to spin-full topological insulator [61]. The time reversal operator T is diagonalized for each p and d by the pseudo spin polarized states

$$p_\pm = \left(p_x \pm \mathrm{i}p_y\right) / \sqrt{2}, \quad d_\pm = \left(d_{x^2-y^2} \pm \mathrm{i}d_{xy}\right). \tag{3.71}$$

Since the system is invariant under T, the polarization does not change in the system. As known from examination of the profile of the eigenfileds, the extended Kekule pattern causes the band-inversion at Γ point, whereas the shrunken pattern does not. Therefore the band structure for the extended Kekule pattern is topologically non-trivial with the Z_2 classification under the pseudo TRS $T = KU$. As a consequence, the dispersion of the helical edge modes for the optical pseudo spin, namely bidirectional edge modes for opposite optical pseudo spins, appears in the gap in the case of the extended Kekule pattern.

The photonic helical edge states discussed here is different from that of electronic topological insulator in the sense that the notion of the Fermi level does not exist here. That is, unless a light is induced in the system, it remains to be empty or conversely, we can extract the preferable direction for the edge mode propagation by polarizing the pseudo spin of the light at will. Unlike the chiral edge mode in the TRS broken system, the back scattering of the edge mode is not reduced unless the optical pseudo spin is protected and it is known to be technically difficult to fully control the optical polarization in the structure. Note that these are also the case in the photonic topological insulator with magnet-optical couplings.

3.4 Topological photonics in other setups

Evanescently coupled waveguides

In the case that the spatial contrast of refractive indices is not so large and the wave vector k_z for the propagation direction is sufficiently large, we can apply the scalar field approximation, or so-called LP mode. [62]

$$\boldsymbol{E}(\boldsymbol{r}) = E_1(\boldsymbol{r})\,\boldsymbol{e}_1. \tag{3.72}$$

We obtain the Helmholtz equation for a scalar field

$$\nabla^2\psi(x, y, z) + k_0^2 n_2 \psi(x, y, z) = 0. \tag{3.73}$$

The scalar field varies rapidly in the z direction mostly as $\mathrm{e}^{\beta z}$ with β being $\beta = n_{\mathrm{eff}}k_0$. The, it is useful to adopt an envelope

$$\psi(x, y, z) = \phi(x, y, z)\,\mathrm{e}^{\mathrm{i}\beta z}. \tag{3.74}$$

By using this envelope, the Eq. (3.73) becomes

$$2\mathrm{i}\beta\frac{\partial\phi}{\partial z} - \frac{\partial^2}{\partial^2 z}\phi = \left(\nabla_\perp^2 + k_0^2\left(n^2 - n_{\mathrm{eff}}^2\right)\right)\phi. \tag{3.75}$$

Here the second term of the left hand side can be neglected for paraxial propagation modes $\partial^2/\partial^2 z\ \phi = 0$, which is called the Fresnel approximation. The paraxial equation has the same form as the two-dimensional Shrödinger equation by regarding the axis z as the time axis.

Below, we consider on the numerical method. In a short interval of time $\triangle z$, if the system are sufficiently smooth in the z direction, we can assume for the scalar field the form of

$$\phi(x, y, z) = A(x, y) \exp(\gamma z). \tag{3.76}$$

By substituting this equation into the governing equation Eq. (3.75) with the Fresnel approximation, we obtain

$$\begin{aligned} 2\mathrm{i}\beta\gamma A(x, y) &= \nabla_\perp^2 A(x, y) + k_0^2 \left(n^2 - n_{\mathrm{eff}}^2\right) A(x, y) \\ A\gamma &= -\frac{\mathrm{i}}{2\beta}\left\{\nabla_\perp^2 + k_0^2 \left(n^2 - n_{\mathrm{eff}}^2\right)\right\} A. \end{aligned} \tag{3.77}$$

Thus denoting $\chi = \frac{1}{2\beta} k_0^2 \left(n^2 - n_{\mathrm{eff}}^2\right)$, for a sufficiently short interval, we can write

$$\phi(x, y, z + \triangle z) = \exp\left(-\mathrm{i}\frac{\mathrm{i}}{2\beta}\left(\nabla_\perp^2 + k_0^2 \left(n^2 - n_{\mathrm{eff}}^2\right)\right)\triangle z\right)\phi(x, y, z). \tag{3.78}$$

For sufficiently small $\triangle z$, we can decompose the exponent and represent the evolution as

$$\phi(x, y, z + \triangle z) = \exp\left(-\mathrm{i}\frac{\mathrm{i}}{2\beta}\triangle z\right)\exp\left(-\mathrm{i}\frac{\mathrm{i}}{2\beta} k_0^2 \left(n^2 - n_{\mathrm{eff}}^2\right)\triangle z\right)\phi(x, y, z). \tag{3.79}$$

For the one-order higher precision, we can denote

$$\phi(x, y, z + \triangle z) = \exp\left(-\mathrm{i}\frac{\nabla_\perp^2}{4\beta}\triangle z\right)\exp\left(-\mathrm{i}\frac{1}{2\beta} k_0^2 \left(n^2 - n_{\mathrm{eff}}^2\right)\triangle z\right)\exp\left(-\mathrm{i}\frac{\nabla_\perp^2}{4\beta}\triangle z\right)\phi(x, y, z). \tag{3.80}$$

For this form, it is numerically efficient to use the basis being diagonal to the adjacent exponential. For $\nabla_\perp^2$, the plane wave is diagonal, however it is the real space basis for the middle exponential. That is, we have to transform between the real space and wave space basis sets, using a numerically sophisticated method such as Fast Fourier Transform(FFT).

Topological photonics in the system of coupled ring resonators and network model

In this section, we review the studies in the system of coupled ring resonators, which is really suited to simulate the *Harper-Hofstader Hamiltonian* as demonstrated by Hafezi et al. [63]. The system is comprised of array of closed wave guides of rings, which is in resonance at wavelength $\lambda = nL$ with n being refraction constant and L circumference. A resonance mode in a closed waveguide tunnels into an adjacent waveguide at a contact point, which is simply represented by a scattering matrix. By interposing a link resonator between two equivalent waveguides, resonance modes in the entire array is unidirectional and as we will see below, it enables us to implement a synthetic gauge field.

Transfer matrix formalism and coupled mode theory

First of all, we discuss the equivalence between the transfer matrix formalism and coupled mode theory for describing the physics of coupled resonators, following the discussion by Hafezi, et al. [64]. Let us begin with the simplest example, namely 'add-drop filter', which is the system of two modes coupled by a resonator (Fig. 3.3). Firstly in the coupled mode theory, it reads

$$\frac{\mathrm{d}E}{\mathrm{d}t} = (-\kappa_{\mathrm{in}} - 2\kappa_{\mathrm{ex}})E - \sqrt{2\kappa_{\mathrm{ex}}}E_{\mathrm{in}}\mathrm{e}^{-\mathrm{i}\omega t}, \tag{3.81}$$

where κ_{ex} is the coupling rate to the attached waveguide, κ_{in} is decay rate into other neglected modes and ω is the detuning of the input field to resonance frequency. The output amplitude is related to the amplitude within

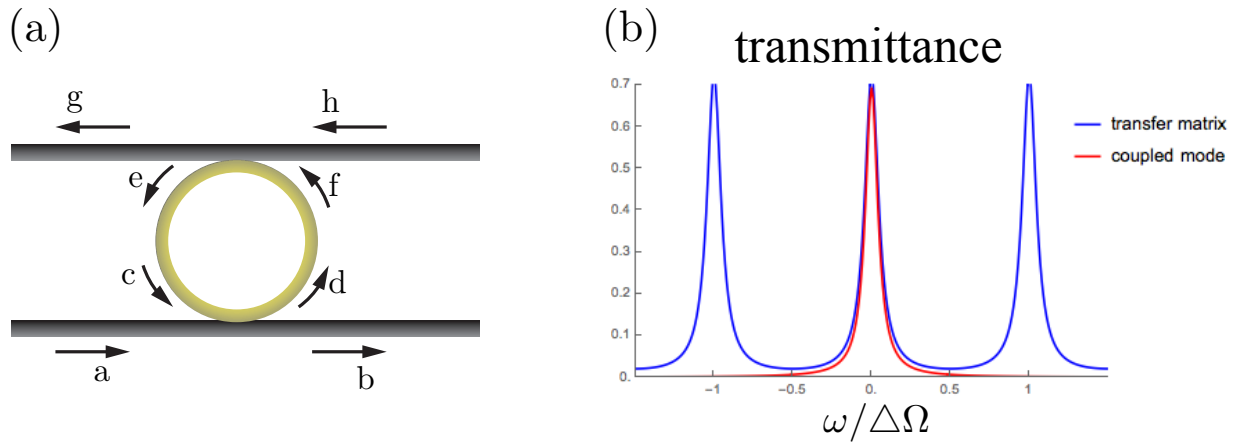

Figure 3.3: (a) Configuration of add-drop filter. (b) Comparison of two results for $\varepsilon - 0.5$ and $\alpha' L = 0.05$.

the resonator by $E_{\text{out}} = \sqrt{2\kappa_{\text{ex}}}E$. For each part, only monochromatic mode is assumed. Solving the differential equation, we obtain

$$E = \frac{\sqrt{2\kappa_{\text{ex}}}E_{\text{in}}}{\mathrm{i}\omega - \kappa_{\text{in}} - 2\kappa_{\text{ex}}}, \tag{3.82}$$

and transmission rate is

$$t = \frac{E_{\text{out}}}{E_{\text{in}}} = \frac{2\kappa_{\text{ex}}}{\mathrm{i}\omega - \kappa_{\text{in}} - 2\kappa_{\text{ex}}}. \tag{3.83}$$

Next, we reconsider the problem from transfer matrix formalism. In this formalism, we take inputs from all channels and outputs to all channels as fundamental degrees of freedom and relates those by a unitary $S-$ matrix, matrix element of which is given by a quantity such as transmission, reflection or scattering rate to different channels. In the case of Fig. 3.3, two outputs amplitudes and two input amplitude are related by the $S-$ matrix at the contact point as

$$\begin{pmatrix} b \\ d \end{pmatrix} = S_{\text{couple}} \begin{pmatrix} a \\ c \end{pmatrix} \quad S_{\text{couple}} = \begin{pmatrix} t & r \\ r & t \end{pmatrix}, \tag{3.84}$$

where t and r is transmission and reflection rate respectively. The relation $s_{11} = s_{22}$ is understood from symmetry and $s_{12} = s_{21}$ is from reciprocity. From unitarity, these coefficients satisfy

$$|t|^2 + |r|^2 = 1 \tag{3.85}$$

$$t^* s + s^* t = 0. \tag{3.86}$$

We know that $(a, b, c, d) = (1, r, 0, t)$ and $(a, b, c, d) = (0, t, 1, r)$ are solution. Then we obtain

$$\begin{pmatrix} d \\ c \end{pmatrix} = M \begin{pmatrix} a \\ b \end{pmatrix}, \quad M_{\text{couple}} = \begin{pmatrix} 1/t(t^2 - r^2) & r/t \\ -r/t & 1/t \end{pmatrix}. \tag{3.87}$$

Within the resonator, amplitudes between two contact points are related as

$$\begin{pmatrix} f \\ e \end{pmatrix} = M_{\text{prop}} \begin{pmatrix} d \\ c \end{pmatrix}, \quad M_{\text{prop}} = \begin{pmatrix} \mathrm{e}^{\mathrm{i}\beta L/2 - \alpha' L/2} & 0 \\ 0 & \mathrm{e}^{-\mathrm{i}\beta L/2 - \alpha' L/2} \end{pmatrix}, \tag{3.88}$$

where $\beta = \frac{2\pi n}{\lambda}$ with n being refraction constant and λ the vacuum wave length of the propagating mode, and α' is an absorption constant. The amplitudes of two external modes are finally related by

$$\begin{pmatrix} g \\ h \end{pmatrix} = M_{\text{couple}} M_{\text{prop}} M_{\text{couple}} \begin{pmatrix} a \\ b \end{pmatrix}, \tag{3.89}$$

and g is regarded as 0 as we did previously. From the transfer matrix formalism, the situation similar to the couple mode theory is the limit $r \to \sqrt{1-\varepsilon^2}, t \to \mathrm{i}\varepsilon$ with $\varepsilon << 1$. We are only interested in the situation $\beta L = 2\pi m$, and we assume the quality of the waveguide is good enough $\alpha' L << 1$. The input is only present at a in Fig. 3.3, and we can set $a = 1, h = 0$. Keeping the terms up to the first order in $\epsilon^2, \beta L, \alpha' L$, we obtain the transmission rate

$$g = \frac{M_{11}M_{22} - M_{12}M_{21}}{M_{22}} = \frac{\varepsilon^2}{\mathrm{i}\beta L - \alpha' L - \varepsilon^2}. \tag{3.90}$$

Now, if we substitute the coefficients by

$$\varepsilon^2 \to \frac{4\pi\kappa_{\mathrm{ex}}}{\triangle\omega}, \quad \alpha' L \to \frac{2\pi\kappa_{\mathrm{in}}}{\triangle\omega}, \quad \beta L \to 2\pi\frac{\omega}{\triangle\omega}, \tag{3.91}$$

the same result is obtained.

Synthetic gauge field

Next, we compare the system of two ring resonators coupled thorough a middle off-resonant ring with the coupled mode theory of two resonators with tunneling phase. Again, let us begin with describing the transmittance and the reluctance in the coupled mode theory. We consider a tunneling with phase between resonators, and it reads

$$H_{r-r} = -Ja_2^\dagger a_1 \mathrm{e}^{-\mathrm{i}\phi} - Ja_1^\dagger a_2 \mathrm{e}^{-\mathrm{i}\phi}. \tag{3.92}$$

Other parts of the hamiltonian, such as contact between the port and resonator, are same as the previous problem. Then, the coupled mode equation reads

$$\frac{\mathrm{d}}{\mathrm{d}t}\begin{pmatrix} a_1 \\ a_2 \end{pmatrix} = \begin{pmatrix} -\kappa_{\mathrm{in}} - \kappa_{\mathrm{ex}} & \mathrm{i}J\mathrm{e}^{\mathrm{i}\phi} \\ \mathrm{i}J\mathrm{e}^{-\mathrm{i}\phi} & -\kappa_{\mathrm{in}} - \kappa_{\mathrm{ex}} \end{pmatrix}\begin{pmatrix} a_1 \\ a_2 \end{pmatrix} - \sqrt{2\kappa_{\mathrm{ex}}}\begin{pmatrix} E_{\mathrm{in}} \\ 0 \end{pmatrix}. \tag{3.93}$$

The output fields of resonators are given as $a_2^{\mathrm{out}} = \sqrt{2\kappa_{\mathrm{ex}}}a_2$, $a_1^{\mathrm{out}} = 1 + \sqrt{2\kappa_{\mathrm{ex}}}a_1$ respectively. Solving the equation, we obtain

$$r = \frac{\sqrt{2\kappa_{\mathrm{ex}}}a_2}{E_{\mathrm{in}}} = -\frac{2\mathrm{i}\mathrm{e}^{-\mathrm{i}\phi}J\kappa_{\mathrm{ex}}}{J^2 + (\mathrm{i}\omega - \kappa_{\mathrm{in}} - \kappa_{\mathrm{ex}})^2} \tag{3.94}$$

$$t = 1 + \frac{\sqrt{2\kappa_{\mathrm{ex}}}a_1}{E_{\mathrm{in}}} = 1 + \frac{2\kappa_{\mathrm{ex}}\left(\mathrm{i}\omega - \kappa_{\mathrm{ex}} - \kappa_{\mathrm{in}}\right)}{J^2 + (\mathrm{i}\omega - \kappa_{\mathrm{ex}} - \kappa_{\mathrm{in}})^2}. \tag{3.95}$$

In next, we consider the same problem from the transfer matrix formalism. However, if we align two rings with directional coupling, it circulates in the clockwise direction at one resonator, whereas it does in the counterclockwise direction at another resonator. To unify the circulation direction, we interpose a off-resonant ring between two resonators. Now we have to prepare two kinds of $S-$matrix for *resonator-port* denoted as M_1 and *resonator-middle resonator* denoted as M_2, and these are given by

$$M_1 = \frac{1}{t_1}\begin{pmatrix} -r_1^2 + t_1^2 & r_1 \\ -r_1 & 1 \end{pmatrix} \tag{3.96}$$

$$M_2 = \frac{1}{t_2}\begin{pmatrix} -r_2^2 + t_2^2 & r_2 \\ -r_2 & 1 \end{pmatrix} \tag{3.97}$$

Amplitude at contact points between port and ring are given as previous

$$\begin{pmatrix} d \\ c \end{pmatrix} = M_1\begin{pmatrix} a \\ b \end{pmatrix}, \quad \begin{pmatrix} l \\ k \end{pmatrix} = M_1\begin{pmatrix} i \\ j \end{pmatrix}. \tag{3.98}$$

We assume that the length of the middle resonator is changed by η so that it is off-resonant there. Further, we consider displacing it to make difference in the length between lower half and upper half by x. Then the

$S-matrix$ for the middle part is given by

$$\begin{pmatrix} h \\ g \end{pmatrix} = M_2 M_{p2} M_2 \begin{pmatrix} e \\ f \end{pmatrix} \tag{3.99}$$

$$M_{p2} = \begin{pmatrix} \mathrm{e}^{\mathrm{i}\beta L/2+\mathrm{i}\beta\eta/2-2\mathrm{i}\beta x-\alpha' L/2} & 0 \\ 0 & \mathrm{e}^{-\mathrm{i}\beta L/2-\mathrm{i}\beta\eta/2-2\mathrm{i}\beta x+\alpha' L/2} \end{pmatrix}. \tag{3.100}$$

Keeping terms up to the second order in $\varepsilon_i^2, \beta L, \alpha' L$ for each of numerator and denominator, the transmittance is given by

$$r = \frac{\mathrm{Det}M}{M_{22}} = \frac{2\mathrm{e}^{-\mathrm{i}\beta x}\varepsilon_1^2\varepsilon_2^2}{2\left(2\alpha' L - 2\mathrm{i}\beta L + \varepsilon_1^2\right)\varepsilon_2^2\cos(\beta\eta) - \mathrm{i}\left(\left(2\alpha L - 2\mathrm{i}\beta L + \varepsilon_1^2\right)^2 + \varepsilon_2^4\right)\sin(\beta L)}. \tag{3.101}$$

By replacing the quantities,

$$\epsilon_1^2 \to \frac{4\pi\kappa_{\mathrm{ex}}}{\triangle\omega}, \epsilon_2^2 \to \frac{4\pi J}{\triangle\omega}, \alpha' L \to \frac{2\pi\kappa_{\mathrm{in}}}{\triangle\omega}, \beta L \to 2\pi\frac{\omega}{\triangle\omega}, \beta x \to \phi, \tag{3.102}$$

it reads

$$r = \frac{2\mathrm{e}^{-\mathrm{i}\phi} J\kappa_{\mathrm{ex}}}{2J\left(\kappa_{\mathrm{ex}} + \kappa_{\mathrm{in}} - \mathrm{i}\omega\right)\cos(\beta\eta) - \mathrm{i}\left(J^2 + \left(\kappa_{\mathrm{ex}} + \kappa_{\mathrm{in}} - \mathrm{i}\omega\right)^2\right)\sin(\beta\eta)}. \tag{3.103}$$

In the case of $\beta\eta = 3/2\pi$, it falls into the same as the Eq.(3.94), and in the case of $\beta\eta = \pi/2$ the sign of tunneling coefficient is flipped. Here, the displacement x effects as the tunneling phase. Then, if we arrange the resonators to form a two dimensional square lattice and increasing the displacement of the middle ring, it realize the Harper-Hofstader model with the *synthetic gauge*. However, note that since the tunneling phase $\mathrm{e}^{\mathrm{i}\beta x'}$ depends on the *beta* it varies with the eigenfrequency ω for the same displacement x'. Although there is no effect breaking TRS, if the propagation direction is preserved between the clockwise and counter-clockwise directions, TRS is broken for each sector as the spin polarized QHSE with propagating direction being the spin degree of freedom.

Frequency band structure in the coupled resonator array

Since we have seen that the coupled resonator system is mapped to the corresponding tight-binding model, it is sufficient to study the tight-binding model and experimental results can be explained. On the other hand, there exists studies [65–67] that analyze the network model directly using the transfer matrix formalism and the Bloch theorem. A sequence of products of the S matrices, which is unitary transformation between outputs and inputs, relates amplitudes at distant points and the Bloch theorem returns its amplitude to the original one.

Chapter 4

Numerical analysys of electromagnetic fields in photonic crystals

In this chapter, we describe the method for numerical analysis of EM fields. Since dielectric materials do not confine EM fields but only scatter them, the tight-binding approximation is not appropriate for the analysis. We have to deals with continuous fields directly. The EM field in a dielectric photonic crystal formed by sequential scatterings from dielectric scatters and thus it is suitable to use plane waves as expansion basis [68, 69]. An advantage in the plane waves is that a transverse field is expanded by only two component of polarization. On the other hand, real space basis methods such as the finite element method [70–74] are often used for the numerical analysis of the EM field. The real space basis methods are suitable for the analysis of finite size structure that lacking the spatial periodicity and also real time evolution is usually done in a real space basis.

Further, the use of the real space basis is advantageous to the topological argument of the band structure, since it respects the periodicity of the Brillouin zone whereas the plane wave expansion does not for a finite number truncation. For the purpose of formulating the procedure to numerically evaluate topological invariants of the photonic band structures, we develop the method using a gaussian basis set to solve the Maxwell equations for EM waves in photonic crystals. The matrix element between gaussian functions for the vacuum or some simple analytic potentials is given analytically by working at simple algebraic manipulations. This is a great merit over other spatially localized basis. In addition, since the gaussian function is smooth, it is advantageous in dealing with some curved structures. For example in the real space grid, such a curved surfaces have to be made rectangular shaped. In the case of the finite element method, it is not good at dealing with spatial variation within a discretized element, and then it is required to generate a mesh that conforms the shape of the interface for each structure.

In this chapter, we first describe the gaussian basis expansion of continuous fields. Then, we focus on solving the Maxwell equation for EM waves in photonic crystals. Then, basis elements with gaussian type localization are introduced for the expansion of EM fields. Finally, we exhibit some typical result to test the validity of the method.

4.1 The gaussian basis expansion

To expand a continuous field, we put a set of gaussian functions

$$g_i(\boldsymbol{r}) = p(\boldsymbol{r} - \boldsymbol{R}_i)\, \mathrm{e}^{-\alpha_i(\boldsymbol{r}-\boldsymbol{R}_i)^2} \tag{4.1}$$

on points arranged uniformly in space(Fig. 4.1). Here the $\vec{R}_i$ represents the localized center, α_i specifies the localization length, which can be set differently for each basis, and the $p(\vec{r}-\vec{R}_i)$ represents a certain polynomial of $(x - x_i, y - y_i, z - z_i)$. Without notice, we set the α to be uniform over the entire gaussian bases. In a spatially periodic system, the basis element can be taken as

$$g_i(\boldsymbol{r}) = \sum_n p(\boldsymbol{r} - \boldsymbol{R}_{ni})\mathrm{e}^{-\alpha_i(\boldsymbol{r}-\boldsymbol{R}_{ni})^2}\mathrm{e}^{\mathrm{i}\boldsymbol{k}\cdot\boldsymbol{R}_{n0}}, \tag{4.2}$$

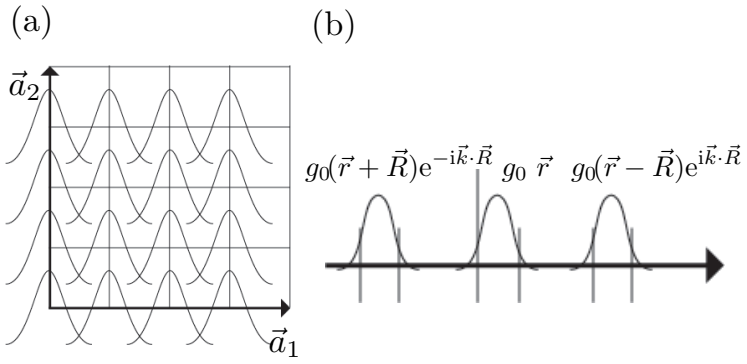

Figure 4.1: Reprinted from [75] with the permission of American Physical Society. (a) Each basis function with the gaussian localization factor is put on the grid point that divide the computational space uniformly. (b) A bloch states is composed of the set of gaussian functions with the same coefficient for corresponding locations within the unit cells and the Bloch wave factor $e^{i\vec{k}\cdot\vec{R}_n}$, where the $\vec{R}_n$ denotes a lattice(between unit cells) translation vector.

with $\vec{k}$ being the Bloch vector. We attempt to approximate a continuous field by the gaussian basis set

$$f(\boldsymbol{r}) = \sum_i c_i g_i(\boldsymbol{r})\,. \tag{4.3}$$

By densely locating the gaussian basis set, an arbitrary continuous field can be restored by the gaussian basis set in the limit. However, the more rapidly the continuous field vary in space, the more densely the gaussian bases have to be located.

We assume an eigenvalue problem

$$\Theta f(\vec{r}) = \lambda f(\vec{r}). \tag{4.4}$$

If we prepare a sufficient number of gaussian bases, we can expect that the action of the operator in the left hand side is closed withing the basis set, namely for an arbitrary element

$$\Theta g_i(\boldsymbol{r}) \approx \sum_j a_j g_j(\boldsymbol{r}). \tag{4.5}$$

The expansion coefficients are obtained as follows. First we take the inner product $\int \mathrm{d}^3 r\; g_i(\boldsymbol{r})\cdot$ with the Eq. (4.3)

$$\tilde{c}_i = \int \mathrm{d}^3 r\; g_i(\boldsymbol{r})\, f(\boldsymbol{r}) = \int \mathrm{d}^3 r\; g_i(\boldsymbol{r}) \sum_j c_j g_j(\boldsymbol{r}) = \sum_j O_{ij} c_j. \tag{4.6}$$

Since for the gaussian basis set, the overlap between them is nonzero $\langle g_i | g_j \rangle \neq 0$, it includes redundant contributions. The coefficients $\{c_i\}$ are given by further solving the linear equation

$$O \begin{pmatrix} c_1 \\ c_2 \\ \vdots \\ c_N \end{pmatrix} = \begin{pmatrix} \langle g_1|g_1\rangle & \langle g_1|g_2\rangle & \cdots & \langle g_1|g_N\rangle \\ \langle g_2|g_1\rangle & \langle g_2|g_2\rangle & \cdots & \langle g_2|g_N\rangle \\ \vdots & \vdots & \ddots & \vdots \\ \langle g_N|g_1\rangle & \langle g_N|g_2\rangle & \cdots & \langle g_N|g_N\rangle \end{pmatrix} \begin{pmatrix} c_1 \\ c_2 \\ \vdots \\ c_N \end{pmatrix} = \begin{pmatrix} \tilde{c}_1 \\ \tilde{c}_2 \\ \vdots \\ \tilde{c}_N \end{pmatrix} \quad . \tag{4.7}$$

Then the eigenvalue problem(Eq. 4.4) is expressed within the gaussian basis set as

$$\sum_j \Theta_{ij} c_j = \lambda \sum_j O_{ij} c_j. \tag{4.8}$$

With the method devised by Fukui, Hatsugai and Suzuki [76], the Chern number of a gapped spectrum is computed from the eigenvectors of the Eq. 4.8, which is described in the appendix. The generalized eigenvalue problem4.8 is solved with a fixed number of steps in the dense matrix computation or with an iterative algorithm in the sparse matrix computation [77].

4.2 Matrix expansion of the Maxwell equations with the gaussian basis set

In this section, we examine appropriate settings for the Gaussian basis sets to obtain correct results for empty lattice in 2D and 3D cases. Furthermore based on the settings in the empty lattice, we test some results of typical photonic crystals as examples.

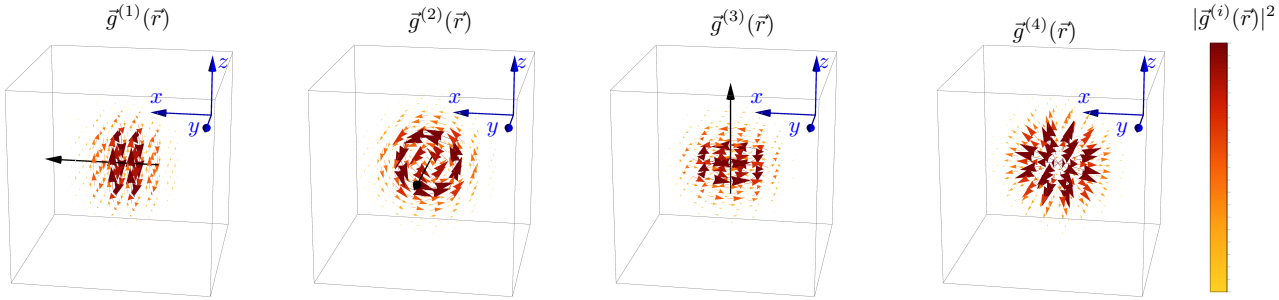

Figure 4.2: Plot of the modified vector gaussian basis elements for each polarization. The $\vec{g}^{(1)}$ $\vec{g}^{(3)}$ are divergence-free elements. The $\vec{g}^{(4)}$ is the longitudinal component. The color of vectors represents the intensity of the vector.

Usually, the spatial variation of EM tensors in photonic crystal is realized by setting materials with different optical constants. Then, they are constant within the same material. For the numerical integration to obtaine the matrix element, it is convenient to separate the optical constant within the material such as $\hat{\varepsilon} = \hat{I} + (\hat{\varepsilon} - \hat{I})$. Since we are using the gaussian functions, the integral for the first term is analytycally given and numerical integration for the second term is done only within the material.

4.2.1 2D problem

Because of TE-TM decomposition in the 2D case, we can use the scalar decomposition (4.1) for numerical diagonalization. For the scalar eigenequation, we use a simple gaussian basis function

$$g_{ik}(\boldsymbol{r}) = \frac{1}{\sqrt{N}} \sum_m \mathrm{e}^{\mathrm{i}\boldsymbol{k}\cdot\boldsymbol{R}_m} \mathrm{e}^{-r_{im}^2/\alpha^2}. \tag{4.9}$$

There are a little differences in the procedure for $\vec{E}$ and $\vec{H}$polarizations. For TE mode, the $\hat{\varepsilon}(\vec{r})$ appearing in the left hand side of the Eq.(3.30) varies in space, whereas the $\hat{\mu}$ in the right hand side is constant($\mu = 1$). The gaussian expansion of the left hand side gives

$$\begin{aligned}\langle g_{ik}|\hat{L}_H|g_{jk}\rangle = \langle g_{ik}|\nabla\times\hat{\epsilon}^{-1}\nabla\times|g_{jk}\rangle = \langle\nabla\times g_{ik}|\hat{\epsilon}^{-1}|\nabla\times g_{jk}\rangle \\ = \sum_n \mathrm{e}^{-\mathrm{i}\boldsymbol{k}\cdot\boldsymbol{R}_n} \int \mathrm{d}^2 r\ (-2\alpha y_{in}, 2\alpha x_{in})\cdot\hat{\varepsilon}^{-1}(\boldsymbol{r}) \begin{pmatrix} -2\alpha y_j \\ 2\alpha x_j \end{pmatrix}\end{aligned} \tag{4.10}$$

Each basis function(Eq. 4.9) is cylindrically symmetric and they overlap each other between two points at a certain distance. These basis elements are configured on the grid points that divides the unit cell regularly (Fig.4.1). Later, we will show that the simple configuration of the basis elements gives sufficient accuracy, and there arises no requirement for further effort on the distribution of the grids, which is important in the finite element methods.

For this basis set, the integral of the overlap $R_{H,ij}(\boldsymbol{k})$ for the constant term (when $\hat{\mu}_c = \hat{1}$) is obtained as

$$R_{H,ij}^{\mathrm{empty}}(\boldsymbol{k}) = \sum_m \frac{\pi\alpha^2}{2} \mathrm{e}^{-\mathrm{i}\boldsymbol{k}\cdot\boldsymbol{R}_m} \mathrm{e}^{-\frac{r_m'^2}{2\alpha^2}}, \tag{4.11}$$

where $\boldsymbol{r}_m' = \boldsymbol{r}_i + \boldsymbol{R}_m - \boldsymbol{r}_j$. On the other hand, the matrix element $\hat{L}_{H,ij}(\boldsymbol{k})$ for the constant term (when $\hat{\varepsilon}_c^{-1} = \hat{1}$) is

$$\hat{L}_{H,ij}^{\mathrm{empty}}(\boldsymbol{k}) = \sum_m \frac{\pi\alpha^2}{2} \mathrm{e}^{-\mathrm{i}\boldsymbol{k}\cdot\boldsymbol{R}_m} \mathrm{e}^{-\frac{r_m'^2}{2\alpha^2}} \frac{1}{\alpha^2}\left(2 - \frac{r_m'^2}{\alpha^2}\right). \tag{4.12}$$

For the empty lattice, all the matrix elements of Eq. (3.30) are given by using Eqs. (4.11) and (4.12). When some different structures are introduced, the additional work to obtain matrix elements is the numerical integration within the structures.

4.2.2 3D problem

For a 3D problem, it is in general impossible to decompose the EM fields into TE or TM modes, and we have to handle all components of the vector. A naive thought suggests us to use the scalar Gaussian functions [Eq. (4.9)] for each component of the vector as

$$\psi_k(\boldsymbol{r}) = \sum_{\lambda=1}^{3} \boldsymbol{e}_\lambda \sum_i c_{ik}^\lambda g_{ik}(\boldsymbol{r})\,. \tag{4.13}$$

Here, $\boldsymbol{e}_\lambda$ represents unit vectors in three orthogonal directions. This naively introduced basis set, however, will end in failure due to the following reason. In first, note that the divergence of the Eq. (3.28) vanishes because of $\nabla\cdot(\nabla\times\boldsymbol{f}(\boldsymbol{r}))=0$ for any vector field $\boldsymbol{f}(\boldsymbol{r})$. Therefore, if the permeability is constant and isotropic, the solution of Eq. (3.28) satisfies the following constraint,

$$\nabla\cdot\boldsymbol{H}(\boldsymbol{r})=0. \tag{4.14}$$

On the other hand, the divergence of Eq. (4.13) is

$$\nabla\cdot\sum_{i,\lambda}\boldsymbol{e}_\lambda c_{ik}^\lambda g_{ik}(\boldsymbol{r}) = \sum_{i,\lambda}(-2\alpha x_\lambda)\,c_{ik}^\lambda g_{ik}(\boldsymbol{r})\,, \tag{4.15}$$

where the right-hand side remains except in the trivial case with $c_{ik}^\lambda = 0$ for all combinations of i and λ. Namely, expansion Eq. (4.13) does not satisfy constraint Eq.(4.14), and as a consequence, the spectrum of the eigenvalues includes unphysical spurious values. For each basis to satisfy constraint Eq. (4.14), we modify each basis by taking its rotation $\boldsymbol{g}_{ik}^\lambda(\boldsymbol{r}) = \nabla\times\boldsymbol{e}_\lambda g_{ik}(\boldsymbol{r}) = \sum_{\mu,\nu=1}^3 \varepsilon_{\mu\lambda\nu}\left(-2\alpha x_\mu\right) g_{ik}(\boldsymbol{r})\,\boldsymbol{e}_\nu$, with $\varepsilon_{\lambda\mu\nu}$ being an anti-symmetric symbol ($\varepsilon_{123}=1$). As a results, the modified bases for three components(Fig. 4.2) are

$$\boldsymbol{g}_i^{(1)}(\vec{r}) = \mathrm{e}^{-\alpha r_i^2/\alpha^2}\begin{pmatrix}0\\-z\\y\end{pmatrix},\qquad \boldsymbol{g}_i^{(2)}(\vec{r}) = \mathrm{e}^{-\alpha r_i^2/\alpha^2}\begin{pmatrix}z\\0\\-x\end{pmatrix},\qquad \boldsymbol{g}_i^{(3)}(\vec{r}) = \mathrm{e}^{-\alpha r_i^2/\alpha^2}\begin{pmatrix}-y\\x\\0\end{pmatrix}. \tag{4.16}$$

This is also obtained by choosing three independent bases of the lowest order from the polynomial in the Eq. (4.1) under the divergence-free condition. The modified basis element Eq. (4.2.2) is divergence-free, and satisfies the constraint [Eq. (4.14)]. We adopt these as basis elements and expand the solution using these basis elements as

$$\psi_k(\boldsymbol{r}) = \sum_{\lambda=1}^{3}\sum_i c_{ik}^\lambda \boldsymbol{g}_{ik}^\lambda(\boldsymbol{r})\,. \tag{4.17}$$

Again, we write down the integral values for this basis set in the following. The integrals for the constant term of the overlaps $R_{H,iz,jz}(\boldsymbol{k})$ and $R_{H,ix,jz}(\boldsymbol{k})$ are

$$R_{H,iz,jz}^{\text{empty}}(\boldsymbol{k}) = \sum_m \sqrt{\left(\frac{\pi\alpha^2}{2}\right)^3}\mathrm{e}^{-\mathrm{i}\boldsymbol{k}\cdot\boldsymbol{R}_m}\mathrm{e}^{-\frac{r_m'^{\,2}}{2\alpha^2}}\times\frac{1}{\alpha^2}\left\{2-\frac{1}{\alpha^2}\left(x_m'^{\,2}+y_m'^{\,2}\right)\right\} \tag{4.18}$$

$$R_{H,ix,jz}^{\text{empty}}(\boldsymbol{k}) = \sum_m \sqrt{\left(\frac{\pi\alpha^2}{2}\right)^3}\mathrm{e}^{-\mathrm{i}\boldsymbol{k}\cdot\boldsymbol{R}_m}\mathrm{e}^{-\frac{r_m'^{\,2}}{2\alpha^2}}\frac{1}{\alpha^4}x_m'z_m' \tag{4.19}$$

respectively. The integrals for the matrix elements $\hat{L}^{\text{empty}}_{H,iz,jz}(\boldsymbol{k})$ and $\hat{L}^{\text{empty}}_{H,ix,jz}(\boldsymbol{k})$ are

$$\hat{L}^{\text{empty}}_{H,iz,jz}(\boldsymbol{k}) = \sum_m \sqrt{\left(\frac{\pi\alpha^2}{2}\right)^3} \mathrm{e}^{-\mathrm{i}\boldsymbol{k}\cdot\boldsymbol{R}_m} \mathrm{e}^{-\frac{r'^2_m}{2\alpha^2}} \frac{1}{\alpha^4}\Big[\frac{1}{\alpha^4}\left(x'^2_m + y'^2_m\right)^2 - \frac{9}{\alpha^2}\left(x'^2_m + y'^2_m\right) + \frac{z'^2_m}{\alpha^2}\Big\{\frac{1}{\alpha^2}\left(x'^2_m + y'^2_m\right) - 2\Big\} + 10\Big] \tag{4.20}$$

$$Ł^{\text{empty}}_{H,ix,jz}(\boldsymbol{k}) = \sum_m \sqrt{\left(\frac{\pi\alpha^2}{2}\right)^3} \mathrm{e}^{-\mathrm{i}\boldsymbol{k}\cdot\boldsymbol{R}_m} \mathrm{e}^{-\frac{r'^2_m}{2\alpha^2}} \frac{x'_m z'_m}{\alpha^6}\left(7 - \frac{r'^2_m}{\alpha^2}\right) \tag{4.21}$$

respectively. Similarly, the integrals of the other components are obtained from the permutation $1 \to 2 \to 3$ and $x \to y \to z$. Also, the integrals are invariant against the simultaneous exchange of the position of the localization center and the direction of the polarization ($i\lambda' \leftrightarrow j\lambda$). Therefore, Eqs. (4.19)-(4.21) are sufficient for all matrix components of an isotropic bulk dielectric. Also for the modified basis elemnt for 3D problems, it is appropreate to to put grid points to divide the unit cell of the Bravais lattice with a regular spacing like Fig. 4.1.

However, if the both of $\hat{\varepsilon}$ and $\hat{\mu}$ vary, the basis functions of the Eq. 4.16 are insufficient since the vector field $\vec{H}(\vec{r})$ is no more divergence free. In this case, we have to add a longituidnal components. The fourth component for the longituidnal component is given in the gaussain form as

$$\boldsymbol{g}^{(4)}_i(\boldsymbol{r}) = \nabla \mathrm{e}^{-2\alpha r_i^2} = \begin{pmatrix} -2\alpha x_i \\ -2\alpha y_i \\ -2\alpha z_i \end{pmatrix} \mathrm{e}^{-\alpha r_i^2}. \tag{4.22}$$

After the numerical diagonalization, the spectrum of eigenvalue includes one third of zero values since the degree of freedom of the EM field is still two since $\vec{\nabla} \cdot \vec{D}, \vec{B} = 0$. In the case of the EM coupling(existence of non zero ξ in Eq. 3.24), the longitudinal component(Eq. 4.22) is also required since we have to take both of $\vec{E}$ and $\vec{H}$. The matrix element of the $\hat{L}$ for the longituidnal component vanishes since the rotation of the longituidinal basis vanishes and we have to only consider the overlap for the longitudinal basis. Those matrix elements are put off to the appendix.

For axial structures that is formed by stretching an isotropic structure in directions, an anistropic gaussian function stretched to the same directions is sutiable. We list matrix elements for a more general anisotropic gaussian functions and matrix elements between them in the appendix.

4.2.3 Test of the method

Empty lattice

For empty lattice, all matrix elements are analytycally obtained. Although a plane wave diagonalize the eigenequation in the empty lattice, it is not trivial for spatially localized basis set. The test in the empty lattice is meaningfull to optimize the basis function in longer wavelength.

2D bases

Let us begin with the 2D empty lattice, in which the scalar gaussian basis is used. In Fig. 4.3, the results of eigenvalues obtained by diagonalization with several gaussian parameteres ($\alpha = 1, \alpha = 0.63$)are compared with the solution $\omega = |\vec{k}|$ in the empty triangular lattices. The correctness of the result in longer wavelength depends on the amount of the overlap between gaussian bases. To reproduce slowly varying(longer wavelengths) fields, the amount of the overlap should be taken sufficiently large. The FWHM of the gaussian basis function is $1.7d$ for $\alpha = d$ and FWHM is d for $\alpha = 0.63d$, with d being the interspacing between adjacent gaussain bases. The requirement for the overlap is minimum in the triangular lattice since the lattice structure has the highest filling ratio. Even if an overlap amount is satisfactory in the triangular lattice, it could not be in the square lattice. From experience, the overlap factor $\alpha = 1$(FWHM= $1.7d$) is sufficient for 2D isotropic lattice(square and triangular). The results with $\alpha = d$ is shown by broken lines in Fig. 4.3, and results with smaller overlap $\alpha = 0.63d$(dotted lines) are compared in lower frequencies. In the case of smaller overap, the obtained line is diverted from the solution in $k \to 0$, which means difficulty in reproducing a constant field with smaller

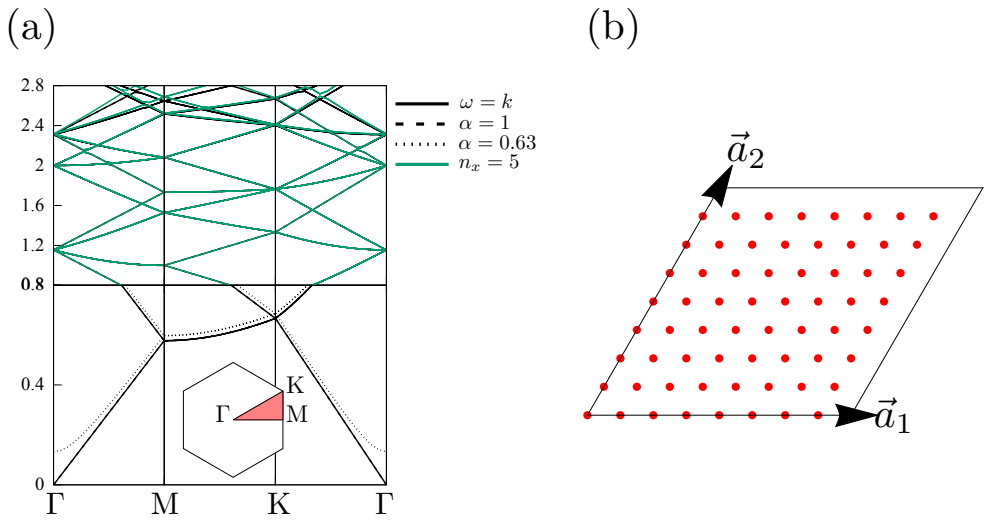

Figure 4.3: (a) The empty bands obtained by the 2D gaussian expansion and the solution $\omega = c|\vec{k}|$(solid lines). In frequencies lower than $\omega = 0.8$, results with $\alpha = d$ and $\alpha = 0.63d$ are compared with the solution. The obtained line for the $\alpha = 0.63d$ is diverted from the solution line in $\omega \to 0$. The empty bands of $n_x = 8$ and $n_x = 5$ with the α of both being 1 are also compared in higher frequencies. In higher frequencies $\omega > 2.4$, the lines of $n_x = 5$ do not lie on the solutoin line. (b) The configuration of gaussian bases for the triangular lattice.

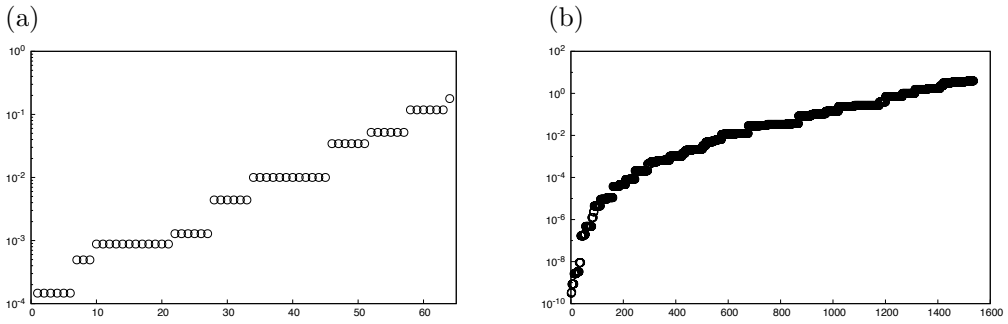

Figure 4.4: Eigenvalue spectrum of the overlap matrix of the gaussian basis sets with periodic boundary condition ($k = 0$), plotted in the ascending order. (a)The result of the scalar gaussian basis set in the 2D triangular lattice with $n_x = 8$ and $\alpha = d$. The ratio $\lambda_{\max}/\lambda_{\min}$ is 1.2×10^3. (b)The result of the vector gaussian basis set in the 3D fcc lattice with $n_x = 8$ and $\alpha = d$. The ratio $\lambda_{\max}/\lambda_{\min}$ is 1.2×10^{10}.

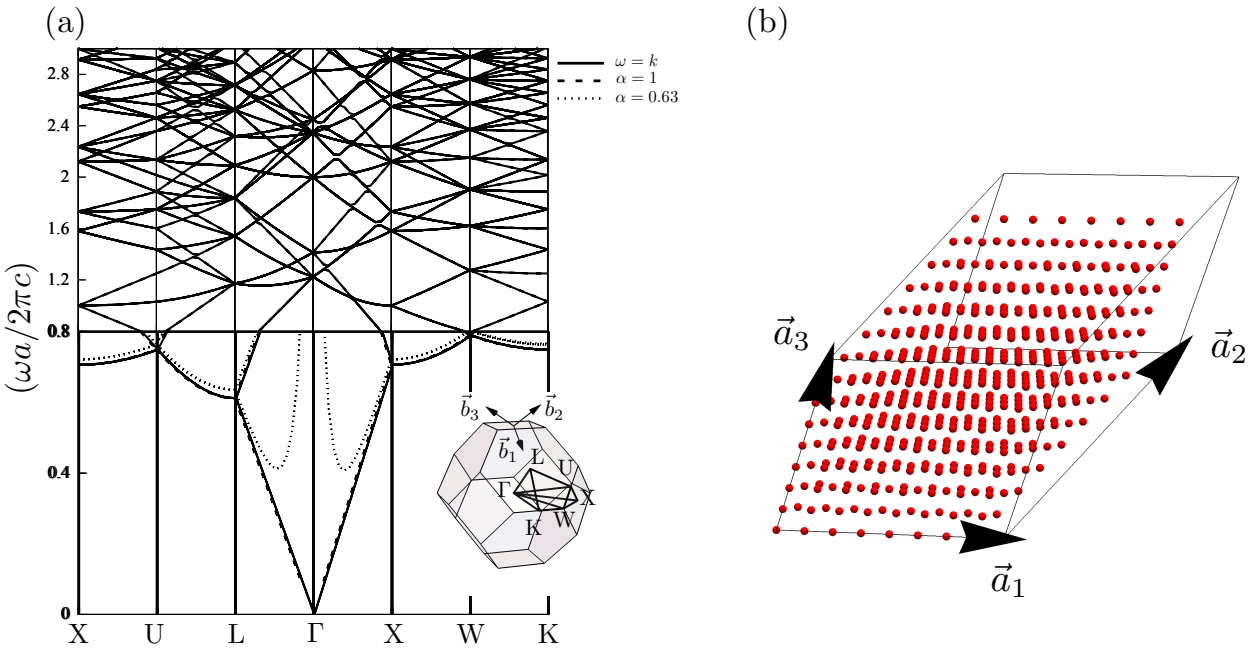

Figure 4.5: (a) The empty bands obtained by the 3D gaussian expansion and the solution $\omega = c|\vec{k}|$(solid lines). In frequencies lower than $\omega = 0.8$, results with $\alpha = d$ and $\alpha = 0.63d$ are compared with the solution. The lowest band for the obtained results do not reach to the origin($\omega = 0$,$k = 0$). The obtained bands for the $\alpha = 0.63d$ do not lie on the solution line in $\omega \to 0$. The empty bands of $n_x = 8$ are also compared in higher frequencies. (b) The configuration of gaussian bases($n_x = 8$) for the FCC lattice.

overlaps. Althoug the overlap between gaussian basis at any two points is not stritically zero, we truncate the matrix element at cetertain distance in practice. The slow decay of the gaussian function leads to increase of the band length in the matrix. The band length is well represented by the eigenvalue of the overlap matrix $\lambda_{\max}/\lambda_{\min}$. The smaller the ratio between maximum and minimum eigenvalue of the overlap matrix is, the shorter the band length of the matrix is and a basis set with a smaller ratio $\lambda_{\max}/\lambda_{\min}$ behaves better in matrix computations. The spectrum of the eigenvalue for several localization factors α are shown in Fig. 4.4. The correctness in higher frequencies(shorter wavelengths), on the other hand, depends on the density of the basis functions. From experience the $n_x = 8$, for which $n_x^2 = 64$ bases in total are required, satisfactory within the frequency region of the Fig. 4.3. hIn Fig. 4.3, the results with fewer basis functions($n_x = 5$) are compared with that of $n_x = 8$, where the α is fixed to d. In higher frequencies $\omega \approx 2.8$, it is seen that the result for $n_x = 5$(green line) is shifted from the solution, which means insufficiency in number of gaussian bases for those wavelenghts.

3D bases

In the three-dimensional case, we have to use the 3D gaussian basis elements(Eqs. 4.16). The 3D basis is more unstable than the scalar basis since it is obtained by taking derivative of the gaussian function one time. Also, since the 3D basis (Eqs. 4.16) is odd in parity, it is orthogonal to a constant field, that is,

$$\int \mathrm{d}^3 r\, \boldsymbol{g}^{(1)}(\boldsymbol{r}) \cdot \boldsymbol{e}_0 = 0,$$

where $\vec{e}_0$ is a constant vector directed to arbitrary direction. As a consequence, it can not reproduce the constant field($k = 0$ state), as seen at the frequency $\omega = 0$ in Fig. 4.5. Because of the multiplication by x, y or z, the basis elements $\vec{g}^{(i)}$s have learger overlaps with the same α. From experience, at least $n_x = 8$ gaussian bases per direction are required for the 3D problem and it requires $3 \times n_x^3 = 1536$ bases in total. In Fig. 4.5, the empty bands of fcc lattice obtained by the gaussian basis expansion with $\alpha = d$ and $\alpha = 0.63d$ are compared with the solution $\omega = |\vec{k}|$. In the figure, the lowest band for the gaussian expansion does not extend to the original point($\omega = 0$, $k = 0$) for the reason mentioned above. In lower frequencies(less tha $\omega = 0.8$), the difference

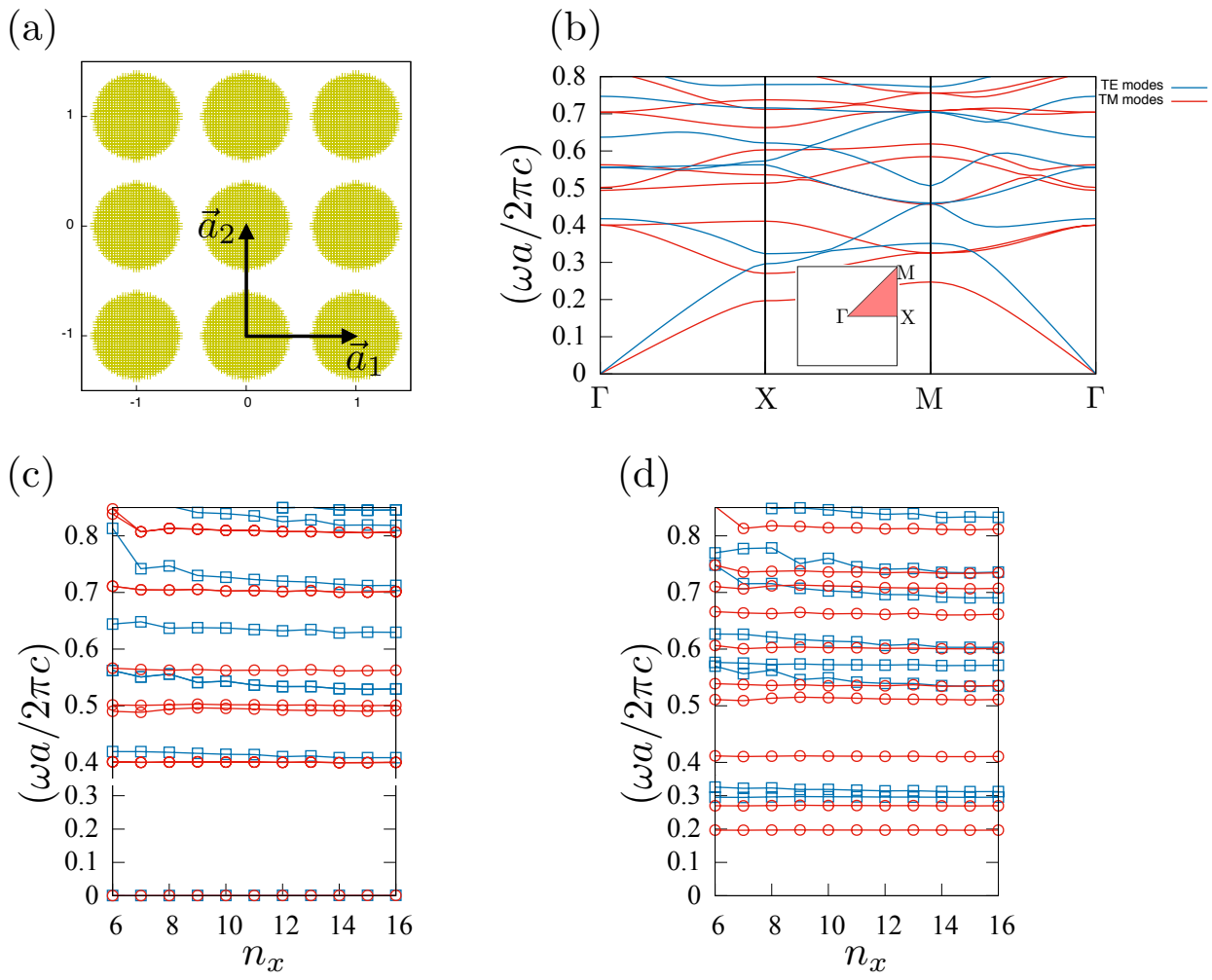

Figure 4.6: (a)Configuration of dielctric cylinders. Dielectric constatnt is set to $\varepsilon = 8.9$, and radius of the cylinder is set to $r = 0.378$, which is same as in Dobson's study [72]. (b) Calculated band structure of TE mode(blue line) and TM mode(red line) in the photonic crystal. The computation is performed using 64 (8×8) bases with $\alpha = d$. (c),(d) Convergence of eigenvalues at Γ or M point against number of bases in one direction n_x. The localization factor α is set to d(d is interspacing between gaussian bases).

for$\alpha = 0.63d$ is more prominent than the scalar basis. For frequencies higher than 0.8, we compared the results of $n_x = 8$ only, since we found it is difficult to truncate the overlap between gaussian bases for n_x less than 8. Within the frequencies plotted in the Fig. 4.5, it seems that the gaussian expansion with $n_x = 8$ and $\alpha = d$ well reproduce the solution $\omega = |k|$.

Test for photonic crystals

2D dielectric photonic crystal

First, we choose the array of dielectric columns arranged on square lattice as a sample system for the 2D Gaussain basis set. We assume the radius of the column to be $0.378a$ with a lattice length, and dielectric constant $\varepsilon = 8.9$ ($\varepsilon = 1.0$) in cloumns (in air) [72]. The structure of the dielectric material, where the numerical integral is performed, is plottede in the Fig. 4.6(a). There is little difference in the numerical integral between TE mode and TM mode. For TE mode(the electric field is perpendicular to the cylinder), numerical integral is required for obtaining the $\hat{L}_H$,

$$\hat{L}_{H,ij} = \int_{\boldsymbol{r}\in V} \mathrm{d}^2 r \, \left(\partial_y, -\partial_x\right) g_i(\boldsymbol{r}) \cdot (\varepsilon(\boldsymbol{r}) - 1)\, \hat{I}, \begin{pmatrix} \partial_y \\ -\partial_x \end{pmatrix} g_j(\boldsymbol{r}) \tag{4.23}$$

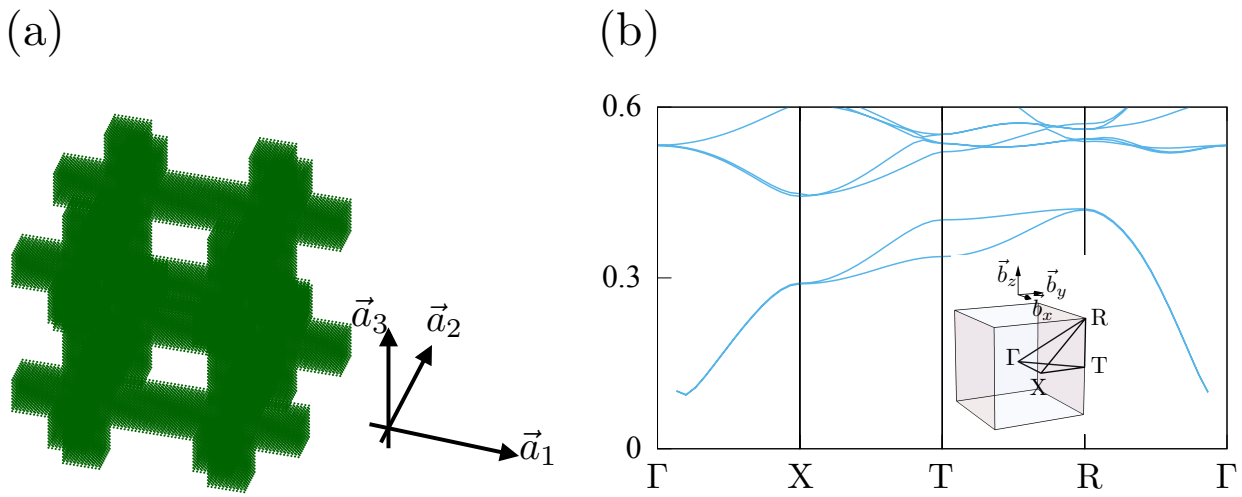

Figure 4.7: (a) The 3-dimmensional scaffold rod structure with width of rod being $0.74a$ and permittivity ε 13.0 and (b) Calculated band structure, which is obtained by using 1,536 bases with $\alpha = d$.

where the integral is perfomed only within the dielectric material(denoted as V). On the other hand for TM mode(the electric field is parallel to the cylinder), numerical integral is required for the $\hat{R}_E$

$$\hat{R}_{E,ij} = \int_{\boldsymbol{r}\in V} \mathrm{d}^2 r \; g_i(\boldsymbol{r}) \left(\varepsilon(\boldsymbol{r}) - 1\right) g_j(\boldsymbol{r}). \tag{4.24}$$

As for finnes of the numerical integral, the integral mesh of $\alpha/5$ is sufficient for gaussian bases because the result converges and does not change for finner integral meshes. The plot of strcuture in the Fig. 4.6a consists of points on which the numerical integral is actually perfomed for gaussian bases with $\alpha = d$, $n_x = 8$. The computed dispersion for TE modes (blue lines) and TM modes (red lines) are shown in Fig. 4.6b. The computation is perfomed by using $64(8\times 8)$ scalar Gaussina bases with localization factor $\alpha = 64.0$(as in the broken line in the Fig. 4.3).

In Fig. 4.6c,d, convergence of eigenvalues at Γ or M point against the number of bases in one direction n_x, on which the fineness of the computation depends, is shown. These figures indicate that most eigenvalues that are $\omega < 0.6$ converge till $n_x = 8$. From these figures we can observe that lower eigenvalues converge faster, representing that EM fields with shorter wavelengths require more n_x. Also, TE modes dispersion have better convergence than TM modes. For TM modes, discontinuitie occurs in all of the electric vector at straigh interface while for TE mode, it is only for tangental component at cylindrical interface and this difference between TE and TM modes seems to be the cause of slow convergence for TM modes. The results seem to be consistent with those obtained by Dobson [72], except the degenerated 3rd and 4th bands of TE mode around Γ point. Also, it does not seem to much the result of Dobson(Fig. 4.6(c)) by increasing n_x.

3D photonic crystals

Next, we choose a simple scaffold structure, namely a 3-dimmensional square rod structure analyzed by Sözüer and Haus [78], for the test of 3D Gaussian basis set. We assumed the width of the rod as $0.26a$ and permittivity ε as 13.0, which is the same setting as that structure in the study of Dobson *et.al.*. [74]. The dispersion calculated by using $1,536$ bases with 512 (8^3) grid points and 3 bases on each point for differnt directions and the localization factor $\alpha = 55.8$ is shown in Fig. 4.7a. As known, the photonic band structure has a complete band gap between the 5th band and 6th band. In this case of inhomogeneous permittivity also, as in homogeneous systems, the lowest eigenstate at Γ point cannot be restored by the vector Gaussian basis expansion. However except the point, the entire profile of the band structure is consisten with that of the previous works. In Fig.4.7b,c convergence of eigenvalues at Γ or M point against the finnnes n_x is shown. For this vector Gaussian basis set, eigenvalues does not converge monotonically, which is different to the scalar Gaussian basis set. Most eigenvalues lower than the gap frequency convege till $n_x = 8$.

4.3 Conclusion

In this chapter, we developed the gaussian expansion method for the Maxwell equations for numerical evaluation of topological invariants of photonic bands. In practical diagonalization by a finite number of bases, the eigenequation for Bloch states are periodic in the wavenumber only when the continuous fields are expanded by a spatially localized basis set. We can numerically evaluate topological invariants directory from eigenvectors obtained in a spatially localized basis set, while in the case of plane waves it is required that maximally localized wannier orbitals are obtained and the eigenvectors are given by the wannier orbitals. However for photonic band structures, it is not always easy to find a so called *composite bands* that are separated by the gap with vanishing Chern number from above and below, in specific for topologically non-trivial photonic band structures. Since the gaussian basis is smooth, it is good at dealing with curved surfaces and it is advantageous to the finite element method in that it does not require a particular mesh for each structure. This property is also advantageous in a problem we will deal with in the Chapter 7, where we will consider structural deformation and Chern numbers for it. In the problem, use of the gaussian expansion method is indispensable since the structural deformation requires different mesh alignments in the finite element method and it makes difficult to take the inner product between eigenstates of different structures. Further, the method also can be applied to other continuous systems such as elastic materials.

Chapter 5

Topological photonic band structures in 3D uniaxial chiral structures

In this chapter, we consider the way for finding topologically protected photonic edge modes in dielectric (non-magnetic) photonic crystals, just by breaking the spatial inversion symmetry of the structure. The 1st Chern number is defined a band structure on the 2D parameter space. However, for a fully 2D system, existence of TRS must lead to vanishment of the Chern number and topologically non-trivial band structure requires a TRS breaking effect such as use of a magnetic material in the photonic crystal. On the other hand, in a 3D system, the Bloch wave vector has three components and then one component remains. We can consider to fix one of them, say k_3, and obtain a 2D slice($k_1 - k_2$) of the Brillouin zone. We call the Chern number on the 2D slice as the section Chern number $C_{n,12}(k_3)$, which is function of k_3. The section Chern number can have a non-zero value by breaking either of the time-reversal or spatial inversion symmetry. The price of this is the requirement of the fixed momentum in one direction.

The non-zero section Chern number occurs when the 3D band structure have a isolated degeneracy point called Weyl point. Although the Weyl point in the photonic band structure is realized in the double gyroid photonic crystal with spatial inversion breaking modulation in the structure [79,80], the structure is complicated and fabrication is only realized in cm scale by drilling a dielectric material. Since the wavelength scale of the photonic band structure depends on the length scale of the photonic crystal structure, the Weyl point related effect in a shorter wave scale requires a structure in a finer scale. The structure is much simplified by discarding the isotropy of the structure. The uni-axially chiral structure serves a topologically non-trivial band structure in the 2D slice for the fixed momentum in the axial direction.

In the first section, we describe a photonic band structure of a photonic crystal formed by shaving helical holes on a honeycomb array in a dielectric material and properties of edge modes propagation there. Without twist, the structure is uniform in the axial direction and nodal lines extends in the structure because of the inversion symmetry. By deforming the columns into helices, the inversion symmetry is broken and the nodal lines of degeneracy reduce to nodal points. In the later section, we describe a photonic band structure of chiral woodpile photonic crystals. The chiral woodpile structures has a lot of similar properties to the array of dielectric helices. The woodpile structure has already been fabricated in the laboratory in a few tenths of μm. The light propagation reflecting the topological edge modes is further studied.

5.1 Weyl points and section Chern number in 3D crystals

Section Chern number

The first Chern number is topological invariant defined to the wavefunctions in the 2−dimensional Brillouin zone. For $d-$dimensional parameter space, the section Chern number in the ${}_dC_2$ slice of the Brillouin zone is given as a function of the rest parameters [38]. As before, the berry connection and curvature is given as

$$A_{n,i} = \langle \psi_n | \partial_i | \psi_n \rangle \tag{5.1}$$

$$B_{n,ij} = \partial_i A_j - \partial_j A_i. \tag{5.2}$$

In a 3D system, the wave vector consists of three components, k_1, k_2, and k_3, and the section Chern number is defined by two of them, as a function of the remaining one. If we fix k_3, the section Chern number $C_{n,12}(k_3)$ is defined as

$$\begin{aligned} C_{n,12}(k_3) &= \frac{1}{2\pi \mathrm{i}} \int \mathrm{d}k_1 \mathrm{d}k_2 \; B_{n,12}(\boldsymbol{k}), \\ B_{n,12}(\boldsymbol{k}) &= \partial_{k_1} A_{n,2}\,(\boldsymbol{k}) - \partial_{k_2} A_{n,1}\,(\boldsymbol{k}), \\ A_{n,i}(\boldsymbol{k}) &= \langle \psi_n(\boldsymbol{k}) | \partial_{k_i} | \psi_n(\boldsymbol{k}) \rangle. \end{aligned} \tag{5.3}$$

As mentioned in a previous section, (spin-less)TRS relates the Berry curvature between at $\vec{k}$ and $-\vec{k}$. In a TRS system, the complex conjugate of an eigenstate is also an eigenstate $\mathcal{T}|\psi_n(\vec{k})\rangle = |\psi_n(\vec{k})\rangle^* = |\psi_n(-\vec{k})\rangle$. Then, the berry connection is related as $A_{i,n}(-\vec{k}) = \langle \psi_n(-\vec{k})| - \partial_i |\psi_n(-\vec{k})\rangle = \langle \psi_n(\vec{k})| - \partial_i |\psi_n(\vec{k})\rangle^* = A_{n,i}(\vec{k})$, since $\langle \psi_n(\vec{k}) | \partial_i | \psi_n(\vec{k}) \rangle = 1$ and $Im[\langle \psi_n(\vec{k}) | \partial_i | \psi_n(\vec{k}) \rangle] \in \mathbf{I}$. Then the berry curvature is related as $\vec{B}_n(-\vec{k}) = -\vec{B}_n(\vec{k})$, since $\vec{\nabla}_k \times \vec{A}_n(-\vec{k}) = -\vec{\nabla}_{-k} \times \vec{A}(-\vec{k}) = -\vec{B}(\vec{k})$. Then, if the parameter space is fully two-dimensional, that is if the $-\vec{k}$ is also included in the integral, the contributions from them cancel each other and the Chern number must vanish. On the other hand, for a 2D slice in the 3D Brillouin zone, time reversal point $-\vec{k}$ is not included in the slice including the $\vec{k}$ except the slice of $k_3 = 0, \pi$. However, if the system is invariant under spatial inversion, the spatial inversion of an eigenstate $R_{\mathcal{I}} \psi_{n,k}(\vec{r}) = \psi_{n,k}(-\vec{r}) = \psi_{n,-k}(\vec{r})$ is also an eigenstate. Then, the berry connection is related as $A_{n,i}(-\vec{k}) = \langle \psi_n(-k) | \partial_i | \psi_n(-k) \rangle = -\langle \psi_n(\vec{k}) | \partial_{k_i} | \psi_n(\vec{k}) \rangle = -A_{n,i}(\vec{k})$, and the Berry curvature is related as $\vec{B}_n(-\vec{k}) = -\vec{\nabla}_{-k} \times \vec{A}_n(-\vec{k}) = \vec{B}_n(\vec{k})$. Then the combination of the TRS and spatial inversion relates $\vec{B}_n(\vec{k}) = -\vec{B}_n(-\vec{k}) = -\vec{B}_n(\vec{k})$ and the berry curvature vanishes at any point in the 3D Brillouin zone. Therefore, the section Chern number can have a finite value by breaking either of the TRS or spatial inversion symmetry. Therefore, by focusing of a three-dimensional structure without spatial inversion symmetry, we can find topologically protected edge mode propagation with a (non-magnetic)dielectric photonic crystal.

Weyl point

In a TRS system, the section Chern number in the inversion invariant slice ($k_3 = 0, \pi$) must vanish because of the cancellation of the berry curvature between $\vec{k}$ and $-\vec{k}$ points. The section Chern number is well-defined if the band structure in the slice is gapped. Varying the k_3, the change of the section Chern number into a non-zero value is caused after the gap closes and reopens, that is quantum transition with varying k_3. This means, viewed in the 3D Brillouin zone, that the degeneracy lies as a nodal point. The nodal point in the 3D point is called as a Weyl point.

When the slice passes through a single Weyl point, the change in the section Chern number is either of ± 1, and this difference of Weyl point is ascribed to the topological charge. Since the surface integral $\int_{k_3 = k^* + \delta} \mathrm{d}k_1 \mathrm{d}k_2 \; - \int_{k_3 = k^* - \delta} \mathrm{d}k_1 \mathrm{d}k_2$, where the slice $k_3 = k^*$ include the single Weyl point is continuously deformed into the surface integral on a sphere, the integral is quantized according to the Weyl point charge as $2\pi \mathrm{i} C$. The existence of certain symmetry in the system gives notice other Weyl points on the start of k, and according to the type of symmetrical operation, the Weyl point charge is found. If two points are related by a rotation $\vec{k} \to R\vec{k}$, the Berry connection at $\vec{k}$ and $R\vec{k}$ are also related as $\vec{A}(\vec{k}) \to R\vec{A}(R^{-1}\vec{k})$ and since the value of the curvature is independent of the choice of the coordinate, it is also related as $\vec{B}(\vec{k}) \to R\vec{B}(R^{-1}\vec{k})$ Then, the surface integrals on tiny spheres surrounding the Weyl points at $\vec{k}^*$ and $R\vec{k}^*$ are related as

$$\int_{S^2(R\boldsymbol{k}^*)} \mathrm{d}k^3 \; \boldsymbol{B}(\boldsymbol{k}) \cdot \boldsymbol{n}(\boldsymbol{k}) = \det|R| \int_{S^2(\boldsymbol{k}^*)} \mathrm{d}k^3 \; \boldsymbol{B}(\boldsymbol{k}) \cdot \boldsymbol{n}(\boldsymbol{k}),$$

and the topological charge is same (different) if the rotation does (not) include spatial inversion $\det|R| = 1(-1)$. TRS also gives notice the Weyl point at $-\vec{k}^*$. In this case, the relation of the topological charges is different from the case of spatial rotation since time reversal operation relates berry curvature as $\vec{B}(-\vec{k}^*) = \vec{B}(\vec{k}^*)$, whereas $\vec{B}(-\vec{k}^*) = -\vec{B}(\vec{k}^*)$ in the case of spatial inversion. Then, two Weyl points related by the TRS has a same Weyl point charge.

As known as the *no-go theorem* [81], the Weyl point in the periodic system must exist as a pair with the opposite chiralities. This can be simply explained by the section Chern number. Since the section Chern number is periodic in k_3, if the section Chern number changes from the original value, it must change with the opposite value until returning to the periodic point, meaning the existence of the Weyl point with the opposite charge.

Further for the TRS case, the section Chern number is zero at both of $k_3 = 0$ and $k_3 = \pi$. Then if the section Chern number changes from zero, it must return to zero again until $k_3 = \pi$. Further, the TRS guarantees the existence of Weyl point at the inversion point $-\vec{k}$ with the same topological charge. Therefore, the Weyl points appear as a set of four points in a TRS system. In addition, for a system with TRS, chirality of the structure is necessary for the following reason. First, TRS gives additional Weyl point at $-\vec{k}^*$ with the same topological charge. A mirror plane gives other two Weyl points with the opposite charge, and in this configure, both planes perpendicular and parallel to the mirror plane must include two Weyl points with the opposite charge at the same time and then the section Chern number can not change. Therefore, chirality in addition to just breaking spatial inversion symmetry is required. For example, a uniform stacking of two-dimensionally inversion broken structure brakes inversion symmetry but not chiral and the section Chern number is always zero.

Since Weyl points must exist as a pair with the opposite chiralities, the existence of Weyl point is topologically stable. It does not disappear with an arbitrary modulation of the system, though it moves in the Brillouin zone. The topological stability of the Weyl point is also seen from the two-band degeneracy. As denoted by Berry [37], an hermitian 2×2 matrix is given by the three Pauli matrices and three real coefficients

$$H_{2\times 2} = R_x\sigma_x + R_y\sigma_y + R_z\sigma_z = \begin{pmatrix} R_z & R_x - \mathrm{i}R_y \\ R_x + \mathrm{i}R_y & -R_z \end{pmatrix} \qquad \boldsymbol{R} \in \mathbf{R}^3.$$

In general for a band structure, the values of the coefficients change with the change of the wave vector $\vec{k}$. The wave vector is related to the parameter space $\vec{R}$ by the hamiltonian as $f_H(\vec{k}) = \vec{R}(\vec{k})$. The eigenvalue of the hamiltonian is given by

$$\varepsilon = \pm\sqrt{R_x^2 + R_y^2 + R_z^2}.$$

Then the Weyl point in the Brillouin zone $\vec{k}*$ is identified as the point satisfying $f_H(\vec{k}^*) = \vec{0} \in \vec{R}$. In general, the map f_H of the three-dimensional Brillouin zone to the parameter space is a three dimensional object. A continuous modulation of the system deforms the object in the $\vec{R}$ space. If the 3D object includes the origin in the $\vec{R}$ space, the Weyl point(the inverse mapping of the origin) remains until the origin goes out of the 3D object by the modulation and thus the Weyl point in the 3D Brillouin zone is topologically stable. Although the mapping of the 3D Brillouin zone in the $\vec{R}$ space is in general a 3D object, existence of a certain symmetry restricts the mapping in a confined space in the $\vec{R}$ space. For example, invariance under the combination of time reversal and spatial inversion restricts the 2×2 hamiltonian to the real valued hamiltonian and it vanishes the R_y. The mapping under the symmetry is restricted to the 2D $R_x - R_z$ plane. In this case, co-dimension of the mapping is one, and then if it includes the origin, the node extends as a line in the 3D Brillouin zone.

5.2 The dielectric photonic crystal of twisted columns arranged on honeycomb lattice

5.2.1 physical system

Honeycomb array of air hole columns

Then, we consider to realize Weyl points in photonic crystals. Our strategy is to begin with a inversion symmetric structure and find a degeneracy line. Then, by adding an inversion breaking modulation we dissolve the degeneracy line into a degeneracy point. In order to observe chiral edge modes appearing as the bulk-edge correspondence to the finite section Chern number $C_n(k_3)$, it is required to have a clear gap on the entire two-dimensional slice for a fixed k_3. Since a clear gap is required only on a 2D slice of k_3, it is appropriate to start with a two-dimensional system having pseudo-gap, a frequency region filled with only a few bands, and then to apply appropriate three-dimensional modifications to the structure.

We begin with a photonic crystal of hollow columns aligned on the honeycomb lattice as depicted in Fig. 5.1(a). We set the dielectric constant of the background medium to be $\varepsilon = 20$. The lattice constant of the triangular lattice is taken to be $a = 1$ for simplicity. The radius of the hollow cylinder is taken as $r = \sqrt{3}/6$, which is maximum radius that does not overlap between cylinders on honeycomb lattice. The band structure obtained by solving the 2D eigenequation is shown in Fig 5.1(b), where TE(TM) modes are shown by the

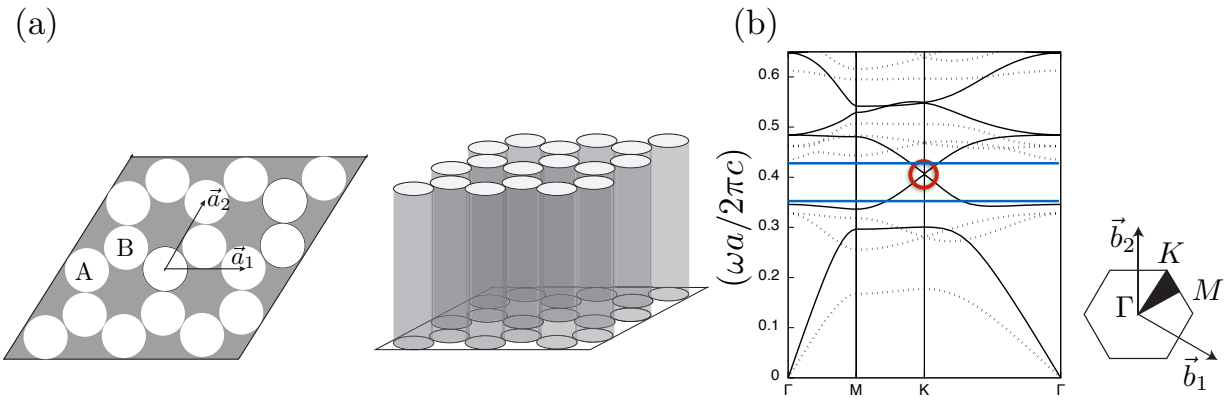

Figure 5.1: Reprinted from [75] with the permission of American Physical Society. (a) A schematic of the photonic crystal consisting of the array of hollow cylinders on honeycomb lattice. The structure has sub-lattice degree of freedom A, B on the cylinders. The dielectric constant in the back ground material is set to $\varepsilon = 20$ and it is set to $\varepsilon = 1$ within the cylinder. The basic translation vectors forms a triangular lattice and the lattice constant is taken as $a = 1$. The radius of the cylinder is set to $\sqrt{3}/6$, which is the maximum radius for which the cylinders do not overlap. (b) The photonic band structure obtained by solving the 2D eigenequation for both of TE(solid line) and TM(broken line) modes. The degeneracy point(noted by the red circle) is distinctive in the frequency region enclosed by blue lines

solid(broken) lines. The band structure of this system has some similarity to that of the triangular lattice, which consists of dielectric columns [82]. The resemblance is obvious noticing the complementary region of the hollow honeycomb lattice composes a triangular lattice. In spite of this resemblance, we prefer to use the hollow honeycomb lattice in Fig. 5.1(a), since it has the sub-lattice structure of the honeycomb lattice and we will make use of this degree of freedom in the following discussion. Without three-dimensional modulation, the second and third TE modes of the hollow honeycomb lattice form 2D Dirac cones at K and K' points, and TM modes do not mask these TE Dirac cones.

Owing to spatial inversion symmetry of the hollow honeycomb lattice, these TE Dirac cones are actually line degeneracies extending in the k_3 direction (Fig. 5.2). The photonic band structure in the Fig. 5.2 is obtained by solving the 3D eigenequation and note that there exist lines with almost flat band dispersion, as frequently found on a line such as the H-L line. Those modes correspond to guided mode, which propagates along the axial direction and strongly confined within the dielectric region. To break the line degeneracy into Weyl points, spatial inversion symmetry should be broken and we reshape each hollow cylinders into a hollow helix. Owing to the sub-lattice degrees of freedom, we can modulate columns differently on sub-lattices A and B of the honeycomb lattice.

Weyl points and change in section Chern number

First, let us consider to apply the same twist on the both hollows at sub-lattices A and B (Fig. 5.3). By reshaping columns into helices, spatial inversion symmetry is broken and the line degeneracy is lifted except K or K' point, which means emergence of the Weyl points. This reduction of degeneracy is explained in terms of the point group symmetry as followings. Without the twist, the system has D_{6h} symmetry, and the group of k is C_{3v} on the line parallel to the k_3 axis passing through K or K' points and specifically it is D_{3h} for K and K' points. Since both of C_{3v} and D_{3h} contain two-dimensional representations, twofold degeneracy is allowed on the whole line, which supports the line degeneracy without twist. Then, with the twist, the reflection symmetry with respect to a plane including the z axis is broken and the group of k on the line parallel to the k_z axis passing through K and K' points reduces to C_3, except K and K' points. This implies the degeneracy dissolves except K and K' points since C_3 does not contain any multidimensional representation. For K and K' points, however, the group of k changes from D_{3h} to D_3. By the compatibility relation, 2D representations of D_{3h} are connected to

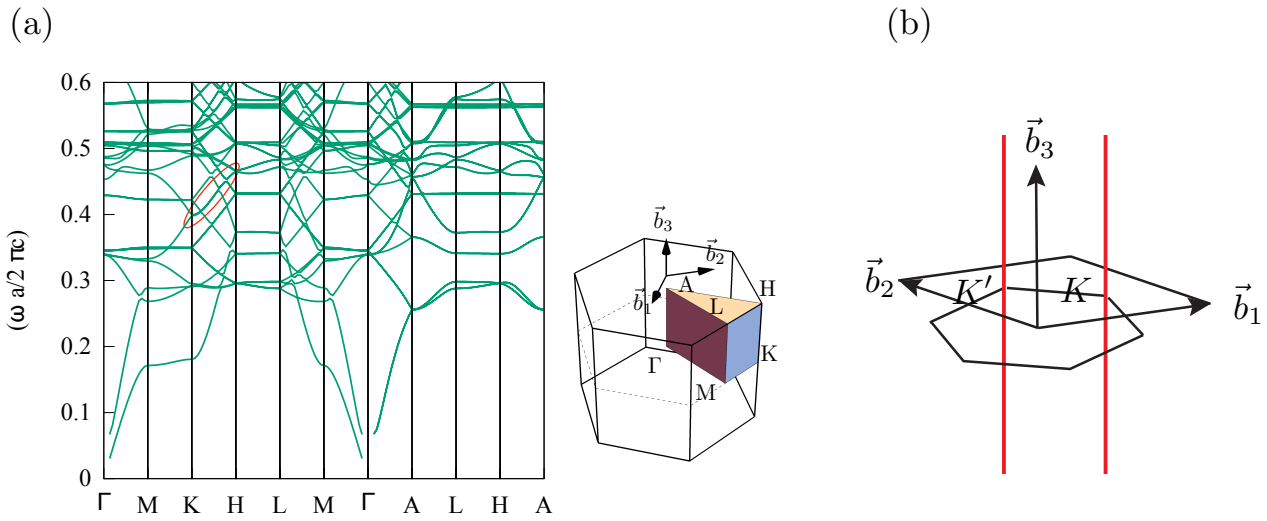

Figure 5.2: (a)Photonic band structure of the honeycomb cylindrical holes(Fig. 5.1(a)). The 2D dirac point is placed on the K point around the frequency $\omega \approx 0.4$. The degeneracy extends as a line in the 3D Brillouin zone as denoted by the red circle. (b) The nodal lines in the 3D Brillouin zone.

2D representations of D_3, and thus, the degeneracies at K and K' points survive even with the twist[1].

The surviving degeneracy are two Weyl points with the same chirality since these points are related by two-fold rotation around the z axis. Then, the section Chern number $C_n(k_3)$ changes by ± 2 when k_3 crosses $k_3 = 0$, because of *two* Weyl points on the $k_3 = 0$ plane [Figs. 5.3(b) and 5.3(c)]. Also,the same argument applies for the $k_3 = \pi$ plane, but the Weyl points on the $k_3 = \pi$ plane can not be observed, since the bands on which we focus merge into the other bands in increasing k_3 from 0 to π.

Next, we consider to change the twist of helix only for the one on the sub-lattice B [Fig. 5.4(a)]. With this modification, the twofold rotational symmetry around the z axis and the axis perpendicular to z axis no more exist and there is no reason for the two Weyl points are confined within the $k_z = 0$ plane. However, the Weyl points found in Fig. 5.3(c) do not simply disappear because Weyl points are topologically stable object and only disappear by annihilating as a pair of Weyl points with opposite chiralities [81][2]. Our numerical calculation shows that the Weyl points move to $\pm k_z$ directions as we increase the difference of the twists between sub-lattices. When one of the Weyl points moves in $+k_z$ direction, the other one moves in $-k_z$ direction due to TRS. In this case, the dispersion is gapped on the $k_z = 0$ plane, and we have $C_n(0) = 0$, which is consistent with the statement of the previous section. The section Chern number changes for large enough k_z as expected from the existence of the Weyl points. We can regard the non-zero k_z in the inversion broken structure as a TRS breaking effect in the 2D slice. Also, the broken π-rotational symmetry can be regarded as a inversion breaking effect in the 2D effect. Then, the transition at the finite k_3 can be regarded as the topological transition in the Haldane's honeycomb model for non-zero M.

Edge modes

In order to investigate edge modes, we perform calculations using the gaussian basis elements on the truncated geometry in the $\vec{a}_1$ direction [see Fig. 5.5(b) for the definition of $\vec{a}_1$] with finite width (eight unit cells in specific). At the interface, we place a material with a smaller dielectric constant in order to prevent the light from leaking to outside. The cladding is necessary because the momentum/frequency region we are focusing on lies above the light cone (for the same dielectric constant with the hollow region), which means that the light leaks out of the system.

In Figs. 5.5 and 5.6, the dispersion relations of the finite width system are compared with the bulk dispersions projected on the surface for several values of k_3. We find several bands apart from the bulk contribution,

[1] In the other way, the point degeneracy is explained from the non-symmorphic(screw) symmetry of the strcuture, as explained in a following section

[2] This modification does not break the screw symmetry that gives point degeneracy on line passing the K or K' point parallel to the k_3. Even after the screw symmetry is broken, the degeneracy point remains because of the topological stability.

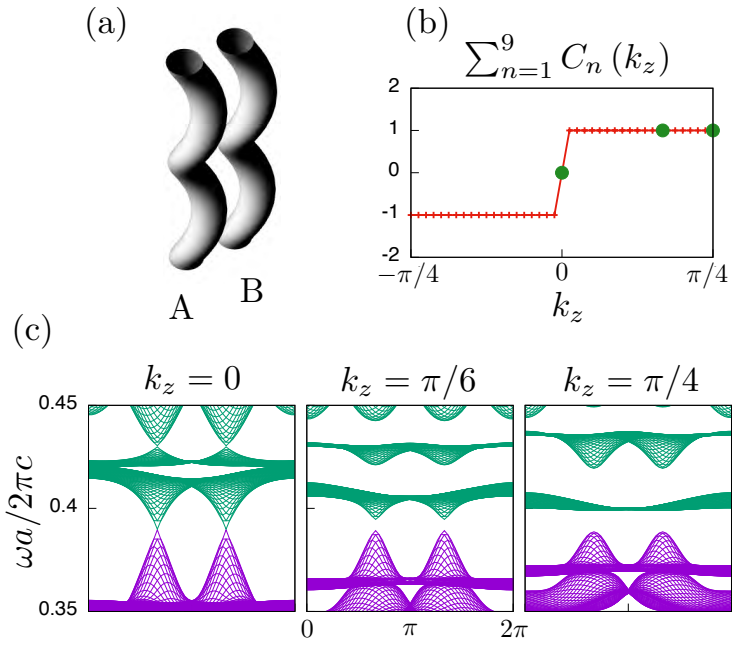

Figure 5.3: Reprinted from [75] with the permission of American Physical Society. (a)A schematic of the hollow shapes. The same twists are applied to sub-lattice A and B. The radius of the helix is taken as h_r = 0.05. (b) The value of the section Chern number as a function of the k_3. At k_3=0, the value changes by two due to two Weyl points at K and K' points. (c) Photonic band structures in the 2D slices at values of k_3 indicated by the green points in the Fig. (b).

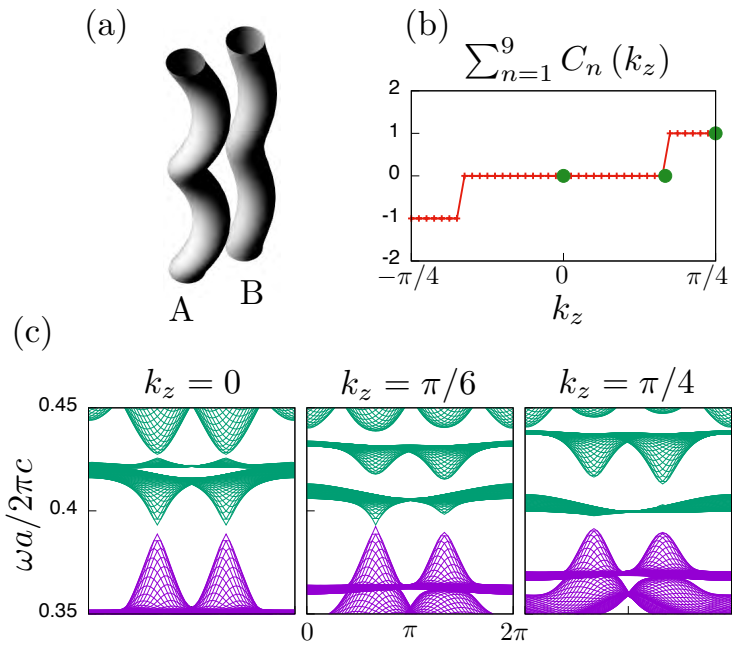

Figure 5.4: Reprinted from [75] with the permission of American Physical Society. (a)A schematic of the hollow shapes in the photonic crystal. The different twists are applied to sub-lattice A and B. The radius of the helix h_r is set to h_r = 0.05 for the sub-lattice A and to h_r = 0.03 for the sub-lattice B. (b) The value of the section Chern number as a function of the k_3. The Chern number changes twist by one each. (c) Photonic band structures in the 2D slices at values of k_3 indicated by the green points in the Fig. (b).

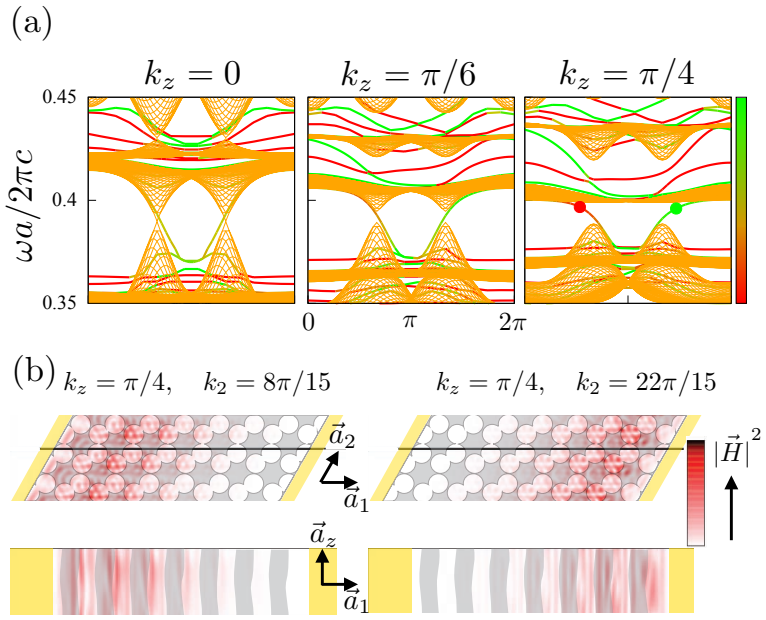

Figure 5.5: Reprinted from [75] with the permission of American Physical Society. (a)Photonic band dispersion in the cylindrical geometry of the structure of Fig. 5.3 plotted to k_2 for several values of k_3. The red(green) color on the line, which is determined from the moment of the eigenmode described in the main text, indicates the eigenmode is localized at the left(right) edge. (b)The cylindrical geometry of the structure, where the results in Fig. (a) are obtained. In the geometry, the system is periodic in the $\vec{a}_2$ direction but truncated with the finite width(8 unit cells) in the $\vec{a}_1$ direction. The region colored by yellow is filled with a perfect metal, which prevent the light leaking outside. The left(right) side image shows the intensity of the eigenfield of the mode indicated by the red(green) point in the Fig. (a). The bottom images show the intensity profiles of the eigenmode in the vertical intersection indicated by the line in the above figures(top images).

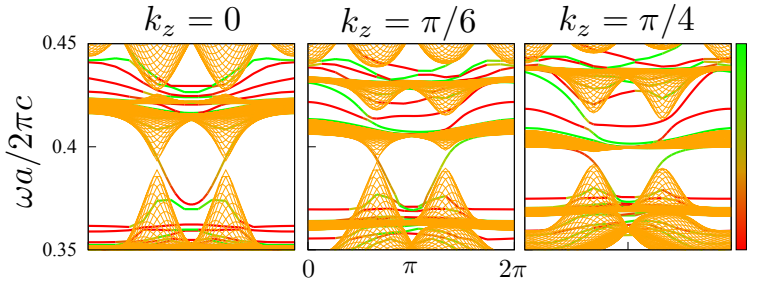

Figure 5.6: Reprinted from [75] with the permission of American Physical Society. (a)Photonic band dispersion of the structure of Fig. 5.4(different h_r for sub-lattice A and B) plotted to k_2 for several values of k_3 in the same geometry as the Fig. 5.5.

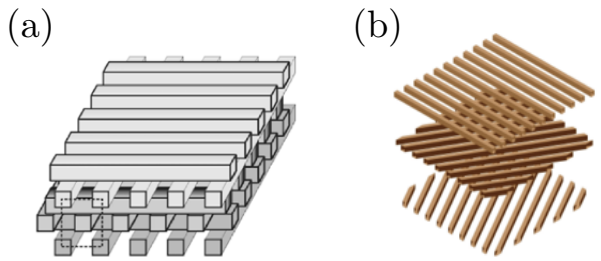

Figure 5.7: Two types of woodpile structures as examples. (a) The woodpile structure with fcc translational symmetry, which has 3D full gap in its band structure. (b) A Chiral woodpile structure stacked with $\pi/3$ in-plane rotation. For $n > 2$, $\pi/n-$rotational stacking forms a chiral structure.

which signals appearance of edge modes. In fact, it is confirmed that the non-bulk bands are localized at the interfaces by examining the eigenvector for each mode. From eigenvectors obtained, we can also examine on which side, left or right, each mode localizes. In Figs. 5.5 and 5.6, the red color on the line corresponds to the states on the left edge, while the green color on the line to the states on the right edge. The color spectrum is determined by the moment of the eigenfield $\langle r_1 \rangle_{\boldsymbol{H}_{n,k}} = \int \mathrm{d}^3 r \; r_1 \vec{H}^2_{n,k}(\boldsymbol{r})$. As we change k_z, the way that the edge modes connect bulk bands changes in accordance with the change of the sum $\sum_{n=1}^{9} C_n(k_z)$, which confirms the bulk-edge correspondence. Also, the same argument also applies to gaps other than the 9th gap with nonzero total section Chern number. When the fixed momentum is conserved for k_z with $\sum_{n=1}^{i} C_n(k_z)$ being nonzero, the wave propagates unidirectionally along the interface.

As discussed in the following chapter, this photonic crystal is similar to evanescently coupled twisted waveguides on honeycomb lattice studied by Rechtsman *et al.* [83]. In the system of evanescently coupled waveguides, the guide wave is described by the paraxial equation, where the z axis, the propagation direction of a waveguide mode, is regarded as the *temporal*. Then, the twist of a waveguide becomes a temporal periodic modulation for waveguide modes and the appearance of the chiral edge modes is attributed to the *Floquet* topological band structure. However, we related the unidirectional propagation of them to the finite value of section Chern numbers.

There might exist some waveguide modes near the frequency of the Weyl point and it could lead to coupling between edge modes and wave guide modes. In such a case, it is possible to avoid the mixing between the edge modes and the waveguide modes by shifting the relative positions of them in the frequency. The relative shift can be achieved by changing the pitch of the helix since the dispersion of wave guide modes is easily affected by the periodic length in the z direction, whereas that of TE-like modes is not so much.

5.3 Chiral woodpile photonic crystals

5.3.1 Circular dichroism of the chiral woodpile photonic crystal

The woodpile photonic crystal is constructed by simply stacking layers consisting of arranged rods. Because of its simple process, the woodpile structure is broadly adopted as a 3D photonic crystal. Despite its simplicity, the woodpile structure shows various functionality according to the ways of stacking. Perhaps, what rises in one's mind hearing a woodpile photonic crystal may be the woodpile structure with translational symmetry of fcc lattice Fig. 5.7. This structure is famous for its photonic band structure having three-dimensional band gap.

On the other hand, by stacking the layers with in-plane rotation, the structure becomes chiral, that is, stacking with π/n in-plane rotation and with $-\pi/n$ in-plane rotation are not identical. Several spiral structures made were reported to show circular dichroism for light along with its axial direction [84–86]. The circular dichroism in chiral woodpile structure for light along with the stacking direction was also reported [87, 88]. The explanation for this effect is given by considering the potential felt by circularly polarized light [89]. To be specific, we assume the woodpile is rotated in the anti-clockwise direction the stacking. The light propagating in the $+z$ direction with anti-clockwise circular polarization is effectively in resonance at wave length equal

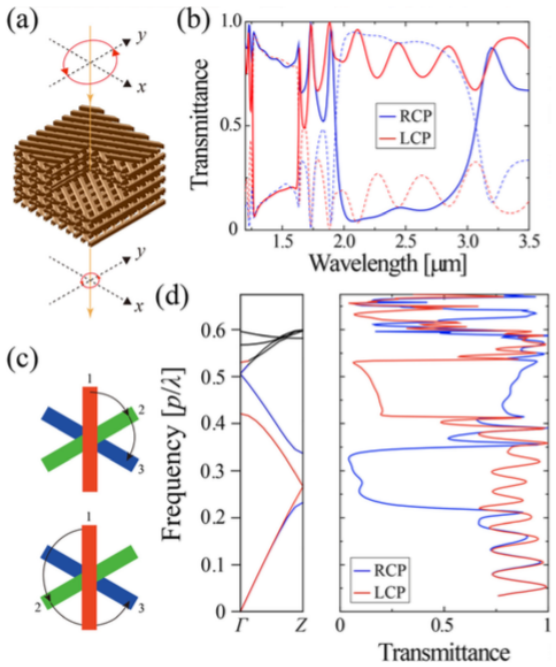

Figure 5.8: Reprinted from [88] with the permission of AIP Publishing. (a) The schematic of the $\pi/3-$rotational chiral woodpile structure studied by Takahashi *et.al.*, which consists of 16 layers (excerpted from [88]).(b) Comparison of transmittance of both circular polarization obtained from FDTD simulation. Two wavelength region $1.25\mu\text{m} < \lambda < 1.75\mu\text{m}$ and $2.0\mu\text{m} < \lambda < 3.0\mu\text{m}$ show clear circular dichroism. (c)Top view of the $\pi/3-$rotational chiral woodpile photonic crystal. Rotation angles after unit layer translation are different between the clockwise and anti-clockwise circular polarization. (d) Dispersion relation written for both circular polarization separately and the right figure is transmittance plot to the frequency.

to the thickness of six layers. This is because the rod rotates by $\pi/6$ with the propagation of the single layer and then the light of anti-clockwise circulation with wavelength equal to the thickness of six layers feels the effective 1D periodic potential Fig. 5.8.

On the other hand, the light with clockwise circular polarization gets in resonance at wave length equal to the thickness of three-layers, since for the clockwise circulation the single layer translation rotates the rod by $-2\pi/3$ Fig. 5.8. At resonant wave length, the circularly polarized light gets reflected by the Bragg reflection. Then, at prohibited wavelength for one circular polarization, only the another circular polarization can go through the structure and thus it causes the circular dichroism.

Fabrication of the structure

Each layer is made of dielectric materials such as GaAs. The array of rods, is formed by electron beam lithograpy and dry and wet etching. Then, the processed layers are stacked on a GaAs substrate one by one along the guiding post confirming each step by SEM image [90]. In current technology, the structure can be fabricated in scale of a few tenth of micro meters. In the study of the circular dichroism, The structure of this scale corresponds to near infra-red frequency for relevant effects. Also to avoid collapse, the thickness of the layer should be sufficiently thick.

Experimental measurement

Circular dichroism is studied by measuring the transmittance of each circularly polarized light along the stacking axis to varying frequency. For transmittance spectrum, a super continuum laser is used as a light source and it is induced through a broad band wave-plate and an objective lens with a relatively small numerical aperture in order that it behaves as a plane wave through the sample with finite thickness. Then the transmittance is

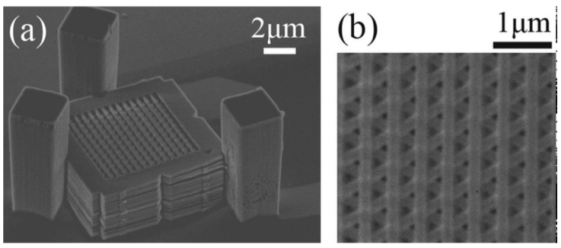

Figure 5.9: Reprinted from [88] with the permission of AIP Publishing. (a) Scanning electron micro-graph (SEM) image of the fabricated 3D chiral photonic crystal. 16 layers are stacked using three posts as a guide. (b) Top view of the structure. The crossing points arranged in a triangle lattice are aligned along the helical axes.

measured using a monochromator and photo-detector and taking the ratio of output power to input. For more detailed measures , a frequency tunable monochromatic laser is used and sweeped through the interested region and polarization or ellipticity of transmitted light is measured by using a quarter wave-plate and linear polarizer. Also correction to transmission thorough the substrate is required. For a truncated structure, the bulk band dispersion in the direction parallel to the surface is obtained by measuring the transmittance varying the direction of inducing light to the sample. If the thickness of the sample is taken sufficiently largely, only light belonging to the bulk mode is transmitted since edge modes parallel to the surface cannot enter into bulk and edge modes along the propagating direction is localized at the perimeter of the sample.

5.3.2 Band strcutures of the chiral woodpile photonic crystals

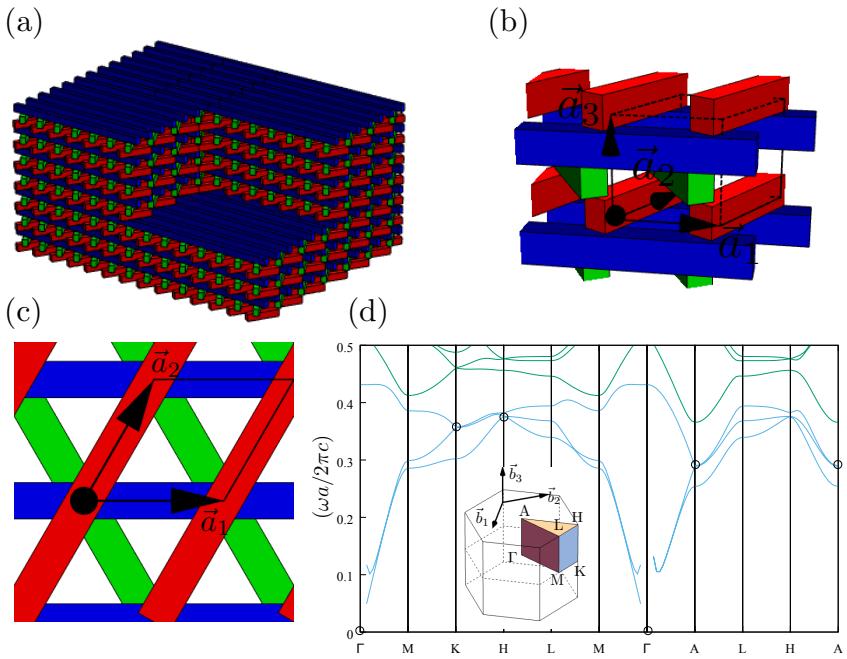

Figure 5.10: (a)A schematic of the $\pi/3$ chiral woodpile structure. Three independent layers are distinguished by colors(red, blue and green). (b) The unit cell of the periodic structure. (c)A top view of the structure. (d) The photonic band structure. The lowest three bands are made distinct with color. The Weyl points in the lowest three bands are enclosed by circles.

As obvious from Takahashi's explanation [88], it is the screw symmetry of the structure that is essential for the circular dichroism. On the other hand, the screw symmetry always accompanies Weyl points in its

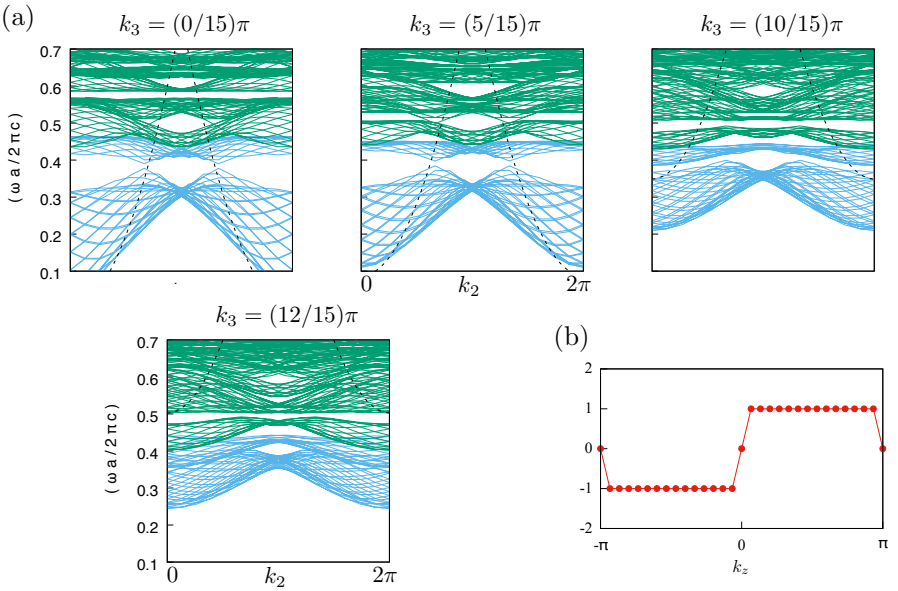

Figure 5.11: (a) Two dimensional photonic band structures on several k_z slices. The lowest three bands are distinguished by blue colors. The light cone are indicated by the broken line. (b) The section Chern number of the total of the lowest two bands as a function of k_z.

band structure. For lines parallel to the screw axis and that are invariant under the rotation part of the screw transformation, the fractional translation is also allowed. Due to the fractional translation, the dispersion curve on the line is folded and it necessarily produces crossing points. More detailed discussion is given in the later7.1. Getting off the line, the crossing is solved and the degeneracy is a Weyl point in the 3D Brillouin zone. Therefore, chiral woodpile structures having a screw symmetry is expected to accompany the Weyl point in its band structure.

The $\pi/3$ chiral woodpile photonic crystal

First, we take the $\pi/3$ chiral woodpile photonic crystal as studied in the subsection of circular dichroism(the schematic is shown in Fig. 5.10). The topview of the structue(crossing points between rods) forms a triangular lattice. We assume the width of each rod to be 130 nm, inter-spacing between adjacent rods(the lattice constant) to be $a = 500$ nm and the thickness of each layer to be $500/3$ nm. In this thickness of the rod, the unit length in the stacking direction equals to the lattice length in the in-plane direction. Also, we assume the refractive index to be that of GaAs, $n = 3.4$.

The bulk photonic band structure for the setup is shown in Fig. 5.10 (d). The most prominent Weyl point here is found between the 2nd and 3rd bands at the K point. Since the lines parallel to the staking axis(the $z-$ axis) passing through the K, K' or Γ point have the $a/3$ fractional translation symmetry in the stacking direction, dispersion curves along those lines are folded into $1/3$. Then, each of them has one Weyl point between the 2nd and 3rd bands and another Weyl point between the 1st and 2nd bands. Since the structure has the same point group symmetry as that of the helical honeycomb photonic crystal, those Weyl are explained by the group theory and conversely, the Weyl points in the helical photonic crystal are also explained by the screw symmetry.

If we can fix the k_z from incidence through sample propagation, we can focus on the 2D slice of the fixed k_z and photonic band structures on k_z slices are shown in Fig 5.11. Since Weyl points lies at K and K' points, two Dirac cones appear in the $k_z = 0$ slice. With the increas of k_z, the Dirac cones dissolve and the section Chern number of the gap is nonzero(Fig. 5.10(b)). The sum of the section Chern numbers $C(k_z)$ below the energy gap between the second and third bands changes from -1 to $+1$ at $k_z = 0$. The sudden change by $+2$ indicates two Weyl points with $+1$ charge at the K and K' point. When the spatial symmetry is reduced by modifying the rod width in one of the three semiconductor layers, the two Weyl points are separated in the opposite k_z directions and $C(k_z)$ gradually changes one by one as a function of k_z, as in the previous case of the honeycomb

array of spirals with different twists between sublattices. Note that the Weyl point must appear as a pair with ± 1 respective topological charges. In the present case, the other two Weyl points with -1 charge exist at the A point(on the line passing the Γ point). Since the A point is invariant under π rotation around the z-axis, two Weyl points pile up there and dispersion around it is quadratic. Then, the degeneracy points contributes by two to the section Chern number. Though Weyl points inevitably arise because of the screw symmetry, the section Chern number can be zero. In the present case, the dispersion curve on the line passing Γ and A points is opposite from that on the line passing K and H points, in the way that the 1st and 2nd(2nd and 3rd) bands cross at the Γ(A) point while they cross at the H(K) point. When those crossing occur at the same time in k_z, the section Chern number can not change from zero [91].

Due to the TRS, the slice dispersion at $-k_z$ is given by rotating the dispersion at k_z by π around z. The band gap in the k_z slice is largest at about $k_z \simeq= 2\pi/3$. This seems to be relevant to the resonant wave length of the circular dichroism. In addition, most part of the topological gap comes below the light cone, meaning the edge mode is bounded at interface without any artificial coatings.

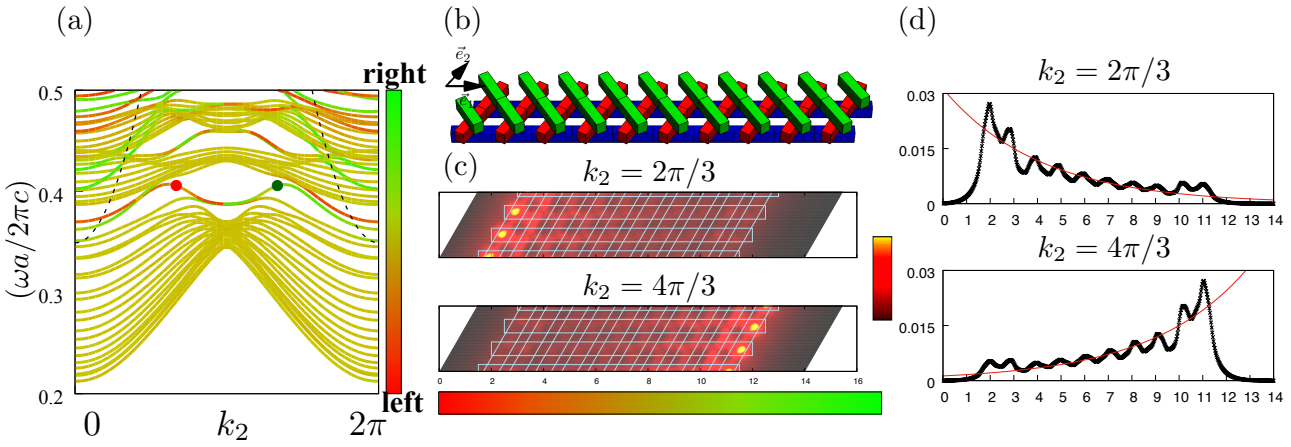

Figure 5.12: (a)Photonic band structure for fixed $k_z = 2\pi/3$ in the finite width geometry. The color of lines represents the intensity momentum of the eigenmode in the a_1 direction $\int \mathrm{d}^3 r \; a_1 |\vec{H}(\vec{r}|^2$. The dotted lines in the figure represents the light cone.)(b) The finite width geometry of Fig. (a). 10 times repetition of rod structures are taken, two unit cells are taken for air region for both sides and the vanishing boundary condition is taken. (c) The intensity profile ($|\vec{H}(\vec{r})|^2$)of the edge mode at $k_2 = 2\pi/3$ ($4\pi/3$), which is represented by the red(green) point in the Fig. (a). (d) The decay profile of the edge modes of Fig. (c), which is given by contracting intensity as $f(a_1) = \int \mathrm{d}r_2 \mathrm{d}r_3 |\vec{H}(\vec{r})|^2$. The profile of $k_2 = 2\pi/3 (k_2 = 4\pi/3)$ is fitted by the red line, $f(a_1) = c \exp(-(a/14)(x - (b/14))$ with $c = 1.92 \times 10^{-2} (1.92 \times 10^{-2})$, $a = 3.42(-3.44)$ and $b = 2(11)$.

Edge mode

In next, we examine the edge mode in the topologically non-trivial gap. To examine edge modes, we set finite width system of 9 unit cells in the $\vec{a}_1$ direction(Fig. 5.12(b)) with termination by air(empty) regions of 2(3) unit cells for the left(right) side. The boundary of the computational space is terminate by the vanishing boundary condition. In the $\vec{a}_2$ direction, the system is periodic and eigenfrequency spectrum is plotted to k_2. In Fig. 5.12(a), the frequency dispersion for $k_z = 2\pi/3$ is shown. Compared to the corresponding result in the Fig. 5.11, edge modes are seen in the bulk gap. The color of the lines represents which side of the system the edge mode is localized at, which is determined by the momentum of the intensity profile of the eigenstate in the $\vec{a}_1$ direction. The red(green) color means that the edge mode is localized at the left(right) edge.

The gap around $\omega a/2\pi c \approx 0.4$ has the Chern number of $+1$(Fig. 5.11). The edge modes appearing in the gap reflects the Chern number since the propagation direction of a wave packet(gradient of the dispersion) along interfaces is the counter-clockwise direction. Because of the TRS, the result in the $-k_z$ is given by inverting the result of k_z with respect to the k_2. Then the propagation direction of a wave packet is the clockwise direction in accordance with the Chern number. Propagation reflecting the edge modes of this property is well described

by a result of finite difference time domain(FDTD) simulation in the following.

Since edge modes are formed in the region below the light cone, it is confined at interface without any coating. Eigenmodes with color(red or green) in the Fig. 5.12(a) above the light cone extend in the air region. Whether topological edge modes come below the light cone or not depends on the type of termination.

Decay profiles of edge modes at $k_2 = 2\pi/3, 4\pi/3$ are shown in the Fig. 5.12(d). Because of the symmetry under the rotation by π around z, the result is symmetric with respect to $\pm k_2$. The decay profile is fitted to an exponential. The exponential is fitted in the region of the woodpile structure(discarding the air region) and the function is obtained by the Levenberg-Marquardt algorithm implemented in *gnuplot* [92]. However, the decay profile is not a smooth exponential function but has bumps. The bump reflects the woodpile structure. Eigenmodes tend to be localized in the dielectric region. The location of bumps in the Fig. 5.12 corresponds to the location of the red rods in the Fig. 5.12. Also, the intensity is stronger at interfaces.

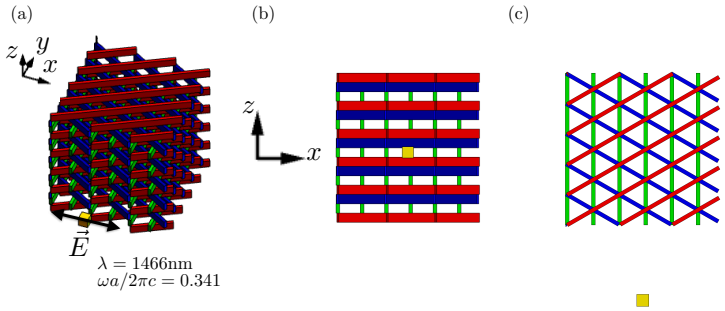

Figure 5.13: The setup for the FDTD simulation. (a)The entire configuration of the setup. A lump of the $\Pi/3$ chiral woodpile photonic crystal is put in air(vacuum). (The rectangular light source is shown by a yellow box. Incident light is generated with TE-polarization and the normalized frequency of $\omega a/2\pi c = 0.341$.(b)A front view of the configuration seen from the side of light source. The depth of the rods is taken to be 167 nm, the width to be 160 nm and the inter-spacing between rods is taken to be 500 nm.(c) A top view of the configuration.)

FDTD simulation

Finally, we examine the effect of the edge modes by the FDTD simulation. In one way, the effect of edge modes would be confirmed by an incidence of a pulse wave with the frequency of the corresponding gap and examining the spatial profile of the transmitted wave. Transmitted waves mostly have the wave number $k_y > 0$(Fig. 5.13(a)). If we choose the frequency of the incident wave to the frequency of the gap , the transmittance profile in the upper part is expected to be strong in the right side edge(Fig. 5.13(a),(b)) since waves propagating in the above direction mostly have the wave number of $k_z > 0$. On the other hand, the transmittance profile in the lower part is expected to be strong in the left side edge from the section Chern number(Fig. 5.11(b)) and the transmittance profile in the middle part is expected to be balanced between both sides.

In the simulation, we consider to induce a monochromatic light from a rectangular light source in front of the sample with the frequency center of the gap($\omega = 0.341$)[3] with the TE polarization(Fig. 5.13). Electric fields after reaching an equilibrium are shown in Figs. 5.14 and 5.15. Electric fields on the y slices are shown in Fig. 5.14. In the left side(Figs. 5.14(b),(d)) the amplitudes are stronger in the bottom part while in the right side(Figs. 5.14(c),(e)), they are stronger in the top. Moreover, electric fields on the z slices are shown in Fig. 5.15. In the top(Figs. 5.15(b)) the wave is directed to the right direction, while in the bottom(Figs. 5.14(c)), the wave is directed to the left. The obtained results are consistent with the expectation from the section Chern number and dispersion of edge modes.

[3]The size of the structure is little different from the previous subsection.

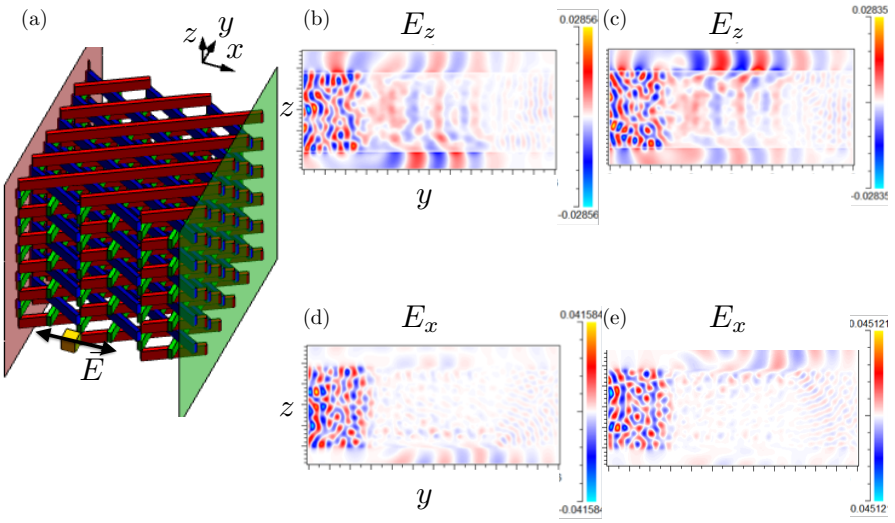

Figure 5.14: (a) Slices in both sides are shown by the colored planes with green and red for the right side and left side respectively. (b),(d) An amplitude profile in the left side(shown by the red plane in Fig. (a)) at a certain instant for E_z and E_x respectively.(c),(e) An amplitude profile in the right side(shown by the green plane in Fig. (a)) at a certain instant for E_z and E_x respectively.

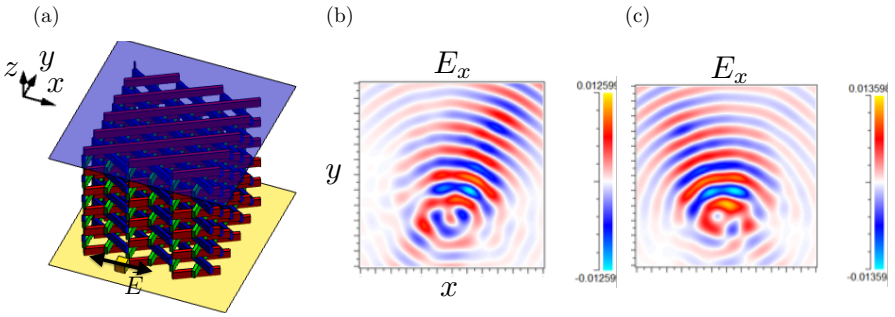

Figure 5.15: (a) Slices in top and bottoms are shown by the colored planes with purple and yellow for the top and bottom side respectively. (b)An amplitude profile in the top of the sample(shown by the purple plane in Fig. (a)) at a certain instant for E_z.(c)An amplitude profile in the bottom(shown by the yellow plane in Fig. (a)) at a certain instant for E_z.

5.4 Conclusion

In this chapter, the photonic crystal consisting of honeycomb array of helix-shaped holes in the dielectric material is analyzed. The edge modes along the spiral at surface of the photonic crystal are related to the section Chern number given in the 2D surface perpendicular to the uni-axis as the bulk-edge correspondence. The occurrences of the non-zero section Chern number is attributed to Weyl points lying in the $k_z = 0$(time reversal invariant) plane. Also we examined similar phenomena occurring in the chiral woodpile photonic crystal, which has a similar structural symmetry as the array of helices.

The chiral woodpile photonic crystal is already fabricated in tens of micrometers, which are suitable for integration to the currently existing electrical/optical systems. In the very same sample, circular dichroism has already been observed. Then, the studied topological edge modes also will be experimentally observed.

Chapter 6

Analogy between temporal and spatial modulation

In the former part of this chapter, our interest is placed on the similarities between temporal periodic modulation and spatial periodic modulation. Under periodic temporal modulation $H_{\text{ext}}(t+T) = H_{\text{ext}}(t)$, the energy of the system is no more conserved quantity. However the periodicity in the temporal modulation guarantees the conservation of the quasi-energy, which is the analog of the quasi-momentum(Bloch momentum) in spatial periodicity, and the steady states are given by the Floquet states satisfying $|\psi(t+T)\rangle = \mathrm{e}^{-\mathrm{i}\omega T}|\psi(t)\rangle$.

Oka and Aoki [93] showed that a strong laser field with circular polarization on graphene opens a gap in the dirac cone dispersion and induce topologically non-trivial band structure for the quasi energy dispersion of the floquet mode. This is the first proposal of the floquet topological insulator. Further, the floquet state in the model is studied in the effective hamiltonian method by Kitagawa *et al.* and the phase pattern for the "one photon assisted" hoppings is shown to be same as the phase pattern of the next nearest hoppings in the alternate fluxes of Haldane's honeycomb lattice. As described in the Sec. 3.4, the paraxial equation for the evanescently coupled wave guides takes the same form as the Shrodinger equation of a discrete lattice with the spatial coordinate in the propagation direction being the temporal coordinate instead. Rechtsman *et al.* made an honeycomb array of spiral wave guides([83]), and the paraxial equation in this case takes the same form as the system of graphene under circularly polarized laser field considered by Oka and Aoki. On the other hand, the honeycomb array of the helical dielectric waveguides almost has a same structure as the uniaxial chiral photonic crystal described in the previous chapter(5.2.1), where the localized propagation modes are ascribed to the existence of Weyl points in the three-dimensional band structure. This fact urges us to consider about the similarity between the temporal and the spatial modulation. We compare the two view points and relate the one side of the result to the other side. Also, we will show a simple tight-biding model of a stacked honeycomb lattice with slight modulation in the stacking are also mapped to the Haldane's honeycomb model and effectively to the Oka and Aoki's system, meaning the effect of spatial modulation can be regarded as a temporal modulation.

Though, the paraxial equation of the honeycomb array of evanescently coupled spiral waveguides are mapped to the Floquet topological insulator in one way, the derivation of the paraxial equation includes several simplifications, which are uncertain in the curved waveguide, and might be different from purely temporary varying systems. In the later part of this section, we consider floquet modes in purely time varying photonic crystals. The results are almost expectable without analysis. Further actual implementation seems to be unreasonable for photonic systems since delay of temporal modulation in space is comparable with dynamic scale of photonic modes. However, the same argument is applicable to other continuous classical systems such as elastic systems and it can be advantage since mapping of paraxial equation to the Schrodinger equation is unique to the optical wave guide and retardation can be negligible in elastic systems.

This chapter is structured as follows. In the first section, we begin with describing two approaches for Floquet mode analysis. One way is the wave expansion method, that is, expansion of the Hilbert space to the Sambe space [94] and the other way is the effective hamiltonian method. In the next section, we describe the Floquet topological insulator and show the paraxial equation in the honeycomb array of evanescently coupled spiral wave guides are mapped to the Oka and Aoki's graphene system. Further, we compare the floquet

mode analysis to the evanescently coupled wave guides to the three dimensional band structure analysis of the uniaxially anisotropic chiral photonic crystal. In the third section, we take a simple tight binding model of a stacked honeycomb lattice with modulation in the stacking direction and relate the effective hamiltonian in perturbation to the Haldane's honeycomb model. In the fourth section, we consider floquet modes in time varying photonic crystals. First, we describe the procedure for obtaining the Floquet modes in photonic crystals. Then we analyze, the floquet band structure and topological edge modes induced by time varying effects.

6.1 Wave expansion and effective hamiltonian methods for temporally varying systems

Wave expansion method(Floquet modes expansion)

When a time varying hamiltonian is periodic in time with period T

$$\hat{H}(t+T) = \hat{H}(t)\,, \tag{6.1}$$

similarly to the spatially periodic case, the eigenstates are given by floquet modes satisfying,

$$|\Psi_\omega(t+T)\rangle = \mathrm{e}^{-\mathrm{i}\omega T}|\Psi_\omega(t)\rangle. \tag{6.2}$$

Here, ω is the quasi frequency(eigenvalue) and it spans between $0 \le \omega < \Omega \quad (\Omega = 2\pi/T)$. It is appropreate, as in the case of the Bloch state, to denote the floquet mode $|\Psi_\omega(t)$ as

$$|\Psi_\omega(t)\rangle = \mathrm{e}^{-\mathrm{i}\omega t}|\psi_\omega(t)\rangle, \tag{6.3}$$

where $|\psi_\omega(t)\rangle$ is a temporally periodic state

$$|\psi_\omega(t+T)\rangle = |\psi_\omega(t)\rangle. \tag{6.4}$$

By substituting the floquet mode into the time dependent Schrodinger equation, we obtaine the floquet mode equation

$$\begin{aligned}\hat{H}(t)\,|\Psi_\omega(t)\rangle &= \mathrm{i}\hbar\frac{\partial}{\partial t}|\Psi_\omega(t)\rangle = \hbar\omega|\Psi_\omega(t)\rangle + \mathrm{i}\hbar\,\mathrm{e}^{\mathrm{i}\omega t}\frac{\partial}{\partial t}|\psi_\omega(t)\rangle \\ \hat{H}|\psi_\omega(t)\rangle &= \left(\hbar\omega + \mathrm{i}\hbar\frac{\partial}{\partial t}\right)|\psi_\omega(t)\rangle.\end{aligned} \tag{6.5}$$

One of the choices for expanding the floquet mode is the planewave expansion [94, 95]

$$|\Psi_\omega(t)\rangle = \mathrm{e}^{-\mathrm{i}\omega t}\sum_m |\psi_m(t)\rangle = \sum_{m,i} c_{m,i}\mathrm{e}^{-\mathrm{i}(\omega+m\Omega)t}|\phi_i\rangle. \tag{6.6}$$

Also we take a fourier transformation of $\hat{H}(t)$

$$\hat{H}(t) = \mathrm{e}^{-\mathrm{i}m\Omega t}\hat{H}_m. \tag{6.7}$$

By taking the inner product from the both hands of the Eq. (6.5),

$$\begin{aligned}\sum_{m,j} c_{m,j}\langle\langle\phi_i\mathrm{e}^{\mathrm{i}(\omega+\Omega_n)t}|\hat{H}|\phi_j\mathrm{e}^{-\mathrm{i}(\omega+\Omega_m)t}\rangle\rangle &= \sum_{m,j} c_{m,j}\hbar\,(\omega+m\Omega)\,\langle\langle\phi_i\mathrm{e}^{\mathrm{i}(\omega+\Omega_n)t}|\phi_j\mathrm{e}^{-\mathrm{i}(\omega+\Omega_m)t}\rangle\rangle \\ \sum_{m,j} c_{m,j}\langle\phi_i|H_{n-m}|\phi_j\rangle &= \hbar\,(\omega+m\Omega)\,\delta_{nm}\delta_{ij}\end{aligned} \tag{6.8}$$

$$\tag{6.9}$$

Here, we donote the total inner product as $\langle\langle\phi(t)\,|\psi(t)\rangle\rangle = \int_0^T \mathrm{d}t\,\langle\phi|\psi\rangle = \int_0^T \mathrm{d}t\int \mathrm{d}^3r\phi^*(\boldsymbol{r},t)\,\psi(\boldsymbol{r},t)$, and spatial inner product only as $\langle\phi|\psi\rangle$.

Thus the floquet mode equation for planewave expansion sattisfies

$$\sum_{m,j}\langle\phi_i|\hat{H}_{n-m}|\phi_j\rangle c_{m,j} = \hbar\left(\omega + m\Omega\right)c_{n,i}. \tag{6.10}$$

By diagonalizing the entire matrix, we obtain a quasi energy as an eigenvalue and floquet mode correspoinding to it. Note that the fourier transformed hamiltonian in the left hand side of the eigenequation is invariant against translation, and thus the spectrum of eigenvalue appears as periodic pattern. Thus all the information falls into the limited range of width Ω.

Effective hamiltonian approach

Using the evolution operator $\hat{U}(t, t_0)$, time evolution of the state $|\Psi(t)\rangle$ is written as

$$|\Psi(t)\rangle = \hat{U}(t, t_0)\,|\Psi(t_0)\rangle. \tag{6.11}$$

The evolution operator sattisfies the Schrodinger equation

$$\mathrm{i}\hbar\frac{\partial}{\partial t}\hat{U}(t, t_0) = \hat{H}(t)\,\hat{U}(t, t_0) \tag{6.12}$$

and it is given using the time dependent periodic hamiltonian $\hat{H}(t)$ as

$$\hat{U}(t) = \mathcal{T}\exp\left[-\frac{\mathrm{i}}{\hbar}\int_0^t \mathrm{d}t'\;\hat{H}(t)\right], \tag{6.13}$$

where $\mathcal{T}$ means taking the $T-$ordered product. Obviously, if the $\hat{H}(t)$ is always herimitian, the $\hat{U}(t, t_0)$ is unitary. It sattisfies the fundamental relations for an evolution operator

$$\hat{U}(t, t) = \hat{1}, \qquad \hat{U}(t_2, t_1)\,\hat{U}(t_1, t_0) = \hat{U}(t_2, t_0)\,. \tag{6.14}$$

For the temporaly periodic hamiltonian $\hat{H}(t + T) = \hat{H}(t)$, the evolution eperator sattisfies the relations

$$\hat{U}(t + T, T) = \hat{U}(t, 0)\,, \qquad \hat{U}(t + T, 0) = \hat{U}(t, 0)\,\hat{U}(T, 0)\,. \tag{6.15}$$

Using these relations, we obtain

$$\hat{U}(nT, 0) = \left[\hat{U}(T, 0)\right]^n, \tag{6.16}$$

with the n being an integer. In a long time scale $t = nt + \delta t, nt >> \delta t$, the time evolution is well given by the $\hat{U}^n(T)$. The effective hamiltonian is introduced as a static hamiltonian giving the $U(T)$

$$U(T, 0) = \mathcal{T}\exp\left[-\frac{\mathrm{i}}{\hbar}\int_0^T \mathrm{d}t'\;\hat{H}(t')\right] \equiv \exp\left(-\frac{\mathrm{i}}{\hbar}H_{\mathrm{eff}}T\right). \tag{6.17}$$

6.2 The floquet topological insulator in evanescently coupled twisted wave guides

A temporary periodic modulation can introduce a TRS breaking effect even if an instantaneous hamiltonian has TRS at any time. As first shown by Oka and Aoki in 2009 [93], application of an intense laser field with circular polarization to a two-dimensional dirac electron system cause a TRS breaking effect and opens a gap in the Dirac cone dispersion. The effective TRS breaking is caused by the circular polarization. The gap does not open in the case of linear polarization[1]. In the laser field, an electron interacts mainly with the electric field of the laser and the magnetic field is negligible. The electric field appears as the vector potential satisfying $\partial/\partial t\boldsymbol{A}(t) = \boldsymbol{E}(t)$. The hamiltonian for a two dimensional mass less dirac electron becomes

$$\mathcal{H} = \tau v\left(k_x + A_x\right)\sigma_x + v\left(k_y + A_y\right)\sigma_y. \tag{6.18}$$

[1]The gap at $\omega = \pm\Omega/2$ open also for linear polarization because of the broken continuous time translation symmetry.

Here, $\boldsymbol{\sigma}$ are pauli matrices, v is a velocity of the Dirac particle and τ is its chirality. In the hamiltonian, the vector potential appears as

$$\begin{pmatrix} 0 & A\tau e^{-i\tau\Omega t} \\ A\tau e^{i\tau\Omega t} & 0 \end{pmatrix}. \tag{6.19}$$

The velocity v can be incorporated into the intensity A^2. Thus, we set it as $v = 1$. The vector potential varies in time as

$$\Big(A_x(t)\,, A_y(t)\Big) = (A\cos(\Omega t), A\sin(\Omega t))\,. \tag{6.20}$$

Below we derive the floquet mode by the wave expansion method. The time invariant part of the hamiltonian is

$$\hat{H}_{mm} = \begin{pmatrix} 0 & k_x - ik_y \\ k_x + ik_y & 0 \end{pmatrix}, \tag{6.21}$$

and non-zero time dependent parts for $\tau = 1$ and $\tau = -1$are

$$\hat{H}_{m,m+1} = \begin{pmatrix} 0 & A \\ 0 & 0 \end{pmatrix}, \qquad \hat{H}_{m,m-1} = \begin{pmatrix} 0 & 0 \\ A & 0 \end{pmatrix}, \tag{6.22}$$

and

$$\hat{H}_{m,m+1} = \begin{pmatrix} 0 & 0 \\ -A & 0 \end{pmatrix}, \qquad \hat{H}_{m,m-1} = \begin{pmatrix} 0 & -A \\ 0 & 0 \end{pmatrix}, \tag{6.23}$$

respectively. The floquet mode band structure is obtained by the diagonalizing the equation (6.10). Since the induced field is monochromatic in this case, the entire matrix $\hat{H}$ is the tridiagonal matrix of the 2×2 block matrix $\hat{H}_{m,m\pm1}$. In the numerical diagonalization, the matrix have to be truncated at certain m. The results of diagonalization are shown in Fig. 6.1. The dispersion is characterized by the ratio A/Ω.

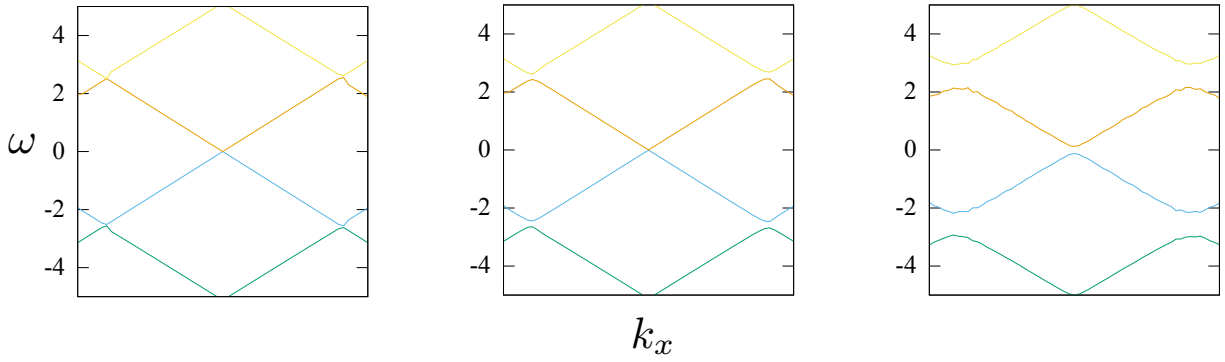

Figure 6.1: Dispersion along the intersection $k_y = 0$. The values are from left $A/\Omega = 0, 0.2, 0.8$ respectively.

The graphene also has two dirac cone dispersions at K and K' points in the Brillouin zone with the opposite chiralities. Since application of the intense laser field with circular polarization into the graphene opens gap in the dirac cones with the effective TRS breaking effect, the floquet band structure is topologically non-trivial. It is the first proposal of the floquet topological insulator [93]. Kitagawa *et al.* showed that the effective hamiltonian of the floquet topological insulator of the honeycomb model is same as that of the Haldane's honeycomb model [96]. In the tight-binding model, the vector potential is introduced by the Pierls approximation. Taking the $1/\Omega$ expansion to the first order [96], the effective hamiltonian reads

$$H_{\text{eff}} \simeq H_0 + \frac{[H_{-1}, H_1]}{\Omega} + O\Big(1/\Omega^2\Big), \tag{6.24}$$

and it becomes further near the K or K' point

$$H_{\text{eff}} \simeq v\Big(\sigma_y k_x - \sigma_x k_y \tau_z\Big) \pm \frac{v^2 A^2}{\Omega}\sigma_z\tau_z + O\Big(1/\Omega^2\Big). \tag{6.25}$$

[2]Therefore, for the same intensity, larger v is more sensitive to the effect.

Here the A is proportional to the laser intensity and H_n is the $n-$th fourier coefficient of the time-dependent hamiltonian. The modification of the hamiltonian with respect to the static case is the second term in the Eq. (6.25). This term comes from the sum of two second order processes, the one $H_1 \frac{1}{\omega-(\omega+\Omega)} H_{-1}$ where electron absorbs a photon and then emits a photon, and another $H_{-1} \frac{1}{\omega-(\omega-\Omega)} H_1$ where electron emits a photon and absorbs a photon. These processes forms the one-photon assisted next nearest hoppings with the same phase pattern with the Haldane's honeycomb model.

If time dependence of the hamiltonian can be taken to be symmetric with respect to an arbitrary time t_0, $\hat{T}\hat{H}(-t+t_0)\hat{T}^{-1} = \hat{H}(t+t_0)$, it is time-reversal symmetric in the level of the effective static hamiltonian [97]. Though emergence of a topologically non-trivial band structure is expected when a band degeneracy is solved by a TRS breaking effect, in certain cases, existence of a combinational symmetry with a spatial rotation can protect the degeneracy [98].

6.2.1 Floquet topological insulator in the evanescently coupled wave guides

As mentioned in the chapter 4, the paraxial equation for the two-dimensional array of wave guides takes the same form as the two-dimensional Schrodinger equation regarding the propagation coordinate as the temporal coordinate

$$\mathrm{i}\nabla_z \psi(x,y,z) = \left\{ -\frac{1}{2k_0}\nabla_\perp^2 - k_0 \frac{\delta n}{n_0} \right\} \psi(x,y,z)\,. \tag{6.26}$$

Here the $\psi(x,y,z)$ is the envelope function and the actual electric field is given by $\vec{E}(x,y,z) = \vec{e}_x \mathrm{e}^{\mathrm{i}k_0 z}\psi(x,y,z)$. The frequency of the electric field is given by $\omega = ck_0/n$, where the n is the refractive index of the background medium. The $\delta n(x,y,z)$ is the local difference of the refractive index from the background one and plays the role of the external potential in the Schrodinger equation. As shown in the Chapter 4, if we make the honeycomb pattern of the different spot of δn, the band structure resembling to that of graphene appears.

Then the deformation of a straight waveguide into a curved wave guide means an explicit temporal modulation of the Schrodinger equation. Rechtsmann *et al.* considered to twist each of waveguides of the honeycomb array to form a helix, and they found it cause the same effect as the circularly polarized laser field. This can be well seen by taking a reference coordinate where the $x-y$ slice plane is invariant

$$(x', y', z') = (x + R\cos(\Omega z)\,, y + R\sin(\Omega z)\,, z)\,, \tag{6.27}$$

where the R is the radius of the helix and the $\Omega = 2\pi/L$ and the L is the pitch of the helix in the unit twist. In the reference coordinate, the paraxial equation becomes

$$\mathrm{i}\partial_{z'}\psi(x',y',z') = \left\{ -\frac{1}{2k_0}\left(\nabla_\perp + \mathrm{i}\vec{A}(z')\right)^2 - \frac{k_0 R^2\Omega^2}{2} - \frac{k_0\delta n(x',y')}{n_0} \right\} \psi(x',y',z')\,, \tag{6.28}$$

where the $\vec{A}(z,) = k_0 R\Omega\,(\sin(\Omega z)\,, -\cos(\Omega z))$ is equivalent to the vector potential in the circularly polarized laser field. Then, it is obvious that the deformation of the straight waveguide into the helix opens a gap in the dirac cone dispersion in the honeycomb array of the waveguides and the band structure becomes topologically non-trivial.

6.2.2 Stacked honeycomb model and Haldane's honeycomb model

In the previous section, we discussed the equivalence between the floquet topological insulator of the honeycomb lattice under ac magnetic field and the evanescently coupled twisted wave guides and also mention that the coupled twisted wave guides are essentially same situation as pseudo two dimensional chiral photonic crystal discussed in the sec. 5.2.1.

In this section, we attempt to mimic the pseudo two dimensional chiral photonic crystal by a simple tight-binding model and derive the effective TRS breaking effect for finite k_z. According to the hollow location, we take a honeycomb lattice as a two dimensional basis and stack it in the $z-$direction. Within the plane, we assume only the nearest neighbor coupling t_1 and also assume the vertical hopping t_2 in the stacking direction. To introduce the effect of twisting, we distinguish the each of three layers and displace the second and third layers in the direction of the nearest neighbor link to form the $2\pi/3$ screw symmetry. As a result, we take the

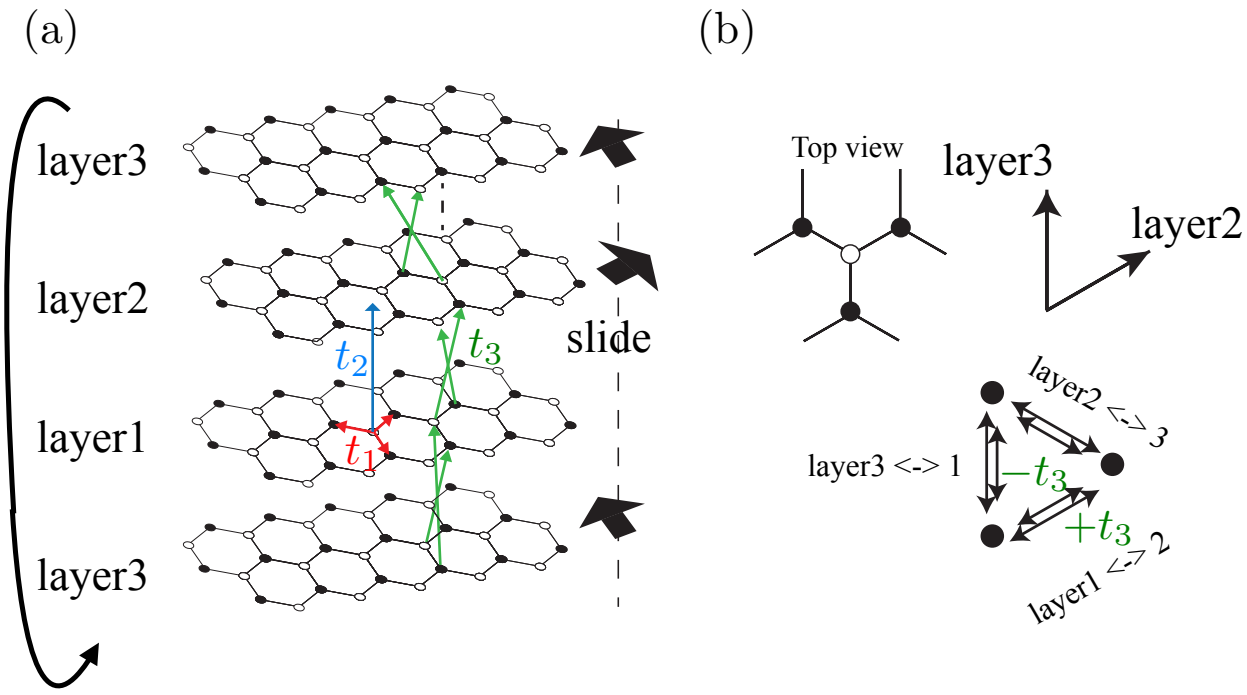

Figure 6.2: The tight-binding model of the stacked honeycomb lattice with the twisting displacement.(a) The links of the nearest neighbor hoppingt_1, the vertical hopping t_2 and the oblique hopping t_3 are shown. The second and third layers are displaced in the direction of the bold arrow.(b) The upper right figure shows the direction of the displacement for each layer. The bottom figure shows the relative displacement between adjacent layers. It is chosen to be the direction of the nearest neighbor link.

additional oblique link t_3 between the closest points in the adjacent layers. Separating the effect of the twist, we write the tight-binding hamiltonian

$$\begin{aligned}\mathcal{H} &= \mathcal{H}_0 + \mathcal{H}' \\ \mathcal{H}_0 &= \sum_{\langle i,j\rangle}\sum_k t_1 c^\dagger_{\bullet,i,k} c_{\circ,j,k} + \sum_{\circ,\bullet}\sum_i\sum_k c^\dagger_{\sigma,i,k+1} c_{\sigma,i,k} + h.c. \\ \mathcal{H}' &= \sum_{i,k}\left[-t_3 c^\dagger_{\bullet,i+\vec{\mu}(k),k+1} c_{\circ,i,k} + t_3 c^\dagger_{\circ,i-\vec{\mu}(k),k+1} c_{\bullet,i,k}\right] + h.c,\end{aligned} \tag{6.29}$$

where the $\vec{\mu}(k)$ is defined for each layer according to the displacement as

$$\vec{\mu}(1) = (0,0)\,, \quad \vec{\mu}(2) = (-1,0)\,, \quad \vec{\mu}(3) = (0,-1) \tag{6.30}$$

in the basis vector of the triangular lattice. Note that the sign difference in the hopping terms of $\mathcal{H}'$. This is because the oblique link in the ascending direction $\circ \to \bullet$ gets closer while the link $\circ \to \bullet$ goes away(Fig. 6.2). Without the perturbation $\mathcal{H}'$, they are just three copies of the honeycomb lattice and different only by the energy shifts due to kinetic energy in the $z-$direction given by $2t_2\cos(k_z + 2\pi i/3)$ $(i = 0,1,2)$. Taking the t_2 as the minus value, in $k_z = 0$, the lowest two bands are separated from the other four bands and the double degeneracy(Dirac cone dispersion) occurs at K or K' point. we consider to solve the degeneracy with the perturbation $\mathcal{H}'$ for $k_z \neq 0$.

Without the perturbation, the eigenstates are also eigenstates of the p_z. It is convenient to take the basis states as

$$|\psi^\alpha_{\sigma,i}\rangle = \sum_k e^{ik_z k}\left\{c^\dagger_{\sigma,i,0+3k} + \omega_\alpha e^{ik_z/3} c^\dagger_{\sigma,i,1+3k} + \omega_\alpha^2 e^{i2k_z/3} c^\dagger_{\sigma,i,2+3k}\right\}|0\rangle, \quad \alpha = 0,1,2 \tag{6.31}$$

where the ω_α is the cubic root and the k is the unit cell index in the $z-$direction. The first order perturbation for the lowest two bands $\langle\psi^0|\mathcal{H}'|\psi^0\rangle$ just adds the t_1 and does not solve the double degeneracy. Then next, we consider the second order perturbation for the lowest two bands

$$\mathcal{H}_{\text{eff}} = \sum_\sigma \sum_{\alpha=1,2} \frac{\mathcal{H}'|\psi^\alpha_\sigma\rangle\langle\psi^\alpha_\sigma|\mathcal{H}'}{E_0 - E_i}. \tag{6.32}$$

Since the matrix element intervenes one intermediate state, the oblique hopping takes place twice and does not change the sub-lattice in the end. The total pass is classified to two types. One is the round trip type, which ends in the initial position and it just gives a constant diagonal term. The phase of the intermediate state is irrelevant since $\omega_\alpha\omega^*_\alpha = 1$. The other type moves it to the next adjacent layer and the next nearest in-plane position. This type accompanies the phase factor in the $z-$ direction as $e^{i\pm 2k_z/3}$ due to two layers hopping. The type of link is determined by specifying the start layer and the end layer since only one link is allowed between adjacent layers. Then, there are six terms for each sub-lattice and they correspond to the six in-plane next nearest hopping. They are different in the phase factor and the strength is given by $\tilde{t} = -t_2^2\left(\frac{1}{E_0-E_1} + \frac{1}{E_0-E_2}\right) \simeq -\frac{2t_2^2}{3t_3}$ The phase factor is determined as shown in the Fig. 6.3. The phase factor is same for each three directions related by the $2\pi/3$ rotation and the two are opposite in the sign and the pattern is opposite for the sub-lattice. Then, the tight-binding model of the stacked honeycomb lattice is effectively mapped the Haldane's honeycomb model. The effective magnetic flux here is induced by the Bloch phase factor in the z direction.

This result is quite predictable. As in the work by Kitagawa *et al.*, the effective hamiltonian of the floquet topological insulator of the honeycomb lattice is mapped to the Haldane's honeycomb lattice. In addition, the twisted pseudo dimensional chiral photonic crystal is mapped to the honeycomb floquet topological insulator as the evanescently coupled twisted waveguides. Then it is natural to expect that a pseudo two dimensional system with the spatial modulation in the stacking direction is related to the two dimensional chern insulator such as the Haldane's honeycomb model.

6.3 The Floquet mode in a time varying photonic crystal

In this section, we consider the Floquet modes of EM waves in time varying photonic crystals. Though the Floquet modes expansion is almost same as before, the procedure is a little bit different because of the formal

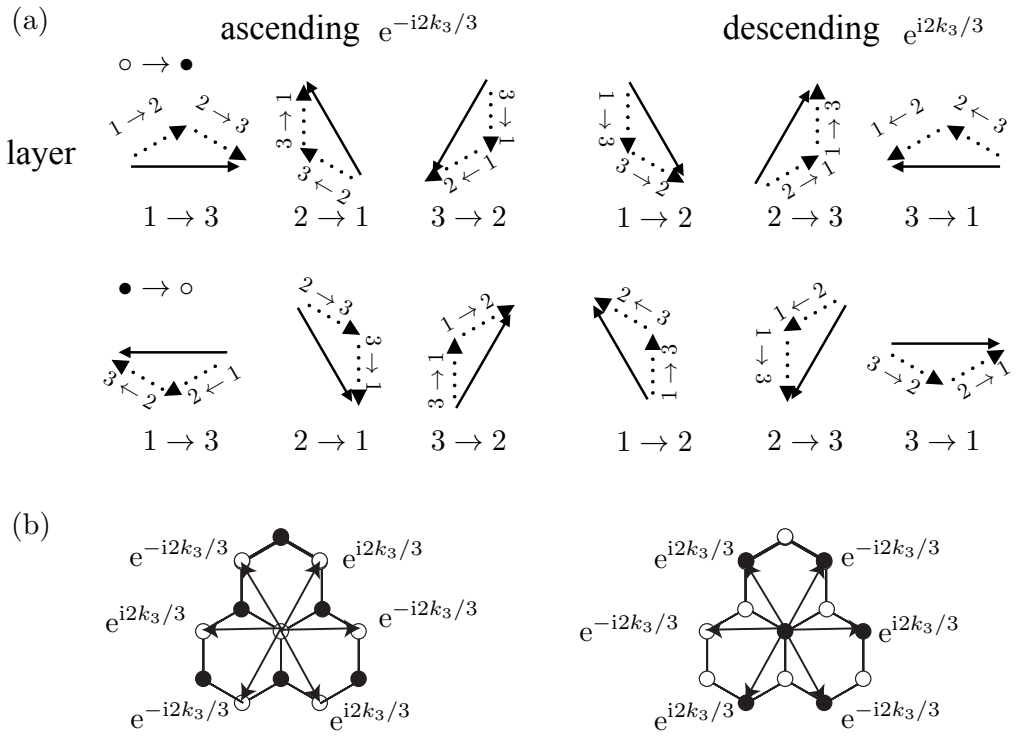

Figure 6.3: (a) All of the 12 terms contributing to the effective hamiltonian, which consist of two sequential oblique hopping, are listed. (b) The effective hopping links between next nearest in-plane points with the phase factors due to the oblique hopping, the pattern of which is same as that in the Haldane's honeycomb lattice.

deference between the Maxwell equations and the Schrödinger equation. In Maxwell equations for EM waves, the time evolution is given by

$$\begin{pmatrix} 0 & \nabla\times \\ -\nabla\times & 0 \end{pmatrix}\begin{pmatrix} \boldsymbol{E} \\ \boldsymbol{H} \end{pmatrix} = \frac{\partial}{\partial t}\begin{pmatrix} \hat{\varepsilon} & 0 \\ 0 & \hat{\mu} \end{pmatrix}\begin{pmatrix} \boldsymbol{E} \\ \boldsymbol{H}. \end{pmatrix} \tag{6.33}$$

Since the permittivity $\hat{\varepsilon}(\boldsymbol{t})$ and the permeability $\hat{\mu}(\boldsymbol{t})$ play the same role as the external potential in the Schrödinger equation, if they do not vary in time, the system is invariant to time translation and a solution is given by harmonic modes

$$\begin{pmatrix} \boldsymbol{E}(t) \\ \boldsymbol{H}(t) \end{pmatrix} = e^{-i\omega t}\begin{pmatrix} \boldsymbol{E} \\ \boldsymbol{H} \end{pmatrix}. \tag{6.34}$$

Thus, the equation is reduced to

$$\begin{pmatrix} 0 & i\nabla\times \\ -i\nabla\times & 0 \end{pmatrix}\begin{pmatrix} \boldsymbol{E} \\ \boldsymbol{H} \end{pmatrix} = \omega\begin{pmatrix} \hat{\varepsilon} & 0 \\ 0 & \hat{\mu} \end{pmatrix}\begin{pmatrix} \boldsymbol{E} \\ \boldsymbol{H}. \end{pmatrix} \tag{6.35}$$

In this form, the equation is further simplified to the equation with respect to either $\boldsymbol{E}$ or $\boldsymbol{H}$,

$$\nabla \times \varepsilon^{-1}\nabla \times \boldsymbol{H} = \omega^2\mu\boldsymbol{H}.$$

If the system varies periodically in time $\{\hat{\varepsilon}(t+T), \hat{\mu}(t+T)\} = \{\hat{\varepsilon}(t), \hat{\mu}(t)\}$, the system is invariant under the time translation with the period T and the solutions are given by floquet modes, which satisfies

$$\begin{pmatrix} \boldsymbol{E}(t+T) \\ \boldsymbol{H}(t+T) \end{pmatrix} = e^{-i\omega T}\begin{pmatrix} \boldsymbol{E}(t) \\ \boldsymbol{H}(t) \end{pmatrix}. \tag{6.36}$$

As before, the general form of the floquet modes is given by

$$\boldsymbol{\Psi}_\omega(t) = e^{-i\omega t}\boldsymbol{\psi}(t), \qquad \boldsymbol{\psi}(t+T) = \boldsymbol{\psi}(t), \tag{6.37}$$

where the $\vec{\psi}(t)$ has two component of the electric and magnetic fields. We expand the time periodic part with plane waves of period $2\pi m/T$

$$\boldsymbol{\Psi}(t) = \sum_m \mathrm{e}^{-\mathrm{i}(\Omega_m+\omega)t}\boldsymbol{\psi}_m \qquad \Omega_m = \frac{2\pi m}{T}, \tag{6.38}$$

By substituting the Eq. (6.38) into Eq. (6.33) it becomes,

$$\sum_m \begin{pmatrix} 0 & \mathrm{i}\nabla\times \\ -\mathrm{i}\nabla\times & 0 \end{pmatrix}\begin{pmatrix} \boldsymbol{E_m} \\ \boldsymbol{H_m} \end{pmatrix}\mathrm{e}^{-\mathrm{i}\Omega_m t} = \sum_m (\omega+\Omega_m)\begin{pmatrix} \hat{\varepsilon}(t) & 0 \\ 0 & \hat{\mu}(t) \end{pmatrix}\begin{pmatrix} \boldsymbol{E}_m \\ \boldsymbol{H}_m \end{pmatrix}\mathrm{e}^{-\mathrm{i}\Omega_m t} + \mathrm{i}\sum_m \begin{pmatrix} \frac{\partial}{\partial t}\hat{\varepsilon}(t) & 0 \\ 0 & \frac{\partial}{\partial t}\hat{\mu}(t) \end{pmatrix}\begin{pmatrix} \boldsymbol{E}_m \\ \boldsymbol{H}_m \end{pmatrix}\mathrm{e}^{-\mathrm{i}\Omega_m t}.$$

Since $\left[\hat{\varepsilon}(t)\,\mathrm{e}^{-\mathrm{i}\Omega_m t}\right]_{t=t_0}^{t=t_0+T} = 0$,

$$\int \mathrm{d}t\,(\frac{\partial}{\partial t}\hat{\varepsilon})\mathrm{e}^{\mathrm{i}\Omega_m t} = -\mathrm{i}\Omega_m \int \mathrm{d}t\;\hat{\varepsilon}\mathrm{e}^{\mathrm{i}\Omega_m t} = -\mathrm{i}\Omega_m\hat{\varepsilon}_m. \tag{6.39}$$

Multiplying the both hands by $\mathrm{e}^{\mathrm{i}\Omega_n t}$ and integrating $\int_0^T \mathrm{d}T$, we obtain

$$\begin{pmatrix} 0 & \mathrm{i}\nabla\times \\ -\mathrm{i}\nabla\times & 0 \end{pmatrix}\begin{pmatrix} \boldsymbol{E}_n \\ \boldsymbol{H}_n \end{pmatrix} = \sum_m (\omega+\Omega_n)\begin{pmatrix} \hat{\varepsilon}_{n-m} & 0 \\ 0 & \hat{\mu}_{n-m} \end{pmatrix}\begin{pmatrix} \boldsymbol{E}_m \\ \boldsymbol{H}_m \end{pmatrix},$$

where $\{\hat{\varepsilon}_n, \hat{\mu}_n\} = \frac{1}{T}\int \mathrm{d}t\;\mathrm{e}^{\mathrm{i}\Omega_n t}\{\hat{\varepsilon}(t), \hat{\mu}(t)\}$. The right hand of the equation consists of multiple frequency components, while the left hand side consists of single frequency component. Then the coefficients in the one hand side can not be divided simultaneously as in the expansion of the Schrödinger equation and thus the eigenequation does not reduce to the equation for single ($\boldsymbol{E}$ or $\boldsymbol{H}$). Also, the eigenequation is translationally invariant with respect to the suffix n, and then those components must be same $\{\boldsymbol{E}_{n+1}, \boldsymbol{H}_{n+1}\} = \{\boldsymbol{E}_n, \boldsymbol{H}_n\}$. This means that if ω is the eigenvalue, $\omega \to \omega + \Omega_k$ is also included in the eigenspectrum, that is, ω is periodic with the period $\Omega = 2\pi/T$, since the ω is quasi energy. To set the equation into the form of a general eigenvalue problem, we denote the equation as

$$\sum_m \begin{pmatrix} -\Omega_n\hat{\varepsilon}_{n-m} & \delta_{n,m}\mathrm{i}\nabla\times \\ -\delta_{nm}\mathrm{i}\nabla\times & -\Omega_n\hat{\mu}_{n-m} \end{pmatrix}\begin{pmatrix} \boldsymbol{E}_m \\ \boldsymbol{H}_m \end{pmatrix} = \omega\sum_m \begin{pmatrix} \hat{\varepsilon}_{n-m} & 0 \\ 0 & \hat{\mu}_{n-m} \end{pmatrix}\begin{pmatrix} \boldsymbol{E}_m \\ \boldsymbol{H}_m \end{pmatrix}. \tag{6.40}$$

Photonic floquet mode in gaussian expansion

In next, we consider to solve the eigenequation(Eq. 6.40) numerically using a hybrid gaussian basis set, which is localized in space and extends as a wave in the temporal direction[3]. We focus on 2-dimensional systems, where the EM modes are given by TE or TM modes. The TE mode, in a time invariant system, is expanded by gaussian bases as

$$\boldsymbol{E}(\boldsymbol{r}) = \sum_i \left\{c_i^{(2)}\boldsymbol{g}_i^{(2)}(\boldsymbol{r}) + c_i^{(3)}\boldsymbol{g}_i^{(3)}(\boldsymbol{r})\right\}, H_z(\boldsymbol{r}) = \sum_i c_i^{(3)} g_1^{(3)}(\boldsymbol{r}), \tag{6.41}$$

where, $\boldsymbol{g}_i^{(1)}(\boldsymbol{r})$, $\boldsymbol{g}_i^{(2)}(\boldsymbol{r})$ $g_i^{(3)}(\boldsymbol{r})$ are gaussian bases

$$\boldsymbol{g}_i^{(1)}(\boldsymbol{r}) = \begin{pmatrix} -(y-y_i) \\ (x-x_i) \end{pmatrix}\mathrm{e}^{-\alpha(\boldsymbol{r}-\boldsymbol{R}_i)^2}, \boldsymbol{g}_i^{(2)}(\boldsymbol{r}) = \begin{pmatrix} (x-x_i) \\ (y-y_i) \end{pmatrix}\mathrm{e}^{-\alpha(\boldsymbol{r}-\boldsymbol{R}_i)^2}, g_i^{(3)}(\boldsymbol{r}) = \mathrm{e}^{-\alpha(\boldsymbol{r}-\boldsymbol{R}_i)^2}, \tag{6.42}$$

and the time dependence is given by the plane waves of period T,

$$\boldsymbol{g}_{i,m}^{(1)}(\boldsymbol{r},t) = \mathrm{e}^{-\mathrm{i}\Omega_m t}\boldsymbol{g}_i^{(1)}(\boldsymbol{r}), \quad \boldsymbol{g}_{i,m}^{(2)}(\boldsymbol{r},t) = \mathrm{e}^{-\mathrm{i}\Omega_m t}\boldsymbol{g}_i^{(2)}(\boldsymbol{r}), \quad g_{i,m}^{(3)}(\boldsymbol{r},t) = \mathrm{e}^{-\mathrm{i}\Omega_m t}g_i^{(3)}(\boldsymbol{r}). \tag{6.43}$$

(6.44)

[3] A gaussian basis localized in both space and time can also be considered.

Referring to Eq.(6.40), we obtain the matrix eigenequation for gaussian bases as a generalized eigenvalue problem

$$\sum_m \hat{L}_{n,m}\boldsymbol{c}_m = \omega \sum_m \hat{R}_{n,m}\boldsymbol{c}_m, \tag{6.45}$$

where the $\vec{c}_m$ is the coefficient vector for a harmonic component

$$\boldsymbol{c} = \begin{pmatrix} \boldsymbol{c}_1 \\ \boldsymbol{c}_2 \\ \vdots \\ \boldsymbol{c}_m \\ \vdots \end{pmatrix}, \qquad \boldsymbol{c}_m = \begin{pmatrix} \vdots \\ c^{(1)}_{m,ij} \\ c^{(2)}_{m,ij} \\ c^{(3)}_{m,ij} \\ \vdots \end{pmatrix}. \tag{6.46}$$

The $\hat{L}_{n,m}$ denotes the block matrix in the left hand side of Eq. (6.40)

$$\hat{L}_{n,m} = \begin{pmatrix} -\Omega_n \hat{\varepsilon}^{(11)}_{n-m,ij} & -\Omega_n \hat{\varepsilon}^{(12)}_{n-m,ij} & -\mathrm{i}\delta_{n,m}\,(\nabla\times)^{(13)}_{ij} \\ -\Omega_n \hat{\varepsilon}^{(21)}_{n-m,ij} & -\Omega_n \hat{\varepsilon}^{(22)}_{n-m,ij} & 0 \\ \mathrm{i}\delta_{n,m}\,(\nabla\times)^{(31)}_{ij} & 0 & -\Omega_n \hat{\varepsilon}_{n-m,ij} \end{pmatrix}, \tag{6.47}$$

and the $\hat{R}_{n,m}$ denotes the block matrix in the right hand side of Eq. (6.40)

$$\hat{R}_{n,m} = \begin{pmatrix} \hat{\varepsilon}^{(11)}_{n-m,ij} & \hat{\varepsilon}^{(12)}_{n-m,ij} & 0 \\ \hat{\varepsilon}^{(21)}_{n-m,ij} & \hat{\varepsilon}^{(22)}_{n-m,ij} & 0 \\ 0 & 0 & \hat{\mu}_{n-m,ij} \end{pmatrix} \tag{6.48}$$

The matrix elements for rotation is

$$(\nabla\times)^{(ab)}_{ij} = \int \mathrm{d}^3 r\, \boldsymbol{g}^{(a)}_i(\boldsymbol{r}) \cdot \nabla \times \boldsymbol{g}^{(b)}_j(\boldsymbol{r})\,. \tag{6.49}$$

The rotation of the gaussian bases $\boldsymbol{g}^{(2)}_i$ is zero. Thus, the non zero elements are only $(\nabla\times)^{(13)}_{ij}$ and $(\nabla\times)^{(31)}_{ij}$.

$$(\nabla\times)^{(13)}_{ij} = \int \mathrm{d}^3 r\, \boldsymbol{g}^{(1)}_i(\boldsymbol{r}) \cdot \nabla \times \boldsymbol{g}^{(3)}_j(\boldsymbol{r}) = \sqrt{\frac{\pi}{2\alpha}}\mathrm{e}^{-\alpha r^2_{ij}}\left(1 - \frac{\alpha}{2} r^2_{ij}\right) \tag{6.50}$$

Further, $(\nabla\times)^{(31)}_{ij} = (\nabla\times)^{13}_{ji} = (\nabla\times)^{(13)}_{ij}$. The overlap $\hat{\varepsilon}^{(ab)}_{m.ij}$ ($\hat{\mu}^{(ab)}_{m,ij}$)is given by

$$\hat{\varepsilon}^{(ab)}_{m,ij} = \int \mathrm{d}^3 r\, \boldsymbol{g}^{(a)}_i(\boldsymbol{r}) \cdot \hat{\varepsilon}_m(\boldsymbol{r})\, \boldsymbol{g}^{(b)}_j(\boldsymbol{r})\,. \tag{6.51}$$

The fourier component of the potential $\hat{\varepsilon}_m(\boldsymbol{r})$ is obtained by fourier transforming the time variation of the potential for each position

$$\hat{\varepsilon}_m(\boldsymbol{r}) = \int_0^T \mathrm{d}t\, \mathrm{e}^{\mathrm{i}\Omega t}\hat{\varepsilon}(\boldsymbol{r}, t)\,. \tag{6.52}$$

The matrix elements for uniform potentials $\{\hat{\varepsilon}, \hat{\mu}\} = \{\varepsilon_0, \mu_0\}$ non zero matrix elements are given by

$$\hat{\varepsilon}^{(11)}_{0,ij} = \hat{\varepsilon}^{(22)}_{0,ij} = \left(\frac{\pi}{2\alpha}\right)\frac{1}{4\alpha}\left(2 - \alpha r^2_{ij}\right)\mathrm{e}^{-\alpha r^2_{ij}}, \qquad \hat{\mu}^{(33)}_{0,ij} = \frac{\pi}{2\alpha}\mathrm{e}^{-\alpha r^2_{ij}}. \tag{6.53}$$

Without truncation, the eigenvalue in the eigenequaion(Eq. 6.40) is periodic with the period $2\pi/T$ and it is the quasi energy. In the actual computation, the floquet component are truncated in a finite number of waves as plane waves truncation for Bloch states. This truncation is allowed since usually the fourier components of the potential converge to zero for higher frequency components. Using the method described above, we solve the Floquet mode equation(Eq. 6.40). First, let us consider to solve the eigenequation Eq. (6.40) for a static photonic crystal, for which we can get the eigenspectrum by the usual static eigenequation.

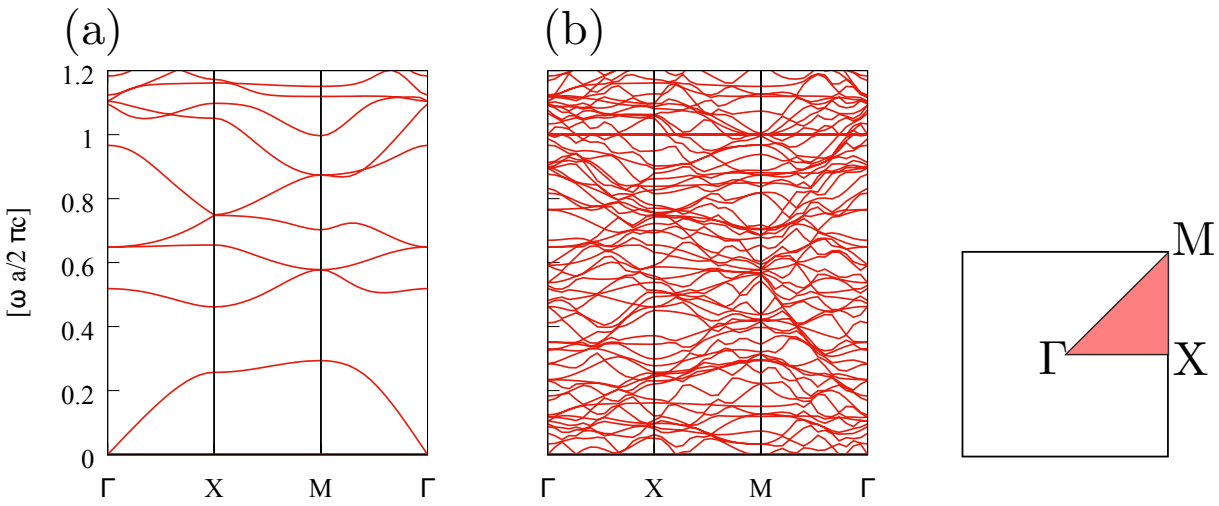

Figure 6.4: Comparison of obtained results by solving the stationary eigenequation(a) and the floquet mode eigenequation. In the floquet mode expansion the range of quasi energy spans between $0 < \omega a/2\pi c \leq 1$.

We consider a steady photonic crystal consisting of the square array of dielectric cylinders, with lattice constant $a = 1$, the radius of the cylinder $r = 0.15$ and the periodic length is set to $T = 1$. The obtained result is shown in figure Fig.6.4(b). As you can see, the figure is too messy to obtain any information. The graph is the repetition of same curves in the frequency axis. This is because reduction of the eigenfrequency to quasi frequency(floquet spectrum) discard the difference of the value with periodicity Ω_m and all the frequency bands are collected within a window (reduced zone). On the other hand, in a static and frequency conserving system, only modes having the same frequency as the injected waves excite in the system. Even if a system is under periodic temporal modulation, the fourier spectrum of the potential converge to zero in higher frequencies, the mode having frequencies quite apart from the injected waves does not seem to excite. Thus we can neglect those modes apart from the frequency of injecting waves and select only a few modes [99].

First, we choose a few of relevant modes $\left\{|\psi_1^0(\boldsymbol{k})\rangle, |\psi_2^0(\boldsymbol{k})\rangle, \cdots, |\psi_n^0(\boldsymbol{k})\rangle\right\}$from the solution of the static system, regarding the time modulation being perturbation. From the static solutions we compose the floquet modes as

$$|\psi_i^m(\boldsymbol{k})\rangle = \mathrm{e}^{-\mathrm{i}\Omega_m t}|\psi_i^0(\boldsymbol{k})\rangle = \sum_i c_{i,a}^m \mathrm{e}^{-\mathrm{i}\Omega_m t}|\boldsymbol{g}_i^{(a)}(\boldsymbol{k})\rangle. \tag{6.54}$$

Using these bases, we obtain reduced(projected) matrix as

$$\tilde{A} = \{|\psi_1\rangle, \psi_2\rangle \ldots, |\psi_m\rangle\}^\dagger A \{|\psi_1\rangle, \psi_2\rangle \ldots, |\psi_m\rangle\}. \tag{6.55}$$

Projecting the matrix in the Eq. (6.45), we can obtained Floquet mode solution coupled among selected modes by the dynamical effect. The validity is confirmed most simply by comparing the numerical solution in the 1D photonic crystal moving in one direction at constant speed with the analytic solution . The uniform motion of the dielectric structure cause the Doppler shift in the opposite amount for light propagating in the opposite direction.

Floquet band structure in moving photonic crystals

We consider to move the dielectric structure in space. This movement can be achieved by producing the spatial profile of the dielectric constant by inducing stimulating lights from both sides to arise a standing wave with large intensity on non-linear optical materials, and giving frequency difference between them [100]. A permanent frequency difference between two stimulating sources causes uniform motion and an oscillating frequency difference cause a oscillation of the spatial profile of the dielectric constant. Further if the frequency

oscillating of the sources are tuned to be different by $\pi/2$ in phase, the motion may become circulation of the profile around each central point.

Though both of the straight oscillation and circular motion induce the Floquet band structure, the former does not break the effective time-reversal symmetry, whereas the later does. In Fig. 6.6 we compare the results of the two types of motion of the spatial profile of the dielectric constant. The set up for the steady state is same as in the case of Fig. 6.4. Without temporal modulation, the TM mode band structure degenerate between the 2nd and 3rd bands($\omega a/2\pi c \approx 0.6$) at M point. We induce a temporal modulation with period $T = 6.0$ and amplitude $r_h = 0.06a$. In the case of circular motion, the degeneracy dissolves, whereas it remain closes in the case of the straight oscillation(Fig. 6.6). Further, we computed the Chern number in the gap and find that it takes -1 for the circular motion in the clockwise direction, whereas the value is converse in the case of counter-clockwise circulation. Note that computation of Chern number in this case requires an additional care because the eigenvector is given on the bases of projected modes. The selected bands are chosen by seeing the intensity decay of the fourier component. Since it sufficiently decays at the 2nd coefficient(see Fig. 6.7), it is reasonable to choose bands within the range of $\omega \approx 0.2$.

The Floquet mode band structure becomes topologically non trivial in the case of circular temporal modulation while it remains trivial in the case of the straight oscillation. Whether the Floquet band structure becomes topologically non-trivial or not depends on whether the temporal modulation is time-reversal symmetric with respect to an arbitrary point in time or not. The spatial profile of the first fourier component for the circular motion is shown in Fig. 6.7. It has the imaginary component, whereas the imaginary component vanishes for the straight oscillation.

Finally, the floquet mode dispersion for the clockwise circulating motion in a finite width system is analyzed. The system is periodic in the y direction, and 8 unit cells are taken in the x direction. First the steady eigenmodes are obtained by the static mode analysis in the geometry. Selected modes for the floquet mode analysis are chosen from the eigenmodes in the geometry. The result is shown in the Fig. 6.8. The edge mode in the topologically non-trivial gap is indicated by the red line. The edge mode profiles at two points are also shown in the Fig. 6.8 and we can see the edge modes agree unidirectional along the edge in the clockwise direction. This is the consequence of the bulk-edge correspondence according to the Chern number in the gap $\nu = -1$, and also it is consistent with the clockwise circulation of the dielectric constant profile.

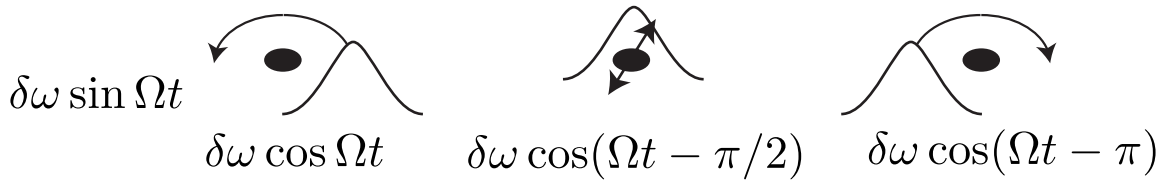

Figure 6.5: Motion of the spatial profile of the dielectric constant given by the frequency difference between stimulating sources. If the phase difference is $\pi/2$, each periodic profile circulates around each central point. If the phases are met, the spatial profile simply oscillates in one direction.

6.4 Conclusion

In this chapter, we first discussed similarity between the uni-axially chiral photonic crystal and the evanescently coupled twisted waveguides, where the edge modes are ascribed to the topological Floquet band structure. Those results are physically equivalent and the difference in the interpretation occurs according to which of, the wavenumber in the propagation direction or the frequency is taken as a spectrum. Subsequently, we attempted to form a photonic topological Floquet band structure in a truly time-varying 2D photonic crystal. Straighforward diagonalization of the Floquet mode hamiltonian in a continuous space produce a messy spectrum, from which

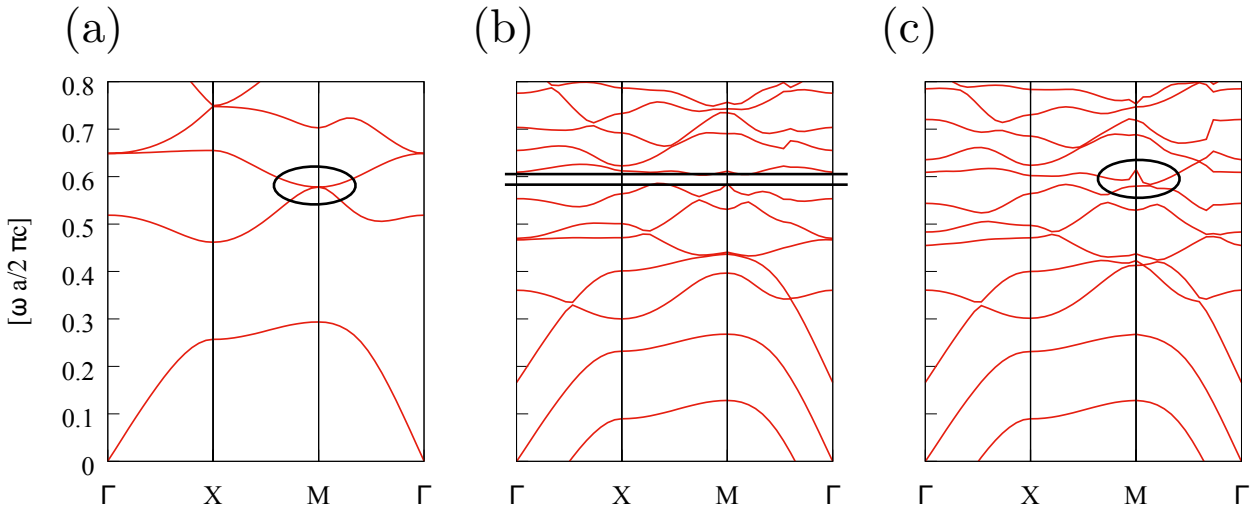

Figure 6.6: Steady photonic band structure of TM mode. The degeneracy between the 2nd and 3rd band is indicated by the circle. (b) The Floquet band structure for the circular motion of the spatial profile of the dielectric constant. The degeneracy is solved by the circular motion and the gap is distinctive by the two straight lines. (c) Floquet band structure in the case of the straight oscillation. The gap remains close(indicated by the circle) for the motion.

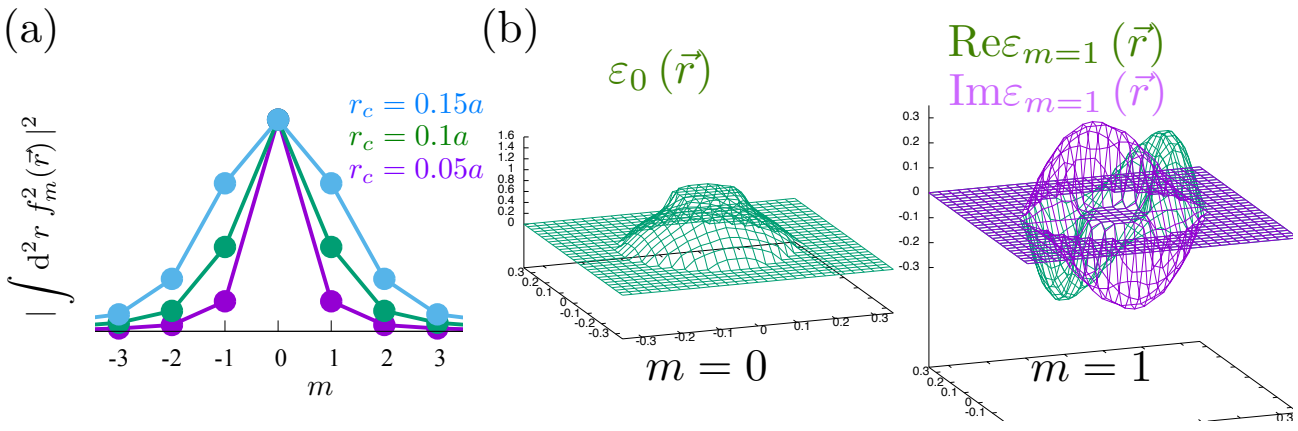

Figure 6.7: (a) Convergence of the fourier coefficients for the circular motion for different values of radius $r = 0.05a, 0.1a, 0.15a$. The intensity is determined by the total value $\int dr^2\ f_m^2(\vec{r})$. The spectrum sufficiently decays at $m = 2$. (b) The spatial profile of the dielectric constant for fourier components of $m = 0, 1$. The $m = 0$ component is the time average of the spatial profile and it extends in the radius of $r + r_h$ meaning it skirts outside. The $m = 1$ component has the real and imaginary component, reflecting the TRS breaking motion.

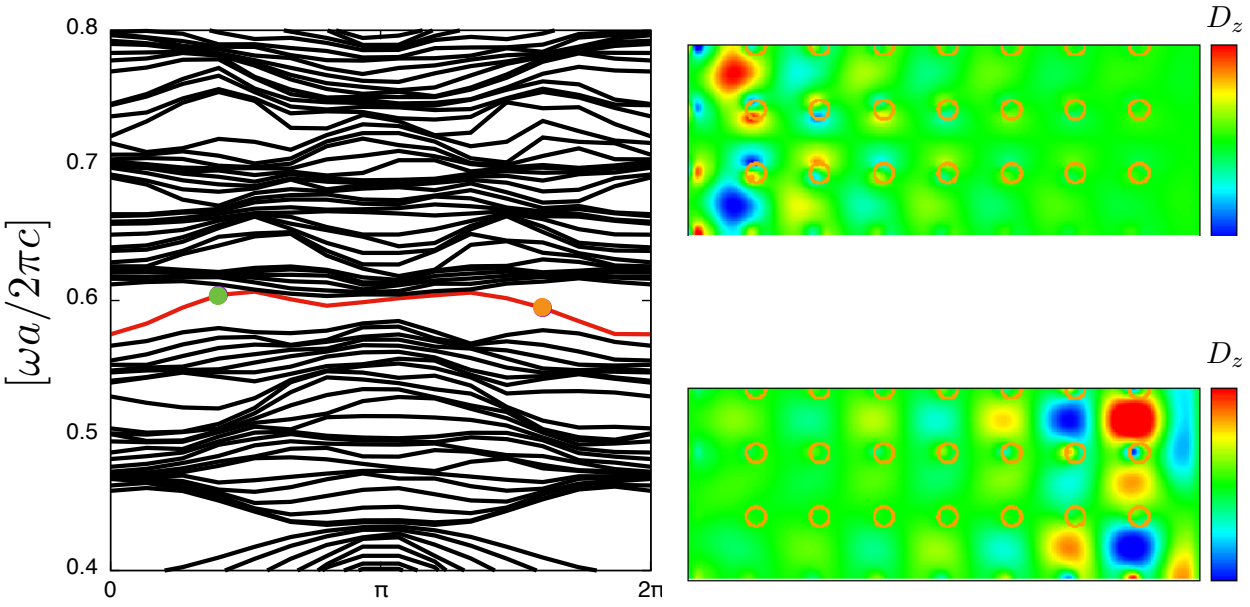

Figure 6.8: Floquet mode dispersion in the finite width system. The chiral edge mode dispersion is seen in the topologically non-trivial gap with Chern number -1. The green(orange) point indicates the eigenmode corresponding the upper(lower) right figure of the mode profile of the edge mode.

we can learn almost nothing. However most lines in the spectrum do not repulse at crossing points and thus, most of spectrum are irrelevant of an incident light. Because of this, it is validated to select bands that potentially couple to the incident light from the spectrum in the static case. Then by solving the eigenequation including the time-varying effect, we obtain a clear Floquet band diagram. This study is unique in that the effect of temporal modulation is considered for continuous states which are not strongly bounded around a certain point, while in many cases topological Floquet band structures are obtained for sufficiently localized states with large band gaps from bands above and below.

The time-varying potential may be implemented by nonlinear effect and external driving fields. For example, two same wave propagation in the opposite directions forms a standing wave, and then displacing the frequency for either wave moves the standing wave profile. Then oscillating modulation of the frequency difference cause oscillation of the standing wave. Further, a pair of counter propagating waves form a 2D standing wave pattern and oscillating modulation of the frequency differences for two directions but with phase difference of $\pi/2$ would cause circular motion of the 2D standing wave pattern. This modulation has already been achieved in several systems. However, photonic systems do not seem to accommodate this since even if such a modulation is caused by a light, the fastest signal in universe, the photonic motion itself is of course comparable and this cause latency in the spatial modulating pattern and expected effect could not be achieved. Because of this, a system such as an elastic system is a rather preferable candidate. Since the Floquet modes depend on the way of temporal variation, we can switch the direction of chiral edge modes at will.

Chapter 7

Structual deformation and the band structure in synthetic space

7.1 Structural deformation in woodpile photonic crystals

In this chapter, we consider to allow certain structural deformation and relate the new degree of freedom to extra dimensions. Specifically, we consider the chiral woodpile photonic crystal, which is constructed by stacking layers of rods with in-plane rotation. The woodpile structure is broadly used as 3D photonic crystal due to its fabrication easiness and structural flexibility. As discussed in a previous section, the woodpile structure shows various functionalities according to the way of the stacking. The Woodpile photonic crystal with the fcc translational symmetry is famous to show an omnidirectional band gap. On the other hand, the chiral woodpile photonic crystal is known for showing circular dichroism for light propagating in the stacking direction or for Weyl points in the band structure due to its screw rotational symmetry as described in a previous section.

In principle, a periodic woodpile structure is realized by repeatedly stacking n distinguishable layers in the same order. Two layers are distinctive if a material property such as the dielectric constant, shape of the rod, direction of the rod or relative position is different. Among them, the relative position of the layers are easily varied without changing the size of the unit cell or preparing multiple kinds of materials. Since we can always retake a crossing points of two layers as an original point, the structural degree of freedom for the relative positions is $n-2$. Then, we have $n-2$ parameters for the deformation by slide. Further, each parameter is periodic since the displacement equal to the inter-spacing between rods is identical to the original structure. Only in the case of $n=2$ or $n=3$, the inter-spacing between rods becomes equals to the lattice constant of the structure. Although the $\pi/4$ chiral structure has the transnational symmetry of the square lattice, the interspersing are different between even and odd layers. In the case of the $\pi/3$ chiral woodpile structure, it has

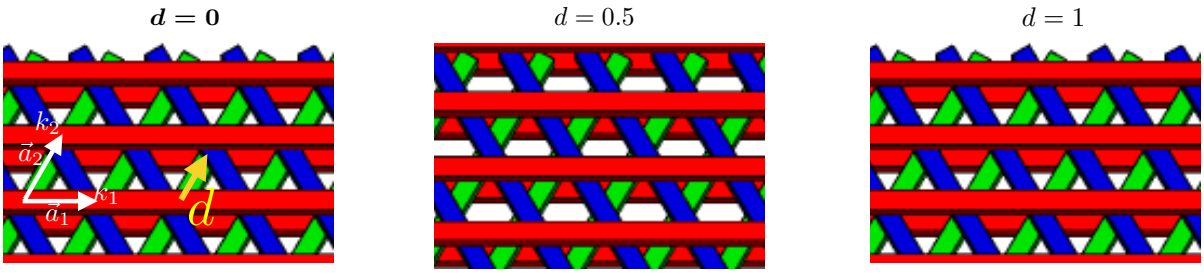

Figure 7.1: Structural deformation of the $\pi/3$ chiral woodpile structure. The crossing point between the 2nd layer(shown by green) and the 3rd layer(shown by Blue) is taken as the origin. Deformation is caused by sliding the 1st layer(shown by red) in the direction depicted by the yellow arrow in the left figure. Seen from top, it forms a triangular lattice at $d=0$, and a kagome lattice at $d=0.5$. Then, it returns to the original structure at $d=1$.

three distinguishable layers and then, the structural deformation degree of freedom by the displacement is one. The deformation is parametrized by d as the displacement of the first layer in a direction(See Fig. 7.1). Without deformation($d = 0$), it forms the triangular lattice seen from top, and it forms kagome lattice at $d = 1/2$, It finally returns to the original triangular lattice at $d = 1$. The eigenspectrum for each deformation parameter forms a certain dispersion curve as a momentum degree of freedom. Thus, it is plausible to introduce the deformation parameter d as an extra dimension in the momentum space.

We consider the dielectric (GaAs, the refractive constant $n = 3.4$) $\pi/3$ chiral woodpile photonic crystal formed by stacking layers consisting of array of rods with unit length spacing($a = 1$). We set the width of each rod as $130/500$ and the thickness as $1/3$. The Bravais lattice of the structure forms the equi-length hexagonal lattice. Without the deformation ($d = 0$), it is same as that taken in a previous section, and it has two Weyl points with the same chirality in the $k_z = 0$ plane and other two Weyl points with the opposite chirality in the $k_z = \pi$ plane. A symmetric consideration of the structure gives a reason for the Weyl points. The $\pi/3$ chiral woodpile structure($d = 0$) is invariant under the combination of $\pi/3(-2/3\pi)$ rotation around the stacking(z) axis and $1/3$ fractional rotation along the z axis, that is, the screw symmetry.

As explained by Young *et.al.* in their work [101], a nonsymmorphic symmetry gives rise to Weyl points in the band structure. The nonsymmorphic symmetry is the invariance under the combination of a rotation(including inversion) and a fractional translation. In the Brillouin zone, the points on the line parallel to k_z passing on the Γ, K or K$'$ point is invariant under the $\pi/3(-2/3\pi)$ rotation around the z axis. As a consequence, there is additional $1/3$ translational invariance on those lines and the reduced Brillouin zone is folded into $1/3$ of the original region. This $1/3$ folding causes at least two crossing points(at $k_z = 0$ and π in a mirror symmetric case), forming a Weyl point in the Brillouin zone. Therefore in this structure, the bands should be considered per the bundle of three bands.

With the deformation ($d \neq 0$), the structure loses the $\pi/2-$rotational symmetry but recovers it at $d = 1/2$. Since any two level hermitian system has three parameters at most, one of the four parameters (k_1, k_2, k_3, d) is redundant and the degeneracy forms a loop in the 4D parameter space. Further in this structure with the deformation, we can make use of a symmetry to reduce the variation. The structure with the deformation $-d$ is given by the $\pi/2$ rotation of the structure with the deformation d. Thus, the eigenequation is invariant under $(k_1, k_2, k_3, d) \to (-k_1, -k_2, k_3, -d)$. and we can find out the entire trace of the degeneracy point while the d is changed just by examining the region $0 \leq d \leq 1/2$. Further, we can find out the trace of the degeneracy points from these facts. TRS relates the Weyl point at $\boldsymbol{k}$ to $-\boldsymbol{k}$ with the same chirality. Without the displacement, the structure further has the $\pi-$rotational symmetry around the $z-$axis and the combination of these transformations confines makes the dispersion along the line passing on the K, K$'$ or Γ point mirror symmetric with respect to $k_z = 0$. In this case, the weyl points(crossing points after the $1/3$ folding) arise in the $k_z = 0$ or $k_z = \pi$ plane. With a finite d, the $\pi-$rotational symmetry is broken and the Weyl points are no more confined within the plane.

Starting from the Weyl point between the second and third bands at K point, the d moves the Weyl point out of the $k_z = 0$ plane, to $+k_z$ specifically in this configuration. Increasing the displacement, it moves toward $k_z = \pi$ and returns to the K point at $d = 1/2$. While this, the Weyl point at the K' point for $d = 0$ moves toward $k_z = -\pi$ due to time reversal symmetry. Since the trace during $1/2 \leq d \leq 1$ is known from the trace during $1/2 \geq d \geq 0$ and $\pi-$rotation around the $z-$ axis, the Weyl point at the K point moves toward $k_z = -\pi$ for $d \geq 1/2$ and it returns at $d = 1$. Since the structure always has the screw symmetry with the $-2\pi/3$ rotation irrespective of the d, the degeneracy points must be on the line. The breaking of the screw symmetry, for example by changing the rod width for one layer, may bends the straight line.

In next, we examine the band structure in the $d - k_1$ space changing k_2 or k_3 and examine the first Chern number obtained there.

$$
\begin{aligned}
C^1_{41}(R_2, R_3) &= \int \mathrm{d}R_4 \mathrm{d}R_1 \; B_{41}(R_1, R_2, R_3, R_4) \\
(R_1 &:= k_1, R_2 := k_2, R_3 := k_3, R_4 := d) \\
B_{ij} &= \nabla_i A_j - \nabla_j A_i \\
A_i &= \langle \psi | \nabla_i | \psi \rangle,
\end{aligned}
\tag{7.1}
$$

here the section Chern number is given as a function of k_2 and k_3. Since the case of the fixed d is a usual case, we should consider the Chern number utilizing the d. Of course, if the dispersion against the d and k_1 is

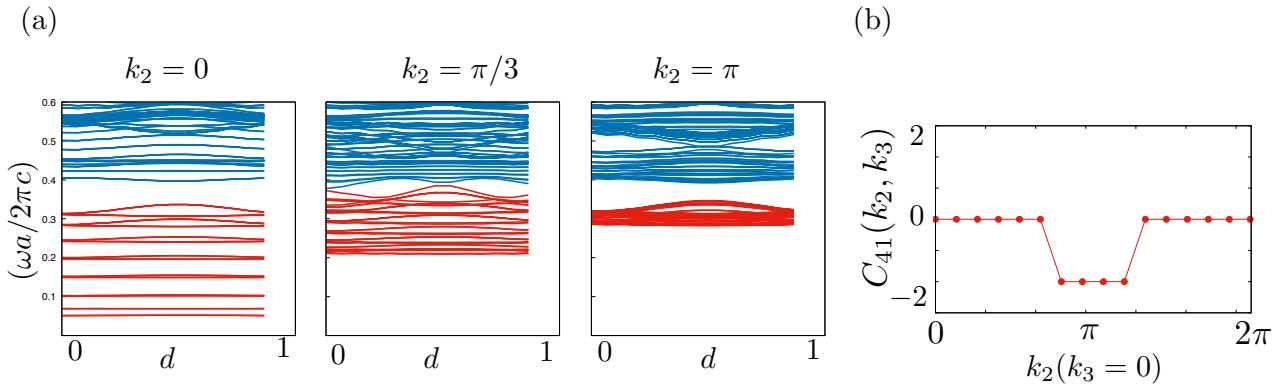

Figure 7.2: (a) Plots of band structures on the $d - k_1$ plane(projected in the k_1 direction) for several values of k_2. The k_3 is fixed to zero in all plots. (b) Plot of the section Chern number C_{41} which is defined on the $d - k_1$ plane. The Chern number changes at $k_2 = \pi/3, 2\pi/3$, where two Weyl points lie.

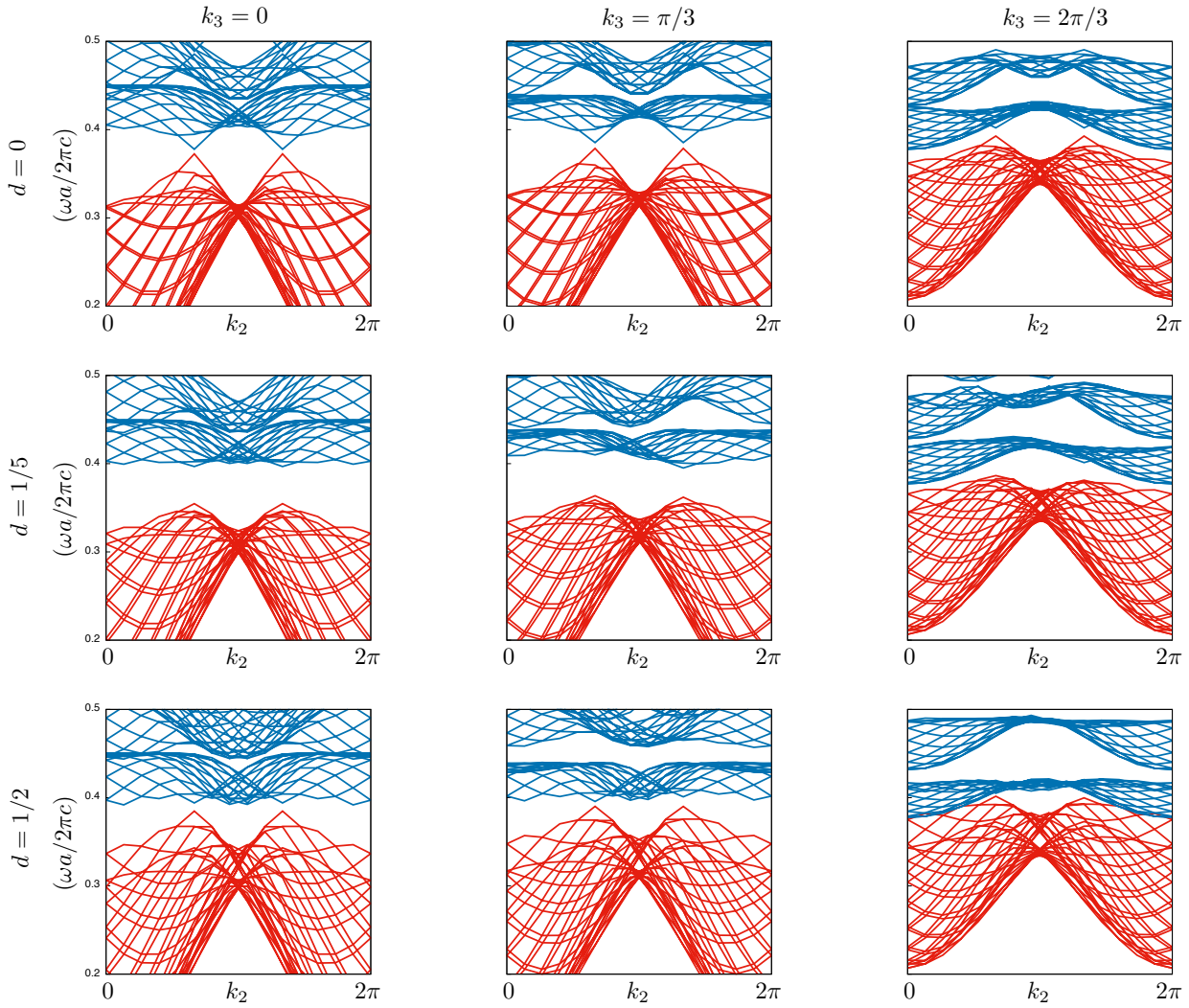

Figure 7.3: A collection of 2D band dispersions for several values of d and k_3. The band dispersions for $d = 1/2$ resembles that for $d = 0$.

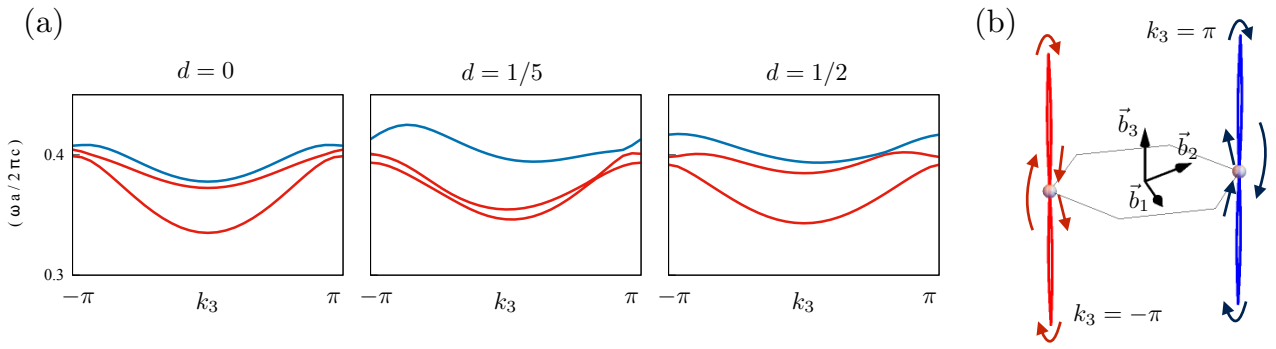

Figure 7.4: (a)The band dispersion along the line parallel to the k_3 passing on the K point. Because of the $-2\pi/3$ screw symmetry, the Weyl point is confined on the line for any value of d. The Weyl point moves with varying d. (b)A schematic of the trace of the nodal point for $0 \leq d \leq 1$.

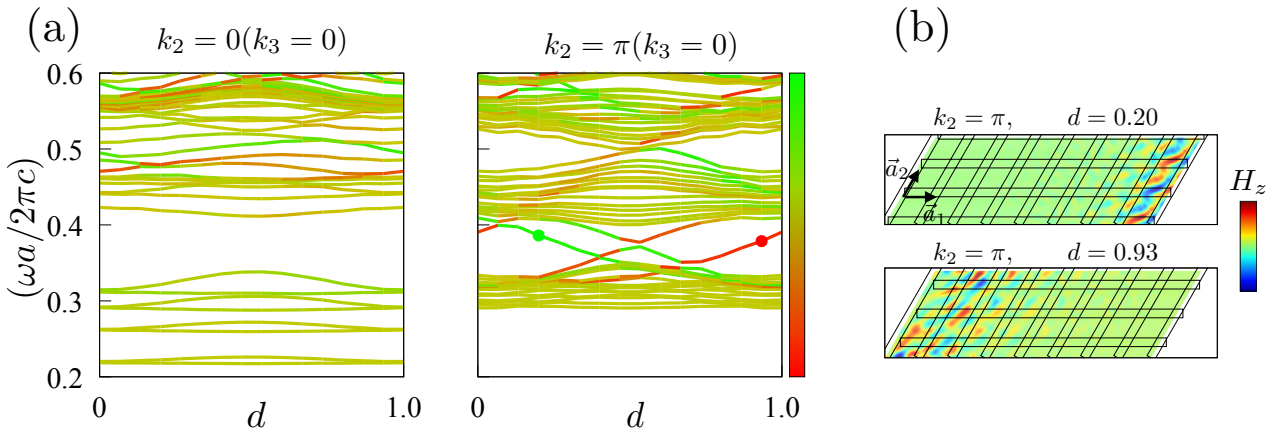

Figure 7.5: (a)The eigenfrequency dispersion against the structural deformation d in the finite width geometry with the width of 8 unit cells in the $\vec{a}_1$ direction. The color of the line represents the normalized moment in the $\vec{a}_1$ direction(explained in the main text). The red means the mode is localized at the left edge while the green means it is localized at the right edge. (b)The H_z profiles of the edge modes in a z slice(the intersection of the woodpile structure in the slice is also shown by black lines). The above(below) image shows the profile of the edge mode localized at the right(left) edge, which is denoted by a green(red) point in the Fig. (a).

continuously deformed into the isolated atomic limit, the Chern number is trivial. We first focus on $k_3 = 0$. In the Fig. 7.2 the band structure on the $d - k_1$ plane for several values of k_2 are plotted. At $k_2 = 0$, the 2nd and 3rd bands are gapped and the gap closes twice at $k_2 = 2\pi/3$ and $k_2 = 4\pi/3$ because of the $\pi-$rotational symmetry at $d = 0, 1/2$. The existence of two Weyl point at $k_2 = 2\pi/3, 4\pi/3$ may cause the change of the Chern number by ± 2 or not cause the change if the Weyl point charges are opposite for them in the k_2 slice. The numerical evaluation of the Chern number by the method [76] and a localized basis set [75] is shown in Fig. 7.1. Indeed, the Chern number Changes by two at $k_2 = 2\pi/3$ or $k_2 = 4\pi/3$. The ± 2 change of the Chern number means the Weyl point charge is same for the k_2 slice. Note that inn the slice of $k_3 = 0$, the chirality of Weyl points are different between the point in the $k_2 = 2\pi/3$ and that in the $k_2 = 4\pi/3$, whereas they are same in the $d = 0$ or $d = 1/2$ slice. The opposite chiralities in the $k_3 = 0$ slice are known from the $\pi-$rotational symmetry around the $z-$axis$((k_1, k_2, d) \to (-k_1, -k_2, -d))$. Also we mention the Chern number change against k_2 for $k_3 \neq 0$. Since the degeneracy point returns to $k_3 = 0$ at $d = 1/2$, the degeneracy curve connects the $(k_3, d) = (0, 0)$ and $(k_3, d) = (0, 1/2)$, the Chern number change against k_2 is same until upper bound of the curve in k_3.

In next, we consider the consequence of the nontrivial Chern number. In the usual band structure for momentum, a value of Chern number predicts the number of chiral edge modes appearing in the gap. This is

confirmed by truncating the periodic structure in one direction to form a cylindrical geometry and plotting the eigenspectrum dispersion along the periodic direction. It could not be specified straightforwardly what means to create a boundary for the deformation parameter d, we can only consider here to create a boundary in the a_1 direction for the momentum k_1, and examining the dispersion in a cylindrical geometry changing the d for fixed k_2 and k_3. In Fig. 7.5, several results of the eigenspectrum for varying d in a cylindrical geometry for several values of k_2 with $k_3 = 0$ are shown. In the figure, the color of the line represents the moment of the magnetic field intensity in the a_1 direction $\int \mathrm{d}^3 r\, a_1 \vec{H}^2_{nk}(\vec{r})$. The color is ranged from 0 to 1 and the value of the moment is normalized to be 0 for the left most position and 1 for the right most position. For $k_2 = 0 (k_3 = 0)$, the section Chern number is trivial and the dispersion in the cylinder is same as that of the bulk. On the other hand, for $k_2 = \pi (k_3 = 0)$ the section Chern number takes the value of -2 and two Chiral edge modes are found in the gap reflecting the Chern number. This means that bulk-edge correspondence holds in this case as well. Note that the termination varies according to the d. In the above analyses, we set the termination as shown in the Fig. 7.6. Taking the crossing points between the 2nd rod(green) and the 3rd rod(blue) as the origin, we place the central of the unit rod with the length of 1 at the origin for $d = 0$. Then, the 1st rod(red) is moved to the direction of the $\vec{a}_2$ with the length of d. However the specific choice of termination does not affect the fundamental result according to the bulk-edge correspondence and indeed we confirmed it for another unified rule for the termination.

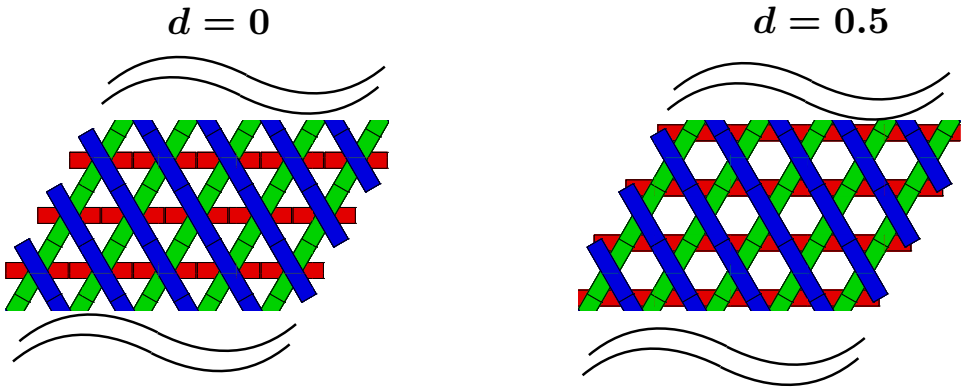

Figure 7.6: A schematic of the termination used in the analyses of Fig. 7.5 for $d = 0$ and $d = 1/2$. The rule for the termination is described in the main text.

The edge modes related to the Chern number here are not unidirectional propagation modes since TRS of the system is not broken. The first thing we can utilize from the above bulk-edge correspondence is that we can always find edge mode localized in either gap at arbitrary frequency in the gap for any value of k_2 with the same non-zero Chern number. Since edge modes related to the non-zero Chern number traverse the gap, we can always find the eigenmode with a required frequency by adjusting the d. Secondly, we can have two domains with different values of d for each domain. If we adjust the d of the left domain for the edge mode to be localized at the right side and also the d of the right domain for the edge mode there to be localized, localization of the edge mode is strengthened at interface.

However in the above consideration, the k_2 and k_3 are always fixed to constants. It is unavoidable to accompany disorder in periodicity and the k_2 or k_3 is not thoroughly fixed in practice. Since the band structure is not fully gapped in the entire Brillouin zone, the disorder scatters edges modes into bulk in this case.

In the following, we discuss how non-zero Chern can be realized with the structural deformation. Seeing a sequential slice of the deformation, if a band structure has a Weyl point at a certain slice of the deformation, it changes the value of the Chern number defined with the deformation and one momentum. In this case, the Chern number can take a non-zero value. However due to a certain symmetry, multiple Weyl points can be included with in a momentum slice and even Weyl points can cancel the Weyl point charge each other. Also without Weyl point, the Chern number with deformation can take a non-zero value and in that case the Chern number is unchanged under whole momentum, since deformation is irrelevant to time reversal while

momentum is inversed. In the above case of the $\pi/3$ chiral woodpile structure, the combination of time reversal and $\pi-$rotation around the $z-$ axis works as the mirror symmetry in the $d - k_1$ parameter space. Because of the mirror symmetry, the Chern number must vanish at $k_2 = 0$. As mentioned in , existence of mirror symmetry in the 2D slice of parameter space leads to vanishing of Chern number. Thus, any mirror symmetric deformation, which falls to parametrization of deformation such that $d = 0$ for an original structure, $d = 1/2$ for a maximal deformation, and just going back the process for $1/2 < d \leq 1$. For example, one may consider the Haldane's honeycomb model and the flux intensity their as the deformation parameter. However the degree of flux intensity is decoupled from other two momentum and it must be taken mirror symmetric.

In the case of the $\pi/4$ chiral woodpile structure, it has two parameters for the structural deformation by sliding the layers and we define a parametric loop in a good way, it can cause the constant finite Chern number for the entire momentum.

7.2 Structural deformation of 2D photonic crystals

We can also consider similar structural defromations for a two dimensional structure such as the one shown in Fig. 7.7. The structure is 2D version of the $\pi/3$ chiral woodpile strcuture since they are same in top view, while the 2D version is uniformly extende in the z direction(Fig. 7.7(b)). The structural deformation is defined in the same way by the displacement of the blue-colored layer in the direction indicated in the Fig. 7.7(a). However, in this 2D version, the structural deformation changes volume fraction of the dielectric part(effective refractive constant), which moves the band center. Nevertheless, if a gap is preserved during the deformation, topological invariants are still defined. Since overlapping area among rods is minimum for $d = 0$, the filling ratio is minimum at $d = 0$, and maximum at $d = 1/2$.

Confining the k_z to $k_z = 0$, it reduce to the 2D problem and electromagnetic modes are separated into TE or TM mode. Here, we focus on the TM mode. The TM mode band structures for several slices of d are shown in Fig. 7.8. Since this structure is two dimensional, the screw symmetry of the three dimensional $\pi/3$ chiral woodpile structure does not exist and the bundle of three bands is not found here. The clear band gap between the 1st and 2nd bands closes at K and K' points once for $d = 1/2$. Then, the section Chern number given by one momentum(k_1) and d for the fixed rest one(k_2) changes by one at those *Weyl* points(Fig. 7.9(b)). For this 2D structure, dispersions at $d = 0$ and $d = 1/2$ behaves differently and gap closes only for $d = 1/2$ and the change of Chern number in this case is ± 1.

In next, we show the frequency dispersions to the displacement d in the finite width geometry for several values of k_2 in the Fig. 7.9(a). The dispersion is obtained by setting 8 unit cells with termination by the perfect conductor(vanishing boundary condition) for both sides. We chose the vanishing boundary for excluding modes propagating in air region. Though the gap between the 1st and 2nd bands are mostly below the light cone for larger k_2, the gap is above the light cone for smaller k_2 since the light cone ends in $\omega = 0$. In the frequency region corresponding to the bulk-gap, the dispersions of edge modes, which is localized at either side of the geometry, are seen to appear. Let us see the edge mode dispersions from the left figure in Fig. 7.9(a). The color on the line represents the moment of the electric field E_z as previous. The red(green) color means the eigenmode is localized at left(right) side of the geometry. In the $k_2 = 0$, there appears edge mode dispersion in the middle of the bulk gap, which remains to be localized at the left side during the deformation. In the $k_2 = \pi/3$, the edge modes are localized only the vicinity of $k_2 \approx 0$ and the modes on the line extends in the bulk since the bulk gap is closed at $d = 1/2$ in this case. Finally in the $k_2 = \pi/2$, where the Chern number is -1, the edge mode dispersion in the bulk gap traverse the gap once, and the direction of the chirality is consistent with the value of the Chern number -1. Note that also in this structure the (k_1, k_2, d) and the $(-k_1, -k_2, -d)$ are related by the $\pi-$rotation around the $z-$axis. Then, if the termination is symmetric, the dispersions in $k_2 = 0$ and $k_2 = \pi$ must be symmetric with respect to d. However, the dispersions in the Fig. 7.9(a) are not. This difference occurs due to the slight difference of the configuration of the gaussian bases. If they are set symmetrically, the dispersion would be symmetric.

In next, we compare the dispersion in the finite width geometry for several values of d slices. In this case, we consider air termination for the finite width structure of 8 unit cells. The obtained dispersions are shown in Fig. 7.10. Note that the result is not same as the Fig. 7.9(a) since the situations are different in the termination. During the deformation, the left and right edge modes change their frequency separately. Therefore, we can

choose which side the edge modes are localized at for a certain frequency by tuning the d. Moreover, we can consider a waveguide sandwiched by the two woodpile photonic crystals. If we tune the left side woodpile photonic crystal to excite the right edge mode while the right side one is tuned to excite the left edge modes, the localization of the mode may be strengthened. On the other hand, if we only tune the either side of the woodpile photonic crystal to excite the edge mode, the waveguide mode inclines to the one side.

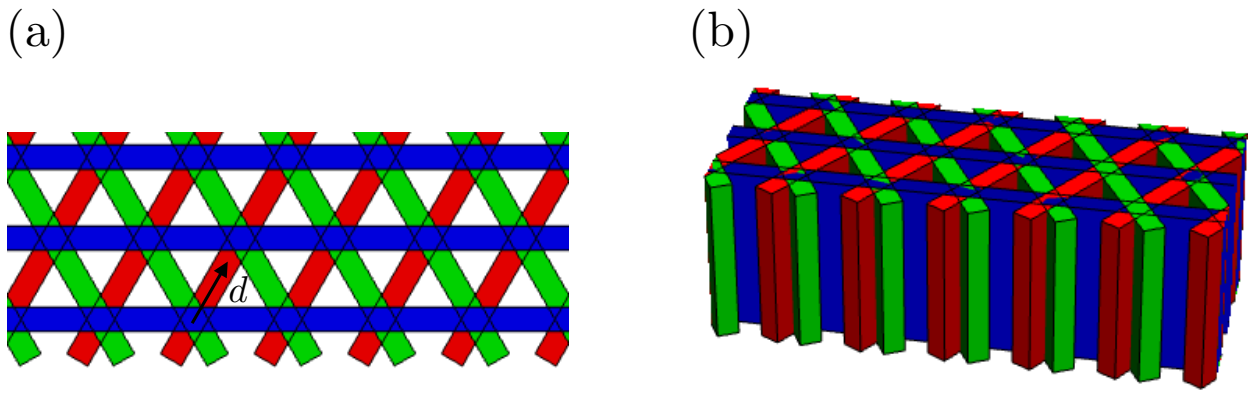

Figure 7.7: Schematics of 2D triangular woodpile structure. (a) Top view of the structure. (b) Oblique view of the structure. the structure is uniform in the z direction. The dielectric constant is same within the structure.

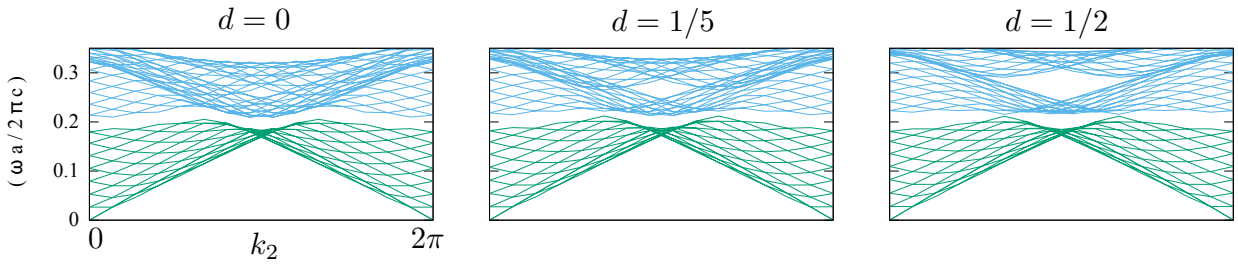

Figure 7.8: Frequency dispersion diagrams plotted to $k_2 - k_1$. The first band is distinguished with different color(green) from other bands(blue).

7.3 Structural deformation in a tight-binding model

We attempt to reproduce the essence of the properties in the structural deformation by a simple tight-binding model. The electromagnetic field within the woodpile photonic crystal is strongly localized at contact point between two rods. Then, it is appropriate to put the nodal points on the contact points in the tight-binding model. Since the electromagnetic field is also localized within the rod, we assume that the profile of the intense field near the contact point is represented by a dipole orbit and they couple only between nodes within the same rod. For the woodpile structure stacked with $\pi/3$ in-plane rotation, the $p-$type orbit is placed at each of three independent points in the unit cell along each rod(see Fig. 7.11). We assume the strength of tunneling rate is determined according to the distance between two points. The closer two orbitals, the stronger the tunneling rate between them is. The tight-binding hamiltonian reads

$$H = \sum_{i,k} \left[t_1 (a^\dagger_{i,k+1} a_{i,k} + h.c.) + t_2 (a^\dagger_{i+\mu_k,k-1} a_{i,k} + h.c.) \right]. \tag{7.2}$$

The $t_1(t_2)$ represents the tunneling ratio on the link shown by blue(red) in the Fig. 7.11). The strength of the tunneling varies during the deformation.

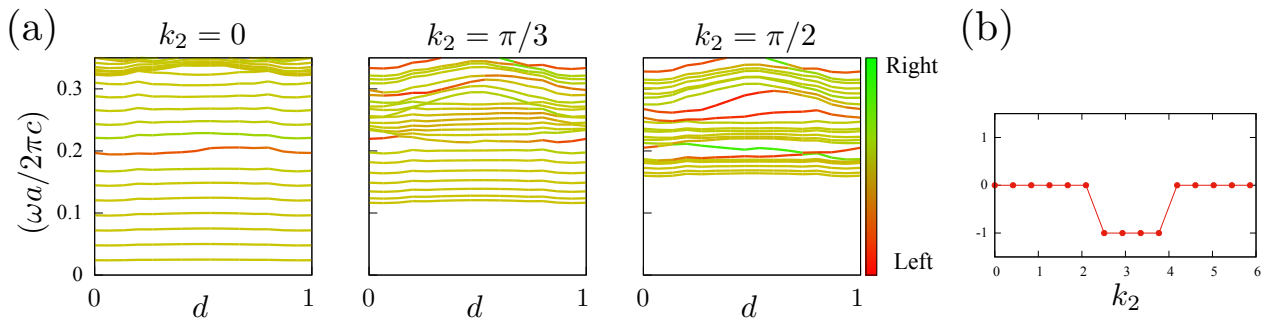

Figure 7.9: (a)The eigenfrequency dispersion agains the structural deformation d in the finite width geometry of 8 unit cells in the $\vec{a}_1$ direction with termination by the perfect conductor(vanishing boundary condition). The color of the line represents the normalized moment in the $\vec{a}_1$ direction. (b) The plot of section Chern number to k_2, which is given by k_1 and d.

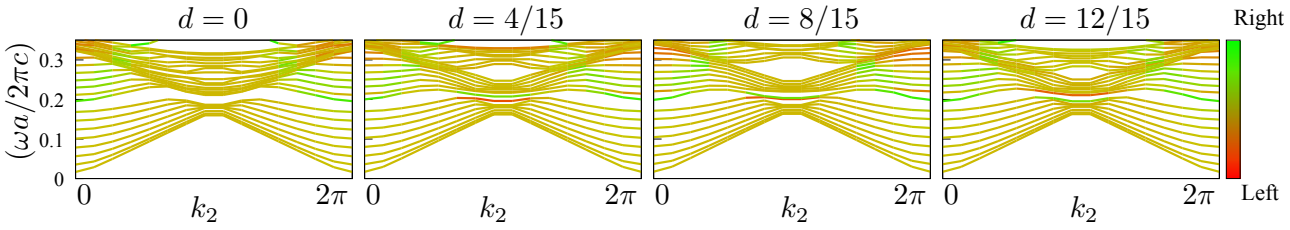

Figure 7.10: The eigenfrequency dispersion plotted to k_2 for several values of d in the finite geometry of 8 unit cells in the $\vec{a}_1$ direction with air termination(vacuume space of 2 unit cells for both sides). The color of line represents the moment of the eigenstate in the $\vec{a}_1$ direction.

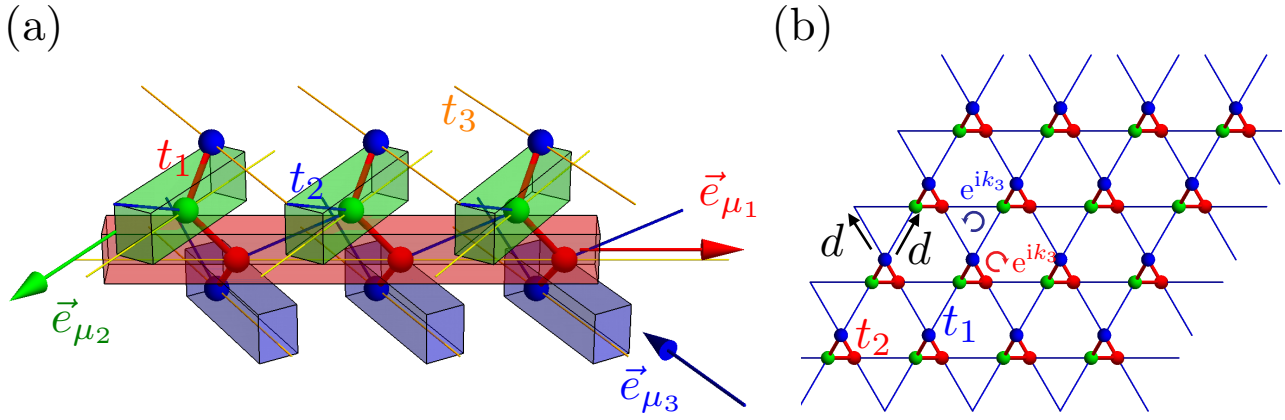

Figure 7.11: A schematic of the tight-binding model(at $d = -0.3$). (a) The red, green and Blue color of rods represent the first, second and third layers respectively. Nodes are placed within the rod and the internal position within the rod varies during the deformation. At $d = 1/2$, nodes are placed at touching points of two rods and the green, blue and red spheres represent the touching points between the 1st and 2nd, the 2nd and 3rd, and the 3rd and 1st layers respectively.The $\vec{e}_\mu$ specifies the rod direction. The red, blue, and yellow links between points represents the tunneling links with strength of t_1, t_2, and t_3 respectively. (b) Top view of the tight-binding model. A non-zero k_3 cause a hopping phase on the closed triangular path of the blue(red) links with the flux $k_3(-k_3)$. During deformation, the blue point remains to be fixed while the grenn and red points move by d in the direction indicated in the figure(b).

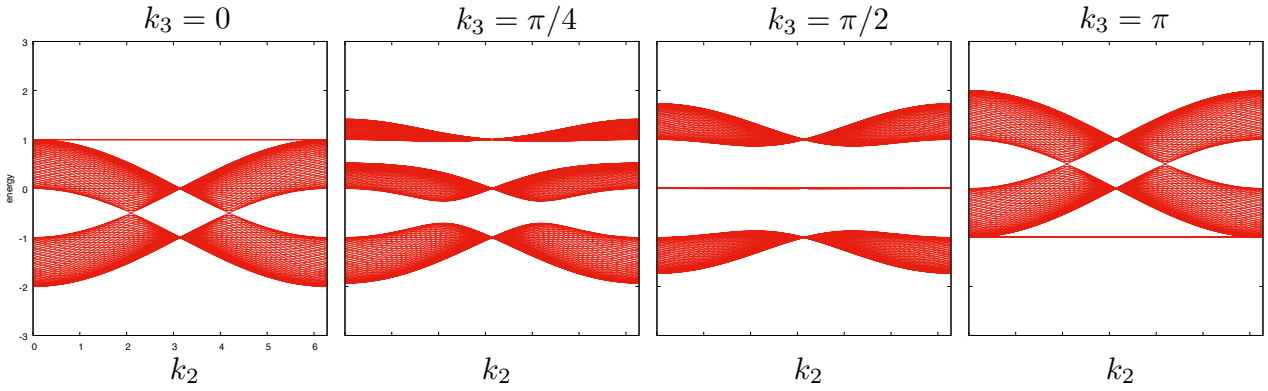

Figure 7.12: Energy dispersions of the structure $d = 1/2$ plotted in the 2d slice Brillouin zones for several values of k_3.

First, let us focus on $d = 1/2$. The top view of the structure forms a Kagome lattice(Fig. 7.11 (b)). Although the model is three dimensional, if we fix the $k_3 = 0$, it is a 2D tight-binding model and the band structure of the Kagome lattice without flux includes a flat band on top, where we set the hopping constant to a minus value ($t_1 = t_2 = -1$). A non-zero k_3 induces a flux pattern in the hopping phase(Fig. 7.11), and the flat band gets dispersive. However, another flat band reappears at $k_3 = \pi/2$ in the middle in the energy. Finally at $k_3 = \pi$, the flat band reappears in the bottom(Fig. 7.12). The phase $e^{ik_3=\pi} = -1$ is equivalent to inverting the hopping constant since $(-1)^3 = -1$. The result of the tight-binding model well reproduces the properties of the $\pi/3$ chiral woodpile structure. In the 3D Brillouin zone, the transition point is the Weyl point and Chern number between the transition point takes non-zero value. The section Chern number plotted to k_3 ($d = 1/2$) are shown in the Fig. 7.13. The bundle of three bands in the Fig. 7.14 also well reflects the nonsymmorphic symmetry that the chiral woodpile structure possesses.

As being described so far, the tight-binding model well reproduce the characteristics of the woodpile photonic crystal with deformation. Then, we can study the mechanisms in detail with the simplified model and it also allows us to study the deformation in three dimensional cases more easily.

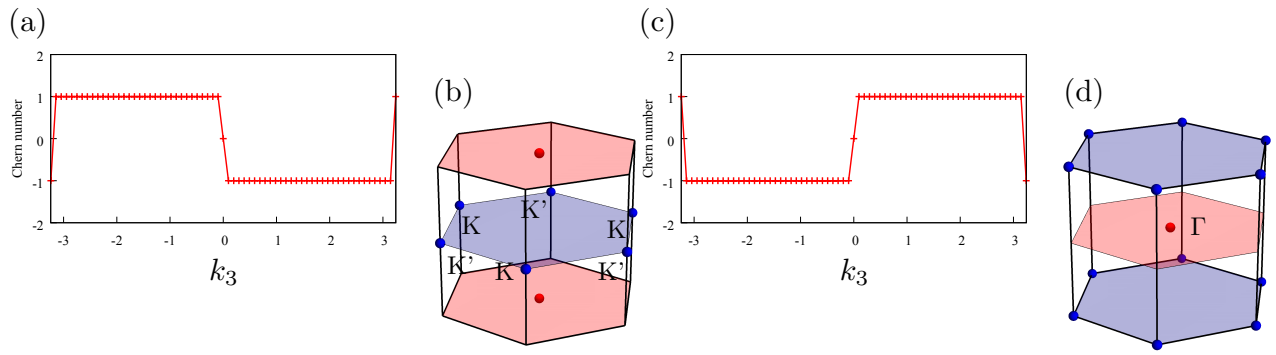

Figure 7.13: (a) The plot of section Chern number for the first gap(Chern number of the lowest band). (b) The locations of Weyl points in the Brillouin zone. The red(blue) color of the Weyl point means topological charge of $+1(-1)$. (c) The plot of section Chern number for the second gap(the total Chern number of the lowest two bands). (d) The same plot as (b) for the second gap.

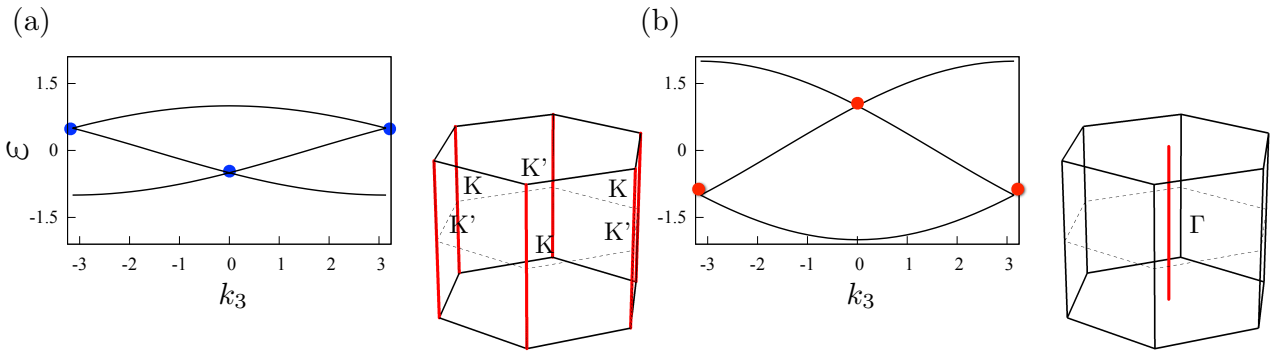

Figure 7.14: (a) Plot of eigenspectrum to k_3 on the line that passes the K or K' point indicated in the right figure. (b) Plot of eigenspectrum to k_3 on the line that passes the Γ point indicted in the right figure.

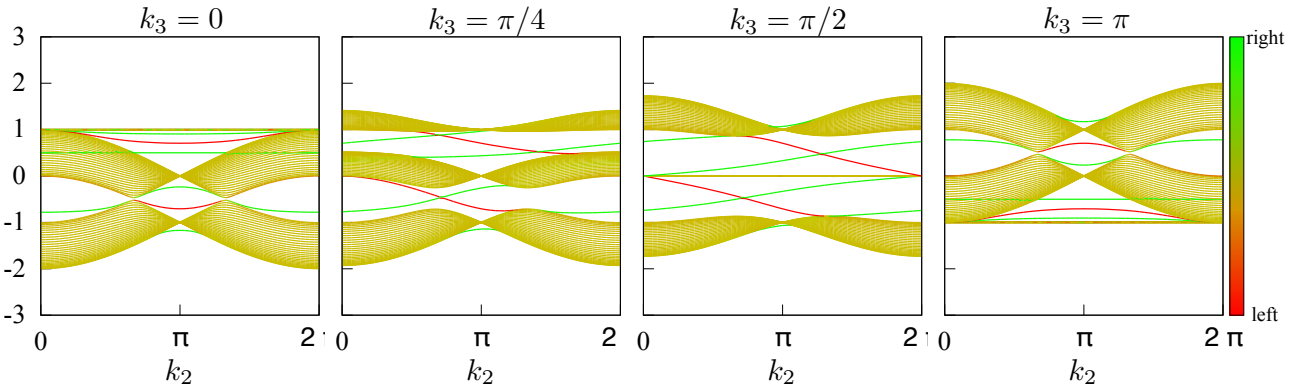

Figure 7.15: The plots of energy spectra in the finite width geometry(30 unit cells). The color of the line represents the moment of the mode intentisty in the $\vec{a}_1$ direction;The red(green) means that mode is localized at lef(right) side.

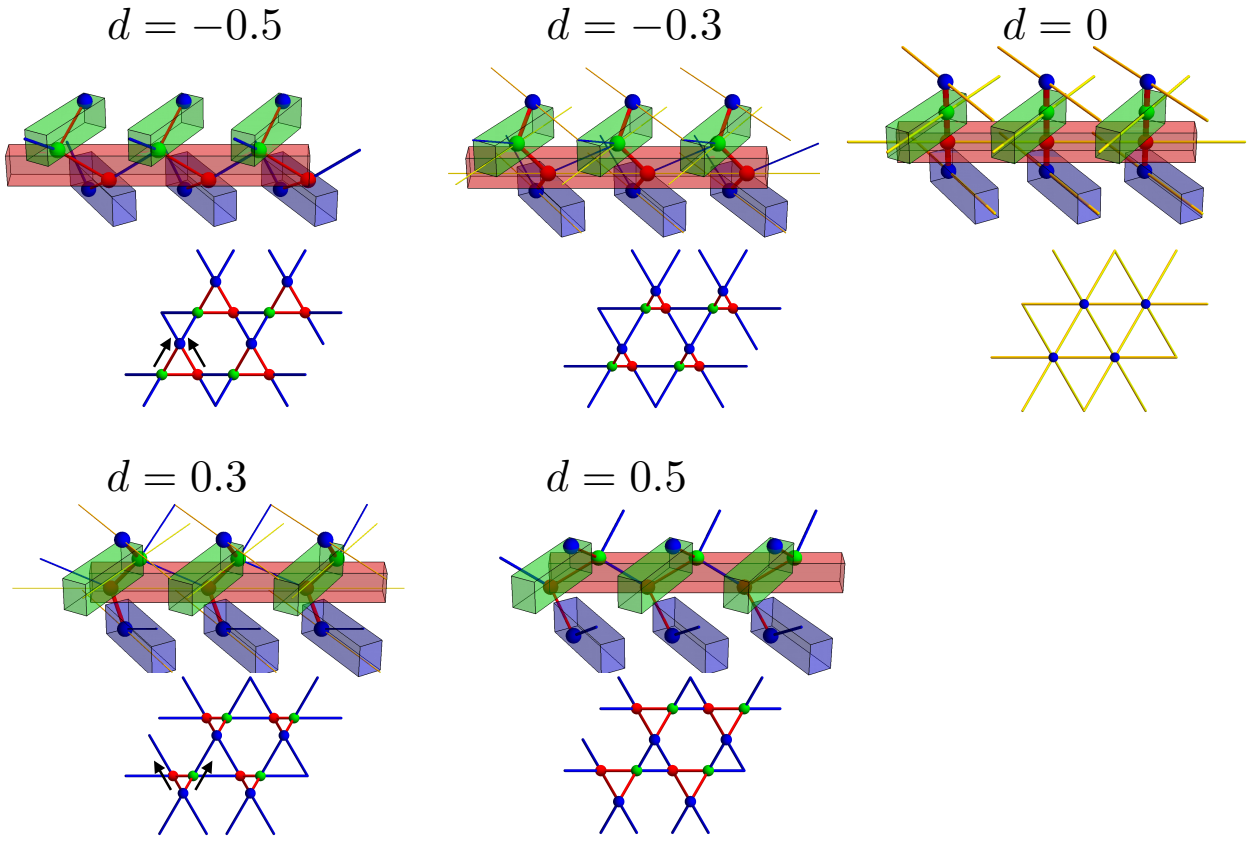

Figure 7.16: Tightbinding models during the deformation shown with the top views($-0.5 \leq d \leq 0.5$).

7.4 Conclusion

In this chapter, we consider structural deformation of the woodpile structure and introduce the parameter for structural deformation as a fictitious momentum. We discussed the bulk-edge correspondence, in the synthetic Brillouin zone consisting of momentum and introduced parameter. As a consequence, the variation of edge modes during the structural deformation can be characterized by the Chern number obtained by using the deformation parameter and can give another justification for edge modes appearing under TRS. Also, we demonstrate it in a two-dimensional structures, even thought in the case filling factor of dielectric material varies during deformation. Moreover, we found a tight-binding model that well reproduce the characteristics of the woodpile photonic crystal with deformation. We can studies the mechanisms in detail with the simplified model and it also allows us to study the deformation in three dimensional cases more easily. Since the woodpile structure is a three-dimensional object, total degrees of freedom including one for structural deformation are indeed four and it has opportunity for the second Chern number, which is well defined topological invariant on four dimensional Brillouin zone. However, two bands are insufficient for non-zero second Chern number because then it is degenerated on a line or trivially gapped. Since the second Chern number is well formalized for four band system with Kramars degeneracy, structural deformation keeping the symmetry under artificial time reversal operation that satisfies $\mathcal{T}^2 = -1$ in combination with spatial rotation would lead to the finding of non-zero second Chern number in deformation of a 3D structure. On the other hand, it would also be interesting to find what corresponds to termination in the structural deformation and consider the bulk-edge correspondence for the termination.

Chapter 8

Conclusions

This thesis was dedicated to the theoretical investigation of topological properties of photonic band structures and topologically protected photonic edge modes. For numerical evaluation of topological invariants of photonic bands, we established the gaussian expansion method for the Maxwell equations in Chapter4. For a spatially localized basis set, the eigenvalue problems for Bloch states are periodic in the wavenumber and then we can numerically obtain topological invariants directory from the eigenvectors.

With the gaussian expansion method obtained in Chapter4, the photonic crystal consisting of honeycomb array of helix-shaped holes in the dielectric material was analyzed. The edge modes propagating along the spiral shapes were related to the section Chern number given in the 2D slice perpendicular to the uni-axis as the bulk-edge correspondence. The occurrences of the non-zero section Chern number was attributed to Weyl points lying in the $k_z = 0$(time reversal invariant) plane. Further we deformed the photonic crystal to reduce the symmetry and observed that the Weyl points move in more general locations. Then we confirmed that the change of section Chern number exactly specifies the locations of Weyl points in the Brillouin zone. Further, we studied the chiral woodpile photonic crystal, which is also uniaxially chiral and possesses the similar structural symmetry to the array of helices. We confirmed Weyl points in the dielectric chiral woodpile photonic crystals and also that the topological edge modes lie under the light cone, which means those modes are confined at interface without certain claddings. The chiral woodpile photonic crystals are already fabricated in tens of micrometers, which corresponds to the near-infrared region in wavelength. Structures in this scale are suitable for integration to the currently existing electrical/optical systems. In addition, the topological edge modes in the chiral woodpile photonic crystal are circularly polarized, from which we can extract circularly polarized light from arbitrary incidence. Since in the very same sample, circular dichroism has already been observed, the studied topological edge modes also will be experimentally observed in near future.

Moreover in Chapter7, we considered the structural deformation of the woodpile structures and introduced the parameter for structural deformation as a fictitious momentum. We discussed the bulk-edge correspondence, in the synthetic Brillouin zone consisting of momentum and introduced parameter. As a consequence, the variation of edge modes during the structural deformation was characterized by the Chern number obtained by using the deformation parameter. With this, we showed the other way of utilizing topological properties than scattering free propagation.

Also in Chapter6, from the similarity between spatially and temporally periodic modulations, we considered to induce a time-varying effect in a photonic crystal. We were able to find a topologically non-trivial Floquet photonic band structure by the numerical evaluation of the Chern number and to find chiral edge modes induced in the time-varying photonic crystal.

In these studies, we always made a certain parameter, such as a wavenumber or a period of time modulation, confined and found topologically nontrivial states between Weyl points. We have made best use of the numerically obtained topological invariants to specify the topologically non-trivial regions and demonstrated the topological edge modes dispersions. The numerical method could also be newly applied to other continuous systems such as elastic systems. We hope that the method would be used to quantitatively optimize topological states as we have demonstrated in this thesis.

Publications

Jounal publications

- Shuhei Oono, Toshikaze Kariyado, and Yasuhiro Hatsugai, *Section Chern number for a three-dimensional photonic crystal and the bulk-edge correspondence*, Phys. Rev. B **94**, 125125 (2016)
- Shun Takahashi, Shuhei Oono, Satoshi Iwamoto, Yasuhiro Hatsugai, and Yasuhiko Arakawa, *Circularly polarized topological edge states derived from optical Weyl points in two kinds of semiconductor-based chiral woodpile photonic crystals*, In preparation, 2018
- Shuhei Oono, Shun Takahashi, Satoshi Iwamoto, Yasuhiro Hatsugai, and Yasuhiko Arakawa, *Structual deformation of the woodpile structure and the bulk-edge correspondence in the synthetic Brillouin zone*, In preparation, 2018

International conference contributions

- Shun Takahashi, Shuhei Oono, Satoshi Iwamoto, Yasuhiro Hatsugai, and Yasuhiko Arakawa "Topological Edge States by Resolving Weyl Points in Semiconductor Chiral Woodpile Photonic Crystals",ICO-24, Tokyo, Japan (2017)
- Shuhei Oono, Shun Takahashi, Satoshi Iwamoto, Yasuhiro Hatsugai, and Yasuhiko Arakawa "Topological edge modes of light in all dielectric chiral woodpile structures stacked with $\pi/4$ in-plane rotation", PLMCN 18, Würzburg, Germany (2017)
- Shun Takahashi,Shuhei Oono, Satoshi Iwamoto, Yasuhiro Hatsugai, and Yasuhiko Arakawa " Optical Weyl Points below the Light Line in Semiconductor Chiral Woodpile Photonic Crystals", CLEO 2017, San Jose, USA, (2017)
- Shuhei Oono, and Yasuhiro Hatsugai, "Topological edge modes in broken inversion 3D photonic crystals", EMN Summer Meeting 2017, Havana, Cuba (2017)
- Shuhei Oono, Toshikaze Kariyado, and Yasuhiro Hatsugai "Topological edge modes in time varying photonic systems", Bulk-edge correspondence 2016, Kyoto, Japan (2016)
- Shuhei Oono, Toshikaze Kariyado, and Yasuhiro Hatsugai "Topologically protected propagating modes of electromagnetic waves in 3D photonic crystals without inversion symmetry", PLMCN17, Nara, Japan (2016)
- Shuhei Oono, Toshikaze Kariyado, and Yasuhiro Hatsugai "Section Chern number and edge states in a 3D photonic crystal", Bulk-edge correspondence 2015, Tokyo, Japan (2015)
- Shuhei Oono, Toshikaze Kariyado, and Yasuhiro Hatsugai "Photonic Chern number and the bulk-edge correspondence by using a Gaussian basis", EP2DS-21, Sendai, Japan (2015)

Bibliography

[1] K. v. Klitzing, G. Dorda, and M. Pepper. New method for high-accuracy determination of the fine-structure constant based on quantized hall resistance. *Phys. Rev. Lett.*, 45:494–497, Aug 1980.

[2] D. J. Thouless, M. Kohmoto, M. P. Nightingale, and M. den Nijs. Quantized hall conductance in a two-dimensional periodic potential. *Phys. Rev. Lett.*, 49:405–408, Aug 1982.

[3] R. B. Laughlin. Quantized hall conductivity in two dimensions. *Phys. Rev. B*, 23:5632–5633, May 1981.

[4] B. I. Halperin. Quantized hall conductance, current-carrying edge states, and the existence of extended states in a two-dimensional disordered potential. *Phys. Rev. B*, 25:2185–2190, Feb 1982.

[5] Y. Hatsugai. Edge states in the integer quantum hall effect and the riemann surface of the bloch function. *Phys. Rev. B*, 48:11851–11862, Oct 1993.

[6] Y. Hatsugai. Chern number and edge states in the integer quantum hall effect. *Phys. Rev. Lett.*, 71:3697–3700, Nov 1993.

[7] F. D. M. Haldane. Model for a quantum hall effect without landau levels: Condensed-matter realization of the "parity anomaly". *Phys. Rev. Lett.*, 61:2015–2018, Oct 1988.

[8] C. L. Kane and E. J. Mele. Quantum spin hall effect in graphene. *Phys. Rev. Lett.*, 95:226801, Nov 2005.

[9] C. L. Kane and E. J. Mele. Z_2. *Phys. Rev. Lett.*, 95:146802, Sep 2005.

[10] E. Yablonovitch, T. J. Gmitter, and K. M. Leung. Photonic band structure: The face-centered-cubic case employing nonspherical atoms. *Phys. Rev. Lett.*, 67:2295–2298, Oct 1991.

[11] J. D. Joannopoulos, S. G. Johnson, J. N. Winn, and R. D. Meade. *Photonic Crystals: Molding the Flow of Light*. Princeton University Press, Princeton, 2008.

[12] K. Sakoda. *Optical Properties of Photonic Crystals*. Springer, Berlin, 2004.

[13] E. Yablonovitch. Inhibited spontaneous emission in solid-state physics and electronics. *Phys. Rev. Lett.*, 58:2059–2062, May 1987.

[14] S. John. Strong localization of photons in certain disordered dielectric superlattices. *Phys. Rev. Lett.*, 58:2486–2489, Jun 1987.

[15] A. Chutinan and S. Noda. Highly confined waveguides and waveguide bends in three-dimensional photonic crystal. *Applied Physics Letters*, 75(24):3739–3741, 1999.

[16] F. D. M. Haldane and S. Raghu. Possible realization of directional optical waveguides in photonic crystals with broken time-reversal symmetry. *Phys. Rev. Lett.*, 100:013904, Jan 2008.

[17] S. Raghu and F. D. M. Haldane. Analogs of quantum-hall-effect edge states in photonic crystals. *Phys. Rev. A*, 78:033834, Sep 2008.

[18] Z. Wang, Y. D. Chong, J. D. Joannopoulos, and M. Soljačić. Reflection-free one-way edge modes in a gyromagnetic photonic crystal. *Phys. Rev. Lett.*, 100:013905, Jan 2008.

[19] Z. Wang, Y. Chong, J. D. Joannopoulos, and M. Soljacic. Observation of unidirectional backscattering-immune topological electromagnetic states. *Nature*, 461(7265):772–775, 10 2009.

[20] S. H. Mousavi, A. B. Khanikaev, and Z. Wang. Topologically protected elastic waves in phononic metamaterials. *Nature Communications*, 6:8682 EP –, 11 2015.

[21] Y. Guo, T. Dekorsy, and M. Hettich. Topological guiding of elastic waves in phononic metamaterials based on 2d pentamode structures. *Scientific Reports*, 7(1):18043, 2017.

[22] Z. Yang, F. Gao, X. Shi, X. Lin, Z. Gao, Y. Chong, and B. Zhang. Topological acoustics. *Phys. Rev. Lett.*, 114:114301, Mar 2015.

[23] A. B. Khanikaev, R. Fleury, S. H. Mousavi, and A. Alù. Topologically robust sound propagation in an angular-momentum-biased graphene-like resonator lattice. *Nature Communications*, 6:8260 EP –, 10 2015.

[24] M. Xiao, W.-J. Chen, W.-Y. He, and C. T. Chan. Synthetic gauge flux and weyl points in acoustic systems. *Nature Physics*, 11:920 EP –, 09 2015.

[25] P. Wang, L. Lu, and K. Bertoldi. Topological phononic crystals with one-way elastic edge waves. *Phys. Rev. Lett.*, 115:104302, Sep 2015.

[26] P. Delplace, J. B. Marston, and A. Venaille. Topological origin of equatorial waves. *Science*, 358(6366):1075–1077, 2017.

[27] S. D. Huber. Topological mechanics. *Nature Physics*, 12:621 EP –, 06 2016.

[28] C. L. Kane and T. C. Lubensky. Topological boundary modes in isostatic lattices. *Nature Physics*, 10:39 EP –, 12 2013.

[29] L. M. Nash, D. Kleckner, A. Read, V. Vitelli, A. M. Turner, and W. T. M. Irvine. Topological mechanics of gyroscopic metamaterials. *Proceedings of the National Academy of Sciences*, 112(47):14495–14500, 2015.

[30] D. Z. Rocklin, B. G. Chen, M. Falk, V. Vitelli, and T. C. Lubensky. Mechanical weyl modes in topological maxwell lattices. *Phys. Rev. Lett.*, 116:135503, Apr 2016.

[31] T. Kariyado and Y. Hatsugai. Manipulation of dirac cones in mechanical graphene. *Scientific Reports*, 5:18107 EP –, 12 2015.

[32] Y. Takahashi, T. Kariyado, and Y. Hatsugai. Edge states of mechanical diamond and its topological origin. *New Journal of Physics*, 19(3):035003, 2017.

[33] L. Lu, J. D. Joannopoulos, and M. Soljačić. Topological photonics. *Nature Photonics*, 8:821 EP –, 10 2014.

[34] P. Yeh. *Optical Waves in Layered Media*. Wiley-Interscience, 2005.

[35] R. E. Prange and S. M. Girvin, editors. *The Quantum Hall Effect*. Springer, Lengeder Str. 52, 13407 Berlin, Germany, 1989.

[36] B. Doucot, V. Pasquier, and V. Rivasseau, editors. *The Quantum Hall Effect Poincare Seminar 2004*. Birkhauser, Basel, Swiss, 2005.

[37] M. V. Berry. Quantal phase factors accompanying adiabatic changes. *Proceedings of the Royal Society of London. Series A, Mathematical and Physical Sciences*, 392(1802):45–57, 1984.

[38] J. E. Avron, R. Seiler, and B. Simon. Homotopy and quantization in condensed matter physics. *Phys. Rev. Lett.*, 51:51–53, Jul 1983.

[39] B. Simon. Holonomy, the quantum adiabatic theorem, and berry's phase. *Phys. Rev. Lett.*, 51:2167–2170, Dec 1983.

[40] M. Kohmoto. Topological invariant and the quantization of the hall conductance. *Annals of Physics*, 160(2):343 – 354, 1985.

[41] J. D. Jackson. *Classical Electrodynamics Third Edition*. Wiley, 1998.

[42] Y. D. Chong, X.-G. Wen, and M. Soljačić. Effective theory of quadratic degeneracies. *Phys. Rev. B*, 77:235125, Jun 2008.

[43] T. Ochiai and M. Onoda. Photonic analog of graphene model and its extension: Dirac cone, symmetry, and edge states. *Phys. Rev. B*, 80:155103, Oct 2009.

[44] K. Ohtaka, T. Ueta, and K. Amemiya. Calculation of photonic bands using vector cylindrical waves and reflectivity of light for an array of dielectric rods. *Phys. Rev. B*, 57:2550–2568, Jan 1998.

[45] K. Ohtaka, J.-i. Inoue, and S. Yamaguti. Derivation of the density of states of leaky photonic bands. *Phys. Rev. B*, 70:035109, Jul 2004.

[46] S. A. Skirlo, L. Lu, and M. Soljačić. Multimode one-way waveguides of large chern numbers. *Phys. Rev. Lett.*, 113:113904, Sep 2014.

[47] S. A. Skirlo, L. Lu, Y. Igarashi, Q. Yan, J. Joannopoulos, and M. Soljačić. Experimental observation of large chern numbers in photonic crystals. *Phys. Rev. Lett.*, 115:253901, Dec 2015.

[48] A. B. Khanikaev, S. Hossein Mousavi, W.-K. Tse, M. Kargarian, A. H. MacDonald, and G. Shvets. Photonic topological insulators. *Nat Mater*, 12(3):233–239, 03 2013.

[49] M. A. Noginov and P. V. A., editors. *Tutorials in Metamaterials (Series in Nano-Optics and Nanophotonics)*. CRC Press, Boca Raton, Frolida, 2011.

[50] R. Marqués, F. Medina, and R. Rafii-El-Idrissi. Role of bianisotropy in negative permeability and left-handed metamaterials. *Phys. Rev. B*, 65:144440, Apr 2002.

[51] M. S. Rill, C. E. Kriegler, M. Thiel, G. von Freymann, S. Linden, and M. Wegener. Negative-index bianisotropic photonic metamaterial fabricated by direct laser writing and silver shadow evaporation. *Opt. Lett.*, 34(1):19–21, Jan 2009.

[52] R. A. Shelby, D. R. Smith, and S. Schultz. Experimental verification of a negative index of refraction. *Science*, 292(5514):77–79, 2001.

[53] S. A. Tretyakov, C. R. Simovski, and M. Hudlička. Bianisotropic route to the realization and matching of backward-wave metamaterial slabs. *Phys. Rev. B*, 75:153104, Apr 2007.

[54] J. K. Gansel, M. Thiel, M. S. Rill, M. Decker, K. Bade, V. Saile, G. von Freymann, S. Linden, and M. Wegener. Gold helix photonic metamaterial as broadband circular polarizer. *Science*, 325(5947):1513–1515, 2009.

[55] B. D. H. Tellegene. The gyrator, a new electric network element. *Philips Research Report*, 3(2):81–101, April 1948.

[56] T. Ochiai. Time-reversal-violating photonic topological insulators with helical edge states. *Journal of the Physical Society of Japan*, 84(5):054401, 2015.

[57] W. Eerenstein, N. D. Mathur, and J. F. Scott. Multiferroic and magnetoelectric materials. *Nature*, 442(7104):759–765, 08 2006.

[58] J. Ryu, A. V. Carazo, K. Uchino, and H.-E. Kim. Magnetoelectric properties in piezoelectric and magnetostrictive laminate composites. *Japanese Journal of Applied Physics*, 40(8R):4948, 2001.

[59] G. Srinivasan, E. T. Rasmussen, B. J. Levin, and R. Hayes. Magnetoelectric effects in bilayers and multilayers of magnetostrictive and piezoelectric perovskite oxides. *Phys. Rev. B*, 65:134402, Mar 2002.

[60] L.-H. Wu and X. Hu. Scheme for achieving a topological photonic crystal by using dielectric material. *Phys. Rev. Lett.*, 114:223901, Jun 2015.

[61] L. Fu. Topological crystalline insulators. *Phys. Rev. Lett.*, 106:106802, Mar 2011.

[62] D. Gloge. Weakly guiding fibers. *Appl. Opt.*, 10(10):2252–2258, Oct 1971.

[63] M. Hafezi, E. A. Demler, M. D. Lukin, and J. M. Taylor. Robust optical delay lines with topological protection. *Nat Phys*, 7(11):907–912, 11 2011.

[64] D. Angelakis. *Quantum Simulations with Photons and Polaritons: Merging Quantum Optics with Condensed Matter Physics*. Quantum Science and Technology. Springer International Publishing, 2017.

[65] G. Q. Liang and Y. D. Chong. Optical resonator analog of a two-dimensional topological insulator. *Phys. Rev. Lett.*, 110:203904, May 2013.

[66] T. Ochiai. Synthetic gauge field and pseudospin–orbit interaction in a stacked two-dimensional ring-network lattice. *Journal of Physics: Condensed Matter*, 29(4):045501, 2017.

[67] T. Ochiai. Floquet–weyl and floquet-topological-insulator phases in a stacked two-dimensional ring-network lattice. *Journal of Physics: Condensed Matter*, 28(42):425501, 2016.

[68] R. D. Meade, K. D. Brommer, A. M. Rappe, and J. D. Joannopoulos. Photonic bound states in periodic dielectric materials. *Phys. Rev. B*, 44:13772–13774, Dec 1991.

[69] S. G. Johnson and J. D. Joannopoulos. Block-iterative frequency-domain methods for maxwell's equations in a planewave basis. *Opt. Express*, 8(3):173–190, Jan 2001.

[70] J.-M. Jin. *The Finite Element Method in Electromagnetics*. Wiley-IEEE Press, Hoboken, 2014.

[71] A. Taflove and S. Hagness. *Computational Electrodynamics: The Finite-difference Time-domain Method*. Artech House antennas and propagation library. Artech House, 2005.

[72] D. C. Dobson. An efficient method for band structure calculations in 2d photonic crystals. *J. Comp. Phys.*, 149(2):363 – 376, 1999.

[73] W. Axmann and P. Kuchment. An efficient finite element method for computing spectra of photonic and acoustic band-gap materials: I. scalar case. *J. Comp. Phys.*, 150(2):468 – 481, 1999.

[74] D. C. Dobson, J. Gopalakrishnan, and J. E. Pasciak. An efficient method for band structure calculations in 3d photonic crystals. *J. Comp. Phys.*, 161(2):668 – 679, 2000.

[75] S. Oono, T. Kariyado, and Y. Hatsugai. Section chern number for a three-dimensional photonic crystal and the bulk-edge correspondence. *Phys. Rev. B*, 94:125125, Sep 2016.

[76] T. Fukui, Y. Hatsugai, and H. Suzuki. Chern numbers in discretized brillouin zone: Efficient method of computing (spin) hall conductances. *Journal of the Physical Society of Japan*, 74(6):1674–1677, 2005.

[77] G. H. Golub and C. F. V. Loan. *Matrix Computations (Johns Hopkins Studies in the Mathematical Sciences)*. Johns Hopkins University Press, 2012.

[78] H. S. Sözüer and J. W. Haus. Photonic bands: simple-cubic lattice. *J. Opt. Soc. Am. B*, 10(2):296–302, Feb 1993.

[79] L. Lu, L. Fu, J. D. Joannopoulos, and M. Soljačić. Weyl points and line nodes in gyroid photonic crystals. *Nature Photonics*, 7:294 EP –, 03 2013.

[80] L. Lu, Z. Wang, D. Ye, L. Ran, L. Fu, J. D. Joannopoulos, and M. Soljačić. Experimental observation of weyl points. *Science*, 349(6248):622–624, 2015.

[81] H. Nielsen and M. Ninomiya. A no-go theorem for regularizing chiral fermions. *Physics Letters B*, 105(2):219 – 223, 1981.

[82] M. Plihal and A. A. Maradudin. Photonic band structure of two-dimensional systems: The triangular lattice. *Phys. Rev. B*, 44:8565–8571, Oct 1991.

[83] M. C. Rechtsman, J. M. Zeuner, Y. Plotnik, Y. Lumer, D. Podolsky, F. Dreisow, S. Nolte, M. Segev, and A. Szameit. Photonic floquet topological insulators. *Nature*, 496(7444):196–200, 04 2013.

[84] J. C. W. Lee and C. Chan. Polarization gaps in spiral photonic crystals. *Opt. Express*, 13(20):8083–8088, Oct 2005.

[85] P. C. P. Hrudey, B. Szeto, and M. J. Brett. Strong circular bragg phenomena in self-ordered porous helical nanorod arrays of alq3. *Applied Physics Letters*, 88(25):251106, 2006.

[86] M. Thiel, M. Decker, M. Deubel, M. Wegener, S. Linden, and G. von Freymann. Polarization stop bands in chiral polymeric three-dimensional photonic crystals. *Advanced Materials*, 19(2):207–210, 2007.

[87] M. Thiel, G. von Freymann, and M. Wegener. Layer-by-layer three-dimensional chiral photonic crystals. *Opt. Lett.*, 32(17):2547–2549, Sep 2007.

[88] S. Takahashi, T. Tajiri, Y. Ota, J. Tatebayashi, S. Iwamoto, and Y. Arakawa. Circular dichroism in a three-dimensional semiconductor chiral photonic crystal. *Applied Physics Letters*, 105(5):051107, 2014.

[89] S. Takahashi, A. Tandaechanurat, R. Igusa, Y. Ota, J. Tatebayashi, S. Iwamoto, and Y. Arakawa. Giant optical rotation in a three-dimensional semiconductor chiral photonic crystal. *Opt. Express*, 21(24):29905–29913, Dec 2013.

[90] K. Aoki, H. T. Miyazaki, H. Hirayama, K. Inoshita, T. Baba, K. Sakoda, N. Shinya, and Y. Aoyagi. Microassembly of semiconductor three-dimensional photonic crystals. *Nature Materials*, 2:117 EP –, 01 2003.

[91] M.-L. Chang, M. Xiao, W.-J. Chen, and C. T. Chan. Multiple weyl points and the sign change of their topological charges in woodpile photonic crystals. *Phys. Rev. B*, 95:125136, Mar 2017.

[92] gnuplot. http://gnuplot.sourceforge.net/docs_4.2/node82.html.

[93] T. Oka and H. Aoki. Photovoltaic hall effect in graphene. *Phys. Rev. B*, 79:081406, Feb 2009.

[94] H. Sambe. Steady states and quasienergies of a quantum-mechanical system in an oscillating field. *Phys. Rev. A*, 7:2203–2213, Jun 1973.

[95] J. H. Shirley. Solution of the schrödinger equation with a hamiltonian periodic in time. *Phys. Rev.*, 138:B979–B987, May 1965.

[96] T. Kitagawa, T. Oka, A. Brataas, L. Fu, and E. Demler. Transport properties of nonequilibrium systems under the application of light: Photoinduced quantum hall insulators without landau levels. *Phys. Rev. B*, 84:235108, Dec 2011.

[97] T. Kitagawa, E. Berg, M. Rudner, and E. Demler. Topological characterization of periodically driven quantum systems. *Phys. Rev. B*, 82:235114, Dec 2010.

[98] J. Inoue. Space-time cooperative symmetry in a periodically driven tight binding model. *Journal of the Physical Society of Japan*, 86(2):024713, 2017.

[99] M. Holthaus. Floquet engineering with quasienergy bands of periodically driven optical lattices. *Journal of Physics B: Atomic, Molecular and Optical Physics*, 49(1):013001, 2016.

[100] D.-W. Wang, H.-T. Zhou, M.-J. Guo, J.-X. Zhang, J. Evers, and S.-Y. Zhu. Optical diode made from a moving photonic crystal. *Phys. Rev. Lett.*, 110:093901, Feb 2013.

[101] S. M. Young and C. L. Kane. Dirac semimetals in two dimensions. *Phys. Rev. Lett.*, 115:126803, Sep 2015.